FACULTY
OF MATHEMATICS
AND PHYSICS
Charles University

DOCTORAL THESIS

Martin Imríšek

Study of instabilities in tokamak plasmas using radiation diagnostics

Department of Surface and Plasma Science

Supervisor:	Prof. RNDr. Milan Tichý, DrSc.
Study programme:	Physics of Plasmas and Ionized Media
Consultants:	Mgr. Vladimír Weinzettl, PhD. RNDr. Jan Mlynář, PhD.

Prague 2022

I declare that I carried out this dissertation independently, and only with the cited sources, literature and other professional sources.

I understand that my work relates to the rights and obligations under the Act No. 121/2000 Sb., the Copyright Act, as amended, in particular the fact that the Charles University in Prague has the right to conclude a license agreement on the use of this work as a school work pursuant to Section 60 subsection 1 of the Copyright Act.

In .... date .... signature of the author

Here, I would like to thank my supervisor Milan Tichý for all his support during my study and many helpful corrections of the thesis. I am profoundly grateful to Vladimir Weinzettl and Jan Mlynar for their extensive support, feedback and help. My sincere thanks also belong to the whole COMPASS team, in particular to Matej Tomeš, Martin Hron, Fabien Jaulmes, Klara Bogár, Lukáš Kripner and Jakub Seidl for their helpful support. Furthermore, I would like to thank the Department of Surface and Plasma Science at the Charles University, namely to Jana Šafránková and Jiří Pavlů for their patience and nice seminars. For the lifelong encouragement and support, I would like to also thank my parents, sister, grandma and her cooking skills.

Title: Study of instabilities in tokamak plasmas using radiation diagnostics

Author: Martin Imríšek

Department: Department of Surface and Plasma Science

Supervisor: Prof. RNDr. Milan Tichý, DrSc.

Consultants: Mgr. Vladimír Weinzettl, PhD.
RNDr. Jan Mlynář, PhD.

Abstract: The thesis focuses on the characterisation of sawtooth instability and its effect on selected edge plasma processes at COMPASS. It is shown that sawtooth crash precedes the vast majority of L-H transitions, lower occurrence of ELMs and transitions to ELM-free H-mode. The sawtooth instability also affects H-L transitions, as their increased occurrence is observed in the middle of the sawtooth cycle. In the thesis, optimised tomography of the electromagnetic emission at COMPASS and JET is also applied to study instabilities in tokamak plasmas. The performance of fast tomographic methods with potential for real-time plasma control purposes is also studied. As the magnetic field configuration plays a vital role in plasma stability and tomographic reconstructions, the thesis also includes simulations of magnetic fields. These simulations were applied to optimise the design of coils for COMPASS-U.

Keywords: tokamak, tomography, sawtooth instability, electromagnetic emission

Název: Study of instabilities in tokamak plasmas using radiation diagnostics

Autor: Martin Imríšek

Katedra: Katedra fyziky povrchů a plazmatu

Vedoucí: Prof. RNDr. Milan Tichý, DrSc.

Konzultanti: Mgr. Vladimír Weinzettl, PhD.
RNDr. Jan Mlynář, PhD.

Abstract: Práce se zaměřuje na charakteriyaci pilovou nestabilitz a jejího vlivu na vybrané plasmové procesy na tokamaku COMPASS. Pád pilové nestability na tokamaku COMPASS předchází dominantní většíně L-H přechodů, sníženému výskutu nestability ELM a přechodům do H-modu v režimu bez nestabilitz ELM. Pilová nestabilita má také vliv na H-L přechod, který nastváv se yvýšenou pravděpodobností zhruba uprostřed jejího cyklu. Práce se také věnuje tomografické rekonstrukci elektromagnetického zaření na tokamaku COMPASS a JET včetně aplikace optimalizovaných algoritmů ke studiu nestabilit v tokamakovém plasmatu a testování rychlých tomografických metod s možným využitím k řízení plasmatu. Práce také obsahuje simulace magnetických polí, které hrají důležitou roli ve stabilitě plasmatu a ve výpočtu tomografických rekonstrukcí. Tyto simulace byly také využity pro optimalizaci designu cívek tokamaku COMPASS-U.

Klíčová slova: tokamak, tomografie, pilová nestabilita, electromagnetické záření

Contents

1. Introduction

Humankind faces growing needs for electrical power and dwindling natural resources. One of the possible solutions is a thermonuclear fusion, i.e. combination of atomic nuclei under high temperatures so that binding energy of nucleons can release in the form of the kinetic energy of products. This process naturally occurs in stars as a source of their energy and it also has the potential to become a nearly inexhaustible, safe and environmentally friendly source of energy for humankind. Thermonuclear fusion requires high temperatures (tens of million degrees) to overcome repulsive electrostatic force between nuclei so that short-range strong nuclear force can take place and nuclei can fuse. At such temperatures, the matter is in the form of ionised gas (plasma) which can be held by the magnetic field. Currently, the most developed concept for the thermonuclear power plant is a tokamak confining plasma in the toroidal vessel by the magnetic field generated by external coils and toroidal current induced in plasma. High temperatures are reached by ohmic heating of plasma current, injection of fast particles and by microwaves.

Tokamaks are supposed to be operated close to their limits to provide the best possible energy gain. Besides material limitations, there is a variety of plasma instabilities causing degradation of plasma confinement or abrupt termination of the plasma or even damage to the tokamak vessel. Such instabilities are typically a consequence of high gradients of plasma parameters (e.g. electron temperature can change from several keV in the plasma core to several eV at the plasma edge). The study of instabilities in tokamak plasmas is therefore essential for the ability to control plasma in order to achieve sustainable scenarios producing sufficient fusion power to establish fusion as a new energy source.

1.1 Goals and thesis overview

The general motivation of the thesis is to study plasma instabilities by means of electromagnetic emission, especially instabilities affecting total radiation losses and SXR emission from plasma core as they have a significant impact on plasma performance which is important for future fusion power plants. Moreover, the thesis also focuses on optimisation and tests of tools for analysis of electromagnetic emission, mainly on methods of tomographic reconstruction applied at COMPASS and JET.

The following chapters 2 and 3 are dedicated to magnetohydrodynamic equilibrium and instabilities and electromagnetic radiation in tokamak plasmas serving as a theoretical introduction for the rest of the thesis.

The chapter 4 presents simulations of plasma equilibrium at COMPASS and COMPASS-U performed by the FIESTA code. The shape of plasma equilibrium is important for tomographic reconstructions applied in the next chapter. Optimal equilibrium is found by the FIESTA code using similar techniques (inbuilt in the FIESTA) described in the following chapter about tomography. The chapter also includes simulations important for the design of COMPASS-U tokamak.

The chapter 5 deals with tomographic algorithm specialised for the reconstruction of tokamak plasmas properties as a tool for analysis of electromagnetic emission. One part of the chapter deals with reconstruction at COMPASS, including fast methods with the potential to be used for real-time plasma control, reconstruction of radiation losses distribution during ELMs and detachment studies and calculation of inversion radius of sawtooth instability, which is studied in the next chapter. The following part presents several applications of tomography at JET related to MHD instabilities and disruptions.

The last chapter 6 overviews the main experimental results. It begins with the characterisation of sawtooth instability at COMPASS and its scalings since sawtooth instability is observed to have a significant influence on other plasma instabilities and processes at COMPASS. Effects of sawtooth on other phenomena of plasmas at COMPASS such as L-H transition, H-L transition, transition to ELMy H-mode and occurrence of ELMs are studied in the remaining part of the chapter.

Attachments contains two articles in impacted journals. The first article A.2 expands topics in chapter 5 as it deals with optimisation of tomography. The second article A.3 is partly related to chapter 5 and partly to chapter 6.

2. Plasma stability in tokamaks and magnetohydrodynamic description

This chapter collects brief theoretical introduction into ideal MHD equilibria and plasma stability in tokamaks followed by classification of plasma instabilities and their measurable quantities.

2.1 Introduction

There are numerous published texts about plasma stability such as [1, 2, 3, 4]. Following theoretical introduction is focused on instabilities with well observable impact on electromagnetic emission.

There are several models describing plasma mainly differing in a character of applied simplifications according to the nature of studied phenomena. Basically, they are all based on the Boltzmann equation (in combination with the Maxwell's equations) [5]:

$$\frac{\partial f_\alpha}{\partial t} + (\mathbf{v}_\alpha \cdot \nabla_\mathbf{x})\, f_\alpha + \frac{1}{m_\alpha}\,(\mathbf{F}_\alpha \cdot \nabla_\mathbf{v})\, f_\alpha = \Big(\frac{\partial f_\alpha}{\partial t}\Big)_{coll} \tag{2.1}$$

where $f_\alpha(\mathbf{x}, \mathbf{v}, t)$ is a distribution function of particles of species α (meaning that $f_\alpha(\mathbf{x}, \mathbf{v}, t)\mathrm{d}x^3\mathrm{d}v^3$ gives a probability to find a particle at $\mathbf{x}$ with a velocity $\mathbf{v}$) and the term on the right side corresponds to the contribution due to the collisions. Further simplifications of the Boltzmann equation are necessary for practical use as the equation is too difficult to solve. According to the character of applied simplifications, models can be classified as either kinetic or fluid models.

Kinetic models can use Boltzmann equation with different versions of simplified collisional contribution such as Fokker-Planck equation (where the collision term is given by Coulomb collisions with particles in the Debye sphere with scattering angle less then $\pi/2$), Vlasov equation (collisions are neglected), etc. Gyro-kinetic models assume averaging over gyro-orbits around magnetic field lines (assuming that time and space scales of interest are larger than cyclotron frequency and Larmor radius) which makes the equations simpler to solve.

Fluid models derive their equations from moments of the Boltzmann (Focker-Planck) equation, i.e. from multiplying the equation 2.1 by appropriate scalar or function of $\mathbf{v}$ such as charge, mass, unity (conservation of particles), momentum and energy of particles and field. Resulting equations describe plasma as two fluids of electrons and ions under assumptions that:

- length-scales $\gg$ Larmor radius, mean free path
- time-scales $\gg$ cyclotron and collision times
- plasma is locally close to thermal equilibrium (i.e. Maxwellian distribution)

Two-fluid model can be simplified under assumptions that $T_i = T_e$ and $n_i = n_e$ to single-fluid model for non-ideal magnetohydrodynamic (MHD) plasma. Neglecting dissipation terms (i.e. resistivity, viscosity) leads to further simplification called ideal MHD for single-fluid model described by the following basic set of equations:

$$\frac{\partial n}{\partial t} + \nabla \cdot (n\mathbf{v}) = 0 \tag{2.2}$$

$$n\left[\frac{\partial \mathbf{v}}{\partial t} + \mathbf{v} \cdot \nabla \mathbf{v}\right] = \mathbf{J} \times \mathbf{B} - \nabla p \tag{2.3}$$

$$\frac{\partial p}{\partial t} + \mathbf{v} \cdot \nabla p = -\gamma p \nabla \cdot \mathbf{v} \tag{2.4}$$

$$\mu_0 \mathbf{J} = \nabla \times \mathbf{B} \tag{2.5}$$

$$\frac{\partial \mathbf{B}}{\partial t} = \nabla \times (\mathbf{v} \times \mathbf{B}) \tag{2.6}$$

Despite the numerous assumptions, the ideal MHD is worthy to use in tokamak physics as its equations include essential physics of plasma equilibria and instabilities in a relatively simple set of equations. Ideal MHD often gives useful answers for plasma stability as instabilities following ideal MHD tend to be the fastest and most violent. If a plasma is unstable according to the ideal MHD, it will not be controllable. Moreover, many non-ideal instabilities can be treated as variations of ideal instabilities.

2.2 MHD equilibrium

In a tokamak (see Fig. 2.1), magnetic field confining hot plasma can be divided into toroidal and poloidal components. Toroidal field B_ϕ (in the direction of ϕ coordinate) is created predominantly by external coils and stabilises confined plasma, whereas poloidal field B_p (combination of R and z components) is created both by the toroidal current in plasma I_p and current in external coils. Plasma current is driven mainly by the central solenoid, which acts as a primary winding while the plasma forms secondary winding. The current dragged through the plasma ohmically heats the plasma and creates a poloidal magnetic field helping to confine the plasma. On the other hand, external coils contribute to the total poloidal field by vertical component (otherwise higher magnetic field on the inner side of plasma column would cause plasma expansion), shaping component (to reach the required shape of plasma) and magnetising component varying so that it drives plasma current. In contrast, the topology of the magnetic field remains the same.

Typically, plasma discharge starts with circular cross-section touching a wall and it is later shaped into D-shaped divertor configuration (shown in Fig. 2.2) allowing separation of the confined plasma from the wall and consequently better energy confinement.

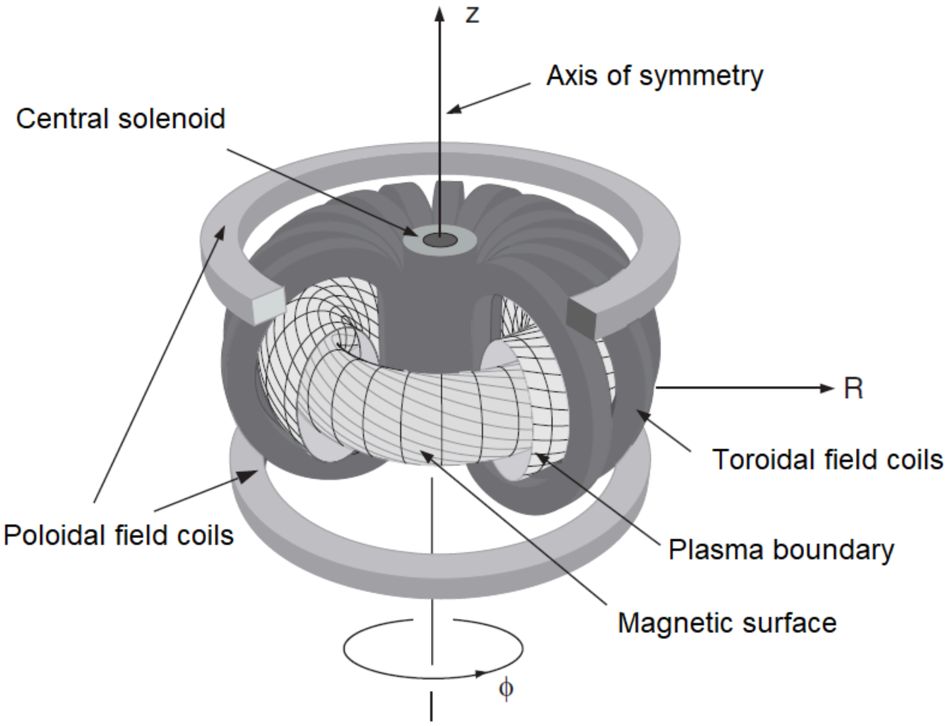

Figure 2.1: Schematic layout of a tokamak coil system in coordinates used to derive the equilibrium [2].

MHD equilibrium is reached when the force in the momentum equation 2.3 is balanced to zero:

$$\nabla p = \mathbf{j} \times \mathbf{B} \tag{2.7}$$

which also implies that there is no pressure gradient along magnetic field lines and current lies on magnetic flux surfaces:

$$\mathbf{B} \cdot \nabla p = \mathbf{j} \cdot \nabla p = 0 \tag{2.8}$$

Toroidal symmetry of a tokamak configuration allows to treat toroidal (azimuthal) angle as an ignorable coordinate and introduce flux of poloidal magnetic field (in the following formulas normalised by a factor 2π) which is constant on magnetic surfaces (also shown in Fig. 2.1).

$$\Psi(R, z) = \int_0^R B_z\left(R', z\right) R' \mathrm{d}R' \tag{2.9}$$

Vertical magnetic field can be then expressed as:

$$B_z(R, z) = \frac{1}{R}\frac{\partial \Psi(R, z)}{\partial R}, \tag{2.10}$$

radial magnetic field can be obtained from $\nabla \cdot \mathbf{B} = 0$ as:

$$B_R(R, z) = -\frac{1}{R}\frac{\partial \Psi(R, z)}{\partial z}. \tag{2.11}$$

Using the Amper's law and neglecting poloidal component of plasma current leads to:

$$B_\phi = \frac{\mu_0 I}{2\pi R} \tag{2.12}$$

where I is a current flowing in poloidal direction around a magnetic surface, e.g. in toroidal field coils.

Inserting equations 2.10, 2.11 together with $\nabla \times \mathbf{B} = \mu_0 \mathbf{j}$ into 2.7 and introducing partial derivative of pressure and current as $\partial f(\psi)/\partial r = \mathrm{d}f/\mathrm{d}\psi \cdot \partial\psi/\partial r$, where f is defined as $f = B_\phi R$, leads to the equation known as Grad-Shafranov equation [6]:

$$\Delta^* \psi = -\frac{\mu_0^2}{8\pi^2} I \frac{dI}{d\psi} - \mu_0 R^2 \frac{dp}{d\psi} = -\mu_0 R j_\phi, \tag{2.13}$$

where Δ^* is a Laplacian-like operator in cylindrical geometry (with reversed order of the factors R and $1/R$ and without $\partial^2/\partial\phi^2$ due to the toroidal symmetry):

$$\Delta^* = R\frac{\partial}{\partial R}\left(\frac{1}{R}\frac{\partial}{\partial R}\right) + \frac{\partial^2}{\partial z^2}. \tag{2.14}$$

The equation is often used in tokamaks to find magnetic field required for equilibrium from assumed or measured p and I, i.e. from profiles of pressure and poloidal current (or from toroidal magnetic field). Finding such equilibrium magnetic field can also provide required currents in external coils which is crucial for a tokamak design (as it also determines heat loads and forces acting on the coils). Since the ψ is present on both sides of the Grad-Shafranov equation, the solution is often found in iterative steps where ψ and j_ϕ are updated each step while satisfying expected shapes of $I(\psi)$, $p(\psi)$ and boundary conditions.

Detailed derivation of the Grad-Shafranov equation including extension for toroidal rotation Ω (which can appear as a result of external torque, e.g. during NBI heating or spontaneously) where p enters the Grad-Shafranov equation as a function $p(\psi, R)$ satisfying $\left.\frac{\partial p}{\partial R}\right|_\psi = \rho R \Omega^2(\psi)$, numerical solutions, analytical Solovjev solution and other insights can be found in [4]. Usually, equilibrium in tokamaks is solved without extension for toroidal rotation as it results in minor correction for subsonic velocities [7] (i.e. in most of the experiments) and it can be non-trivial to measure. An example of reconstructed ψ is shown in Figure 2.2.

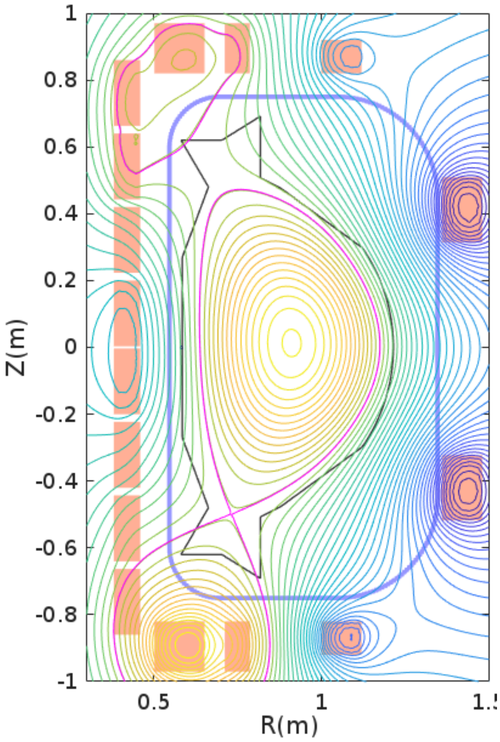

Figure 2.2: Vertical cross-section of designed COMPASS-U tokamak showing an example of own simulation of MHD equilibrium (magnetic field lines as colored contours) by the Fiesta code (described more into detail in chapter 4). Magenta line corresponds to the separatrix value defining geometry of confined plasma inside plasma-facing components (black). Orange boxes represent poloidal field coils and central solenoid (3D scheme is shown in the previous Fig. 2.1).

2.3 MHD stability

Once the MHD equilibrium is found, it is possible to predict its stability. One of the well known approaches allowing prediction of system stability is the energy principle. It is a variational technique determining stability of an equilibrium from a change of potential energy caused by any possible perturbation. In such perturbated state, a system is shifted from its equilibrium to a state where condition for balanced forces is not valid anymore ($\mathbf{F} = \mathbf{J} \times \mathbf{B} - \nabla p \neq 0$) and the potential energy of a system is changed. If the change of potential energy is negative ($\mathrm{d}W < 0$) plasma can change to a new configuration. If the change is positive ($\mathrm{d}W > 0$), plasma is stable. Essential elements of MHD stability can be derived from linearization of MHD equations where all quantities are expanded as $Q = Q_0 + Q_1$ where Q_0 is equilibrium value and Q_1 small perturbation. Linearized ideal MHD equations can be then derived as:

$$\frac{\partial \rho_1}{\partial t} + \rho_0 \nabla \cdot \mathbf{v}_1 = 0 \tag{2.15}$$

$$\rho_0 \frac{d\mathbf{v}_1}{dt} = -\nabla p_1 + \mathbf{J}_0 \times \mathbf{B}_1 + \mathbf{J}_1 \times \mathbf{B}_0 \tag{2.16}$$

$$\frac{\partial p_1}{\partial t} = -\mathbf{v}_1 \cdot \nabla p_0 - \gamma p_0 \nabla \cdot \mathbf{v}_1 \tag{2.17}$$

$$\frac{\partial \mathbf{B}_1}{\partial t} = \nabla \times (\mathbf{v}_1 \times \mathbf{B}_0) \tag{2.18}$$

$$\nabla \times \mathbf{B}_1 = \mu_0 \mathbf{J}_1 \tag{2.19}$$

$$\nabla \times \mathbf{B}_0 = \mu_0 \mathbf{J}_0. \tag{2.20}$$

Introducing the perturbed displacement vector $\boldsymbol{\xi}$ as $\partial\boldsymbol{\xi}/\partial t = v_1$ and inserting p_1, J_1 and J_0 from 2.17, 2.19 and 2.20 modifies momentum equation 2.16 into:

$$\rho \frac{\partial^2 \boldsymbol{\xi}}{\partial t^2} = \mathbf{f}(\boldsymbol{\xi}) \tag{2.21}$$

where

$$\mathbf{f}(\boldsymbol{\xi}) = \nabla\left(\boldsymbol{\xi} \cdot \nabla p_0 + \gamma p_0 \nabla \cdot \boldsymbol{\xi}\right) + \frac{1}{\mu_0}\left(\nabla \times \mathbf{B}_1\right) \times \mathbf{B}_0 + \frac{1}{\mu_0}\left(\nabla \times \mathbf{B}_0\right) \times \mathbf{B}_1 \tag{2.22}$$

is an operator representing force density. Application of the Fourier transformation to the perturbed quantities ($Q_1(\mathbf{r}, t) = Q_1(\mathbf{r}) \exp(-\mathrm{i}\omega t)$) leads to the linearization of the momentum equation:

$$-\omega^2 \rho \boldsymbol{\xi} = \mathbf{f}(\boldsymbol{\xi}) \tag{2.23}$$

Eigenvalues ω^2 of the $\mathbf{f}$ operator have several important properties useful for spectral analysis such as that ω can be purely real or purely imaginary (this is only true for ideal MHD), continuum eigenvalues are permitted only in the stable domain ($\omega^2 > 0$), etc. [8].

The change of the potential energy can be expressed as a negative of work performed by force 2.23 linearly growing with $\boldsymbol{\xi}$:

$$\delta W = -\frac{1}{2} \int \boldsymbol{\xi}^* \cdot \mathbf{f}(\boldsymbol{\xi}) \mathrm{d}V \tag{2.24}$$

where $\boldsymbol{\xi}^*$ is conjugate value of $\boldsymbol{\xi}$. The equation 2.24 can be expressed as [8]:

$$\begin{aligned}\delta W(\boldsymbol{\xi}) =& \frac{1}{2} \int_p \left(\gamma p_0 |\nabla \cdot \xi|^2 + (\xi \cdot \nabla p_0)(\nabla \cdot \xi^*) - \mathbf{J}_0 \cdot (\mathbf{B}_1 \times \xi^*) + \frac{B_1^2}{\mu_0} \right) \mathrm{d}V \\ &+ \frac{1}{2} \int_s \left(p_1 + \mathbf{B}_0 \cdot \frac{\mathbf{B}_1}{\mu_0} \right) \xi \cdot \mathrm{d}\mathbf{S} + \frac{1}{2} \int_v \frac{B_1^2}{\mu_0} \mathrm{d}V \end{aligned} \tag{2.25}$$

where integrals subscripted by p, s and v correspond to contributions from plasma volume, plasma-vacuum interface and vacuum envelope respectively. The third term for vacuum contribution is always positive and stabilising. The second term integrating over plasma-vacuum surface (obtained via the Gauss's theorem) is zero for perturbations in tangential directions which suggests natural division of MHD modes into free-boundary and fixed-boundary modes (without deformation of plasma-vacuum surface). The first term can be rewritten into so-called *intuitive form* as it allows to characterise different stabilising and destabilising contributions by their nature [2]:

$$\begin{aligned}
\delta W_p(\boldsymbol{\xi}) =& \frac{1}{2}\int_p \gamma p_0 |\nabla\cdot\boldsymbol{\xi}|^2 && \textit{fluid compression (sonic wave)}\\
&+ \frac{B_{1\perp}^2}{\mu_0} && \textit{field line bending (shear Alfvén wave)}\\
&+ \frac{B_0^2}{\mu_0}\left|\nabla\cdot\xi_\perp + 2\xi_\perp\cdot\kappa\right|^2 && \textit{field line compression (compr. Afvén wave)}\\
&- 2\left(\xi_\perp\cdot\nabla p_0\right)\left(\xi_\perp^*\cdot\kappa\right) && \textit{pressure driven mode}\\
&- \mathbf{J}_{||0}\cdot\left(\mathbf{B}_{1\perp}\times\xi_\perp^*\right)\mathrm{d}V && \textit{current driven (kink) mode}
\end{aligned} \tag{2.26}$$

where $\boldsymbol{\xi}$, $\mathbf{B_1}$ and $\mathbf{J_1}$ were separated into parallel and perpendicular components with respect to the equilibrium field $\mathbf{B_0}$, several $\xi_{||}$ were cancelled and $\boldsymbol{\kappa}$ is the curvature of $\mathbf{B_0}$:

$$\boldsymbol{\kappa} = \frac{\mathbf{B}}{B}\cdot\nabla\left(\frac{\mathbf{B}}{B}\right), \quad \text{with} \quad |\boldsymbol{\kappa}| = \frac{1}{R_c} \tag{2.27}$$

The first three terms in the equation 2.26 are always positive and stabilising, i.e. resulting in oscillations around equilibrium, whereas last two terms can be either positive (stabilising) or negative (destabilising). Thus, there are two sources of MHD instability: one proportional to the ∇p_0 and other to the $\mathbf{J}_{||0}$. The former is responsible for kink or sausage instability well known in plasma columns carrying current. The latter term provides negative contribution when ∇p_0 and κ have the same direction which typically happens in tokamaks on the outer region of plasma torus and it is responsible for Rayleigh-Taylor or so-called ballooning instabilities.

In the incompressible MHD model, the first term with $\nabla\cdot\boldsymbol{\xi}$ is zero due to the incompressibility

$$\nabla\cdot\boldsymbol{\xi} = 0 \tag{2.28}$$

which is a useful limit for the case when the growth time of the MHD instability of interest is much longer than adiabatic transit time across one wavelength [3]. The sound of speed is infinite in this limit. Conditions of instability can be further examined by introducing Fourier decomposition of perturbations $\boldsymbol{\xi}$ in appropriate spatial coordinates (i.e. in contrast to the previous application of Fourier decomposition of time domain in the motion equation 2.23, here reached perturbations $\boldsymbol{\xi}$ will be decomposed into space coordinates). Expression of δW_p for a tokamak with general poloidal cross section is described e.g. in [2] with decomposition according to $\boldsymbol{\xi} = \boldsymbol{\xi}(\psi,\chi)e^{in\phi}$ where ϕ is toroidal angle, χ poloidal coordinate, n integer number and ψ poloidal flux taking a role of radial coordinate. Resulting form of δW_p is too complex for practical use but it can provide physical insights in its two limiting cases. One limit is "straight" tokamak approximation [3] where toroidal curvature is neglected and it is useful for current driven modes where curvature can be neglected (in contrast to the pressure driven source of instabilities containing curvature $\boldsymbol{\kappa}$ as it is shown in 2.26). Second limit is local expansion around so-called resonant magnetic surfaces and it is useful for high n pressure driven modes. Both limiting cases are briefly introduced in next sections 2.4.1 and 2.4.2.

2.4 Basic classification of MHD instabilities

As it was indicated in the previous sections, there are several ways how to classify MHD instabilities: according to the type of distortion (if plasma resistivity is important), location of the instability (internal with fixed boundary or external with free boundary) or according to the source of instability (current driven or pressure driven). In this section, several MHD instabilities are briefly over-viewed with respect to the latter classification. Even though instabilities are usually combination of both pressure and current driven sources, it is still useful to classify them as current driven or pressure driven instabilities according to the dominant effect as physical description and behaviour is similar in both groups. However, in several cases both effects are comparably important and such instabilities can be referred as combined pressure and current driven modes [2]. Furthermore, there are instabilities driven by the kinetic distribution of plasma particles in velocity space (particle driven MHD modes). Following parts of this section contain known theoretical background important for understanding of MHD instabilities. However, theoretical description is still incomplete and one of the motivation of the thesis is to contribute to knowledge about plasma instabilites.

2.4.1 Current driven instabilities

The current driven modes, i.e. kink modes can be both external and internal. External modes limit maximal current and can cause termination of discharge whereas internal modes limit current density and steepness of current profile. As it was outlined in the previous chapter, their behaviour can be predicted from the 'straight' tokamak approximation where toroidal curvature is neglected and poloidal cross section is approximated as circular. This allows Fourier decomposition of displacement $\boldsymbol{\xi}$ into cylindrical coordinates r, θ, z with periodicity in poloidal direction $f(\theta) = f(\theta + m2\pi)$ and wave number $k_z = n/R_0$ resembling a toroidal system [2]:

$$\boldsymbol{\xi}(r, \theta, z) = \xi(r) e^{i\left(m\theta - \frac{n}{R_0} z\right)} \tag{2.29}$$

where R_0 is a major radius of the torus, m poloidal mode number and n toroidal mode number. Resulting δW can be seen as special case of energy principle 2.25 called general screw pinch and it is derived e.g. in [3]. The "straight" tokamak approximation is derived from the general screw pinch by assuming:

$$\begin{aligned} \epsilon &\ll 1 \\ B_\theta / B_z &\sim \varepsilon \\ q &\sim 1 \\ \beta = 2\mu_0 p / B_z^2 &\sim \varepsilon^2 \end{aligned} \tag{2.30}$$

where

$$\varepsilon = a/R_0 \tag{2.31}$$

is the inverse aspect ratio. Resulting δW can be expressed as Taylor expansion for low $\beta \sim \varepsilon^2$ in the form $\delta W = \delta W_0 + \delta W_2 + \delta W_4 + \cdots$, where each term scales as $\delta W_n \sim \varepsilon^n \delta W_0$ with $\delta W_0 \sim B_z^2 R_0 \xi^2 / \mu_0$ [3]. Despite many simplifications, the "straight" tokamak approximation describes surprisingly well basic behaviour of kink modes (especially external kink modes) and resulting practical limits of tokamak operation. The first non-zero contribution to δW is of second order and it was derived in [9]:

$$\begin{aligned}\frac{\delta W_2}{W_0} =& \int_0^a \left[(r\xi')^2 + \left(m^2-1\right)\xi^2\right]\left(\frac{n}{m}-\frac{1}{q}\right)^2 r\mathrm{d}r \\ &+ \xi_a^2 a^2 \left(\frac{2}{q_a}\left(\frac{n}{m}-\frac{1}{q_a}\right) + (1+m\lambda)\left(\frac{n}{m}-\frac{1}{q_a}\right)^2\right)\end{aligned} \tag{2.32}$$

where $W_0 = 2\pi^2 R_0 B_0^2/\mu_0 a^2$, $\lambda \equiv \frac{1+(a/b)^{2m}}{1-(a/b)^{2m}}$ (derivation of precise expression can be found in [3]) represents influence of the wall at radius $r = b$ to the plasma with boundary at $r = a$ and the q safety factor defined as:

$$q \equiv \frac{\mathrm{d}\Phi}{\mathrm{d}\psi} \simeq \frac{rB_z}{R_0 B_\theta} \tag{2.33}$$

where Φ is toroidal magnetic flux and the approximated expression assumes circular cross section and $R_0/a \gg 1$. While deriving the δW_2 relation from the 2.25, B_1 was replaced via relation 2.18, ξ' appears due to the $\nabla \cdot \boldsymbol{\xi}_\perp$, $\nabla \cdot \boldsymbol{\xi}$ disappears due to incompressibility condition 2.28, $\mathbf{J}_{||0}$ became represented by q as well as curvature κ (for the screw pinch, $\kappa = -\mathbf{e}_r \frac{B_\theta^2}{rB^2}$ [3]). More details about the derivation and proprieties of the 2.32 can also be found in [3]. The pressure disappeared as a consequence of the assumption that plasma pressure is small compared to pressure of toroidal magnetic field given by the last line in 2.30 (the ratio is several percent in tokamaks). Thus, the equation 2.32 is related only to the current driven mode (dependence on current is represented by q).

The first line of the expression 2.32 corresponds to the δW_p plasma term whereas the second line corresponds to the plasma-vacuum interface influencing stability of external modes (with $\xi_a \neq 0$).

The integral term can not be negative which implies that stability of external modes is determined by balance between destabilising plasma-vacuum interface term and stabilising plasma term. In the plasma-vacuum interface term, only the first term can contribute to instability when:

$$\left(\frac{n}{m}-\frac{1}{q_a}\right) < 0 \tag{2.34}$$

implying that the necessary condition for external kink instability (under given assumptions) is a presence of a resonant surface outside the plasma in vacuum region ($q_a < m/n$). It can be also shown [3, 2] that the lower m the higher the negative contribution of the plasma-vacuum term, see also Fig 2.3.

For the most unstable $m = 1$ mode, the stability condition $q_a > 1$ is known as Kruskal-Shafranov limit [3]. Inserting the definition of the safety factor 2.33 allows to rewrite it as a condition for maximal achievable current in plasma:

$$I_p < \frac{2\pi a^2}{\mu_0 R_0} B_z \tag{2.35}$$

In reality, plasma becomes often unstable already for $q_a < 3$ as higher modes appear and operation for $q_a < 2$ requires specific active feedback control to counteract the mode $m = 2$ growth [10].

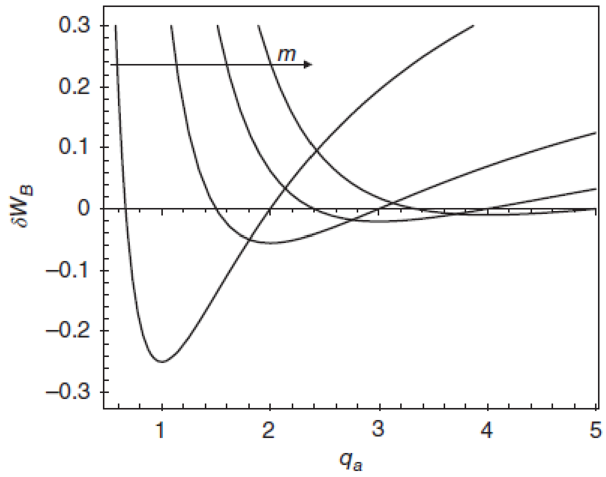

Figure 2.3: Contribution of the boundary (plasma-vacuum interface) term δW_b for $n = 1$ as a function of q_a for m = 2,3,4,5 [2].

Moreover, also internal kink modes are often observed that can not be derived from the equation 2.32 as only the boundary term was contributing to the plasma instability. In order to describe internal kink modes, the higher order of δW expansion has to be taken into account. The δW_4 contribution for $m = 1$ was derived in [11] using trial function closing to the step function with $\xi' = 0$ inside $q = 1$ and $\xi_{edge} = 0$ outside $q = 1$:

$$\frac{\delta W_{4,cyl}}{W_0} = \xi_0^2 n^2 \int_0^{r_1} \left(r\beta' + \frac{r^2}{R_0^2} \left(n - \frac{1}{q} \right) \left(3n + \frac{1}{q} \right) \right) r\mathrm{d}r \tag{2.36}$$

where β' is radial derivative of the *plasma beta* which is defined as ratio of kinetic and magnetic pressure:

$$\beta = \frac{2\mu_0 p}{B^2} \tag{2.37}$$

The δW_2 for the $m = 1$ internal kink mode (from 2.32):

$$\frac{\delta W_2}{W_0} = \int_0^a \left(\frac{n}{m} - \frac{1}{q} \right)^2 r^2 \xi'^2 r\mathrm{d}r \tag{2.38}$$

vanishes for the chosen $\xi(r)$ and the change of potential energy is given by the relation 2.36, i.e. $\delta W_p \simeq \delta W_{4,cyl}$. The first term in the integration is usually destabilising as $\beta' < 0$ for pressure decreasing from the core to the edge and the second term is destabilising if $q(r) < 1$ so the necessary stability condition (for monotonically increasing q-profiles) is:

$$q(0) > 1 \tag{2.39}$$

and can be rewritten as a condition for central current density as using $\nabla \times \mathbf{B} = \mu_0 \mathbf{j}$ (for $r \to 0$) with the approximated definition of the safety factor 2.33 gives:

$$j(0) < \frac{2B_z}{\mu_0 R_0} \tag{2.40}$$

From the physical point of view, the negativity of the second term in 2.36 (if $q(0) < 1$) describes a situation when destabilising contribution of kink instability overcomes stabilising effect due to the energy required to bend field lines (fluid compression vanished due to the incompresibility condition 2.28, field compression by choice of ξ during approximation of δW_4 and the pressure-driven source is represented by the first term). The presence of the pressure in the equation 2.36 derived by assuming displacement of the central column (represented by chosen $\xi(r)$) implies that the internal kink mode is not purely current-driven instability. However, a current carrying column remains a necessary condition. Toroidal geometry makes solution more complicated, but the basic result remains the same, i.e. necessary condition $q(0) < 1$ [12].

An important consequence of the internal $m = 1$, $n = 1$ kink mode is so-called sawtooth instability. The internal kink mode, sawtooth instability and its effect on other plasma processes are studied in the chapter 6.

2.4.2 Pressure driven instabilities

Pressure driven instabilities originates from the term $2\left(\boldsymbol{\xi}_\perp \cdot \nabla p_0\right)\left(\boldsymbol{\kappa} \cdot \boldsymbol{\xi}_\perp\right)$ in 2.26. It can be seen that a contribution of this term is destabilising (i.e. negative) when $\boldsymbol{\kappa}$ and ∇p_0 have the same sign and their vectors are parallel. In tokamaks, this term is typically negative on the outer side of the torus as both the pressure gradient and the curvature of magnetic field lines point towards the centre of the torus whereas it is positive on the inner side of the torus where the pressure gradient has an opposite direction. These regions are sometimes referred as regions with a bad and good curvature, respectively.

In tokamaks, the effect of the bad curvature on LFS is compensated along magnetic field lines (helically surrounding the plasma so that it travels between the HFS and LFS regions) by the effect of the good curvature on HFS so that larger modes with a perturbation of the plasma boundary aligned with the magnetic field lines (i.e. with the same phase along the magnetic field lines) are typically stable according to the Mercier criterion [13, 14, 2] for $q > 1$ and an internal kink mode dominates the stability of the plasma. However, the LFS region is susceptible to localised instabilities called ballooning modes which act as an elongation of a squeezed balloon and causes a sudden release of the energy. Pressure driven ballooning modes limit the edge pressure gradient and achievable β.

2.4.3 Pressure and current driven instabilities

The pressure or current driven instabilities described in the previous sections are related only to one specific term in the equation for the plasma potential energy 2.26. In practise, both the effects often combine to drive a plasma instability.

One of the instabilities combining both the effects is the edge localised mode (ELM) [15, 16, 17]. Basically, the ELM is a quasi-periodic relaxation of the steep pressure gradient developed during a high-confinement mode (H-mode) which results in high heat loads on tokamak vessel. H-mode is a regime with a better energy confinement due formation of the edge transport barrier, see Fig. 2.4a. Transition to the higher confinement mode [15] is observed to be connected with formation of the shear flow layer (associated with the radial electric field) at the plasma edge suppressing (”tearing”) turbulences and reducing transport [18]. It is observed to occur when the power crossing the separatrix exceeds a critical threshold depending on n_e, B_T, area enclosed by the separatrix, X-point height, ion species and others [8]. During the ELM cycle, the edge pressure gradient gradually increases due to the edge transport barrier. Increase the of edge pressure gradient can cause an increase of the edge current density due to a bootstrap current. The bootstrap current is a self-generated current in the presence of the pressure gradient due to collisions between passing and trapped particles (i.e. particles reflected on the HFS due to the high magnetic field) [19, 20, 21]. Both the edge pressure gradient and edge current density have their limits leading to an instability, see Fig. 2.4b.

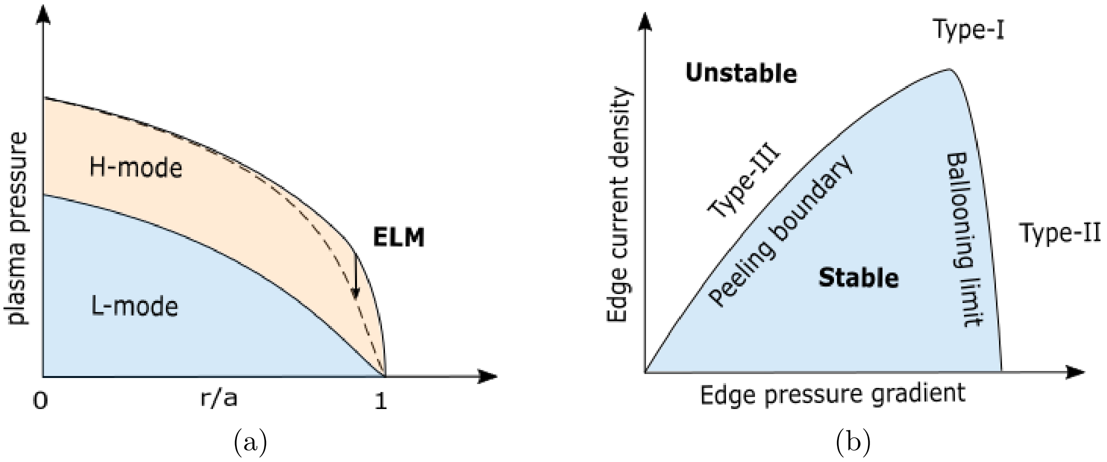

(a) (b)

Figure 2.4: (a) Schematic illustration of the pressure profiles during L-mode and H-mode and the effect of ELM and (b) the stability diagram for ELM.

The pressure gradient is limited by the ballooning mode described in the previous section and the edge current density is limited by the localised peeling mode [16]. The nature of the localised peeling mode is similar to the internal kink mode as its instability is driven by a high current density and results into peeling of current filaments from the confined plasma. The ELMs are sometimes divided into three groups [22, 16]:

Type-I : Large ELMs which are supposed to be caused by coupled peeling-ballooning modes. The model describes the ELM cycle as a development of the pressure gradient towards the balloning limit where it stops and the edge current density limit increases towards the coupled peeling-ballooning limit causing a sudden collapse of the edge pressure gradient resulting in an expulsion of a high amount of the energy to the divertor plates. This type of ELMs is typically observed in high confinement plases at a high plasma heating. The frequency of ELMs increases with plasma heating.

Type-II : Appears in a narrow operational window, i.e. during strongly shaped plasmas with a high elongation, triangularity and density. Their magnitude is smaller and the frequency is higher than in the case of the type-I ELMs. According to the model, type-II ELMs are governed mainly by the ballooning mode.

Type-III : The smallest and most frequent ELMs typically occurring at conditions close to the transition between the L-mode and the H-mode when the edge temperature is rather low (and resistivity high). Their frequency decreases with the plasma heating. An amount of the expelled energy is relatively low compared to the type-I ELMs but their high frequency typically leads to high energy losses causing a stronger degradation of the energy confinement.

In summary, as the plasma heating increases it can cross the threshold for the L-H transition and H-mode with the edge transport barrier and type-III ELM take place. Even higher plasma heating leads to a decrease of the ELM frequency up to the regime with no ELMs, i.e. ELM-free H-mode. Further increase of the plasma heating leads to a regime with large type-I ELMs. Advantage of ELMs is that they help to clean the confined plasma from impurities. The ELM-free regime can eventually leads to a disruption due to a strong cooling related to the significant radiation of accumulated impurities. The disadvantage of ELMs is high sudden heat loads which can damage the divertor plates, in particular in the case of type-I ELMs. Therefore, various techniques suppressing their destructive effect were developed including vertical kicks (provoking the instability before larger ELM occurs [23, 24, 25]), the detachment regime (described in section 3.3.1), pellet injection (increasing ELM frequency and decreasing their energy [26, 27, 28]) or resonant magnetic perturbations (which can change the ELM frequency and size or even completely suppress ELMs while preserving a good energy confinement [17, 29, 30, 31]).

In tokamak plasmas, there are various instabilities and processes driven by the pressure and current including e.g. external kink modes and ballooning-kink modes which consequently lead to the so-called Troyon beta limit [32]:

$$\beta_N = \beta \frac{a B_T}{I_p} \tag{2.41}$$

which has been calculated as 2.8%. In practise, the limit can vary as it depends on the shape of the poloidal cross-section and current profile and due to external conducting structures which can stabilise instabilities [33].

2.5 Operational limits and disruptions

A tokamak plasma is affected by various instabilities and processes beyond the MHD description including radiative instabilities (mentioned in section 3.3.1), vertical displacement events (regarded in section 4.3.3 and 4.3.5) and many others. One group of instabilities typically only limits a plasma performance (e.g. sawtooth instability or ELM) whereas the second group limits an operational space of stable operation as they violate plasma stability conditions so that it leads to a significant degradation of the plasma confinenemt or even to disruptions, i.e. an uncontrolled termination of discharge and loss of the plasma current. The main operational limits of tokamak can be illustrated by the Hugill diagram, see 2.5. The Hugill diagram does not cover all the limitations for the tokamak operation, but it provides a basic idea about achievable plasma parameters.

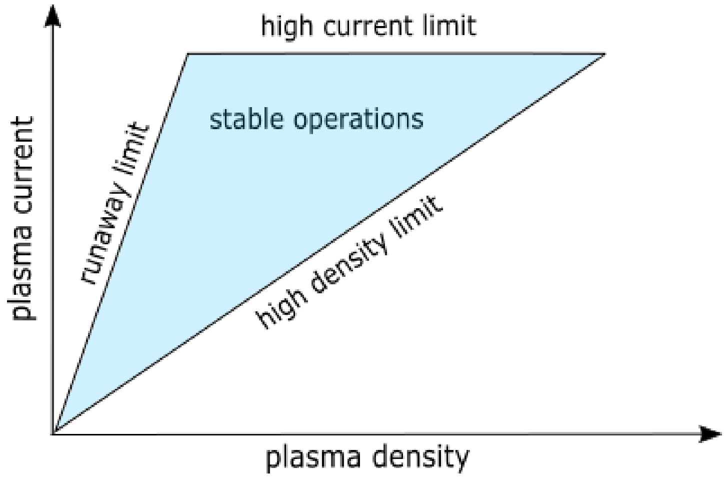

Figure 2.5: The Hugill diagram showing main limits of the tokamak operation. The favourable region of the tokamak operation is near the right corner with a high density, i.e. with a high fusion reation rate.

The high current limit in the Hugill diagram is mainly given by the external kink mode mentioned in section 2.4.1. The condition 2.35 (or $q_a < 3$) shows that the maximal plasma current increases with the toroidal (axial) magnetic field and minor radius. In reality, the maximal current is often evaluated numerically as it can be higher for non-circular, D-shaped plasmas and depends on current and pressure profiles [33].

The high density limit represents an important constrain since the rate of fusion reactions scales with the squared plasma density (see section 3.3). It was determined empirically as the so-called Greenwald limit [34, 35]:

$$n_G = \frac{I_p}{\pi a^2} \tag{2.42}$$

where n_g is the line averaged density in 10^{20} m^{-3}, I_p the plasma current in MA and a the minor radius in m. Exceeding the limit often triggers the multifaceted asymmetric radiation from the edge (MARFE) which is an instability creating poloidaly assymetric zones of a high radiation. It typically often leads to a plasma edge cooling and shrinking of the current profile (the plasma becomes unstable to kink and tearing modes). The basic idea is that when the radiation cooling due to high densities and a line radiation of impurities exceeds the plasma heating, the plasma cooling eventually leads to an instability. However, this understanding is not complete as an auxiliary heating not always avoids the instability. The processes behind the Greenwald limit are not yet completely understood, but the main findings indicates that it is associated with edge physics and depends mainly on edge temperature and density [36]. There are also indications that the Greenwald limit can be caused by a formation of magnetic islands at the plasma edge [37]. There are several ways how to overcome the Greenwald limit including a better wall conditioning (e.g. boronisation described in section 3.2.2 which subsequently leads to a lower amount of impurities in the plasma), scenarios with a peaked plasma density profile achieved by the pellet fuelling [38] (as injecting hydrogen isotopes into the plasma core leads to a more peaked profile than fuelling by the gas puff at the edge) or plasma shapes with different triangularities (which could influence the edge stability).

The runaway limit takes place when an accelerating electric force on electrons overcomes a friction by collisions. In this situation, the ohmic plasma heating is reduced and electrons are accelerated until they can hit and damage the tokamak vessel. Regions near the runaway limit are not interesting for tokamaks since a low density leads to a low rate of the fusion reactions. However, runaway electrons can appear as a side effect of disruptions, in particular during the mitigated disruptions when gas puff of inert gas is used to slow down and suppress the impact of disruption. Runaway electrons can appear when yhe plasma confinement is lost and the toroidal electric field is present (due to a change of current in coils and due to a rapid change or loss of plasma current).

2.6 Basic characteristics of MHD modes

Summarising the previous chapters, the MHD modes can be described by the mode numbers m, n, the radial structure and the growth rate γ. The growth rate γ represents an assumed exponential growth of the mode with the time $e^{\gamma t}$ and it is given by an imaginary part of eigenvalues of equation 2.23. The Mode numbers m, n represent a mode structure as a number of the local maximal perturbation in the poloidal and toroidal direction. As the mode numbers imply, the linear mode can only live close to rational numbers of $q = m/n$ due to a possible periodicity of perturbations. The radial structure of the mode is not so trivial to measure, but even information if it affects the boundary (external mode) or not (internal mode) can provide useful information about its nature.

If the mode rotates in the laboratory frame, its perturbation is also described by the measured frequency $\omega_{m,n}$ that is a combination of the toroidal and poloidal rotation [39]:

$$\omega_{m,n} = n\omega_\phi + m\omega_\theta \tag{2.43}$$

where signs of all components have to be taken into account, e.g. in the coordinate system with θ in the clockwise direction the equation 2.43 changes to $\omega_{m,n} = n\omega_\phi - m\omega_\theta$. The plasma rotation can be intrinsic (natural) or driven by an external torque. The intrinsic rotation can originate from pressure gradient and electric field as can be seen from an application of $\times\mathbf{B}$ to the equation $\nabla p_{e,i} = en_{e,i}\left(\mathbf{E} + \mathbf{v}_{e,i} \times \mathbf{B}\right)$:

$$v_{e,i} = \frac{\mathbf{E}\times\mathbf{B}}{B^2} - \frac{1}{en_{e,i}}\frac{\nabla p_{e,i}\times\mathbf{B}}{B^2} \tag{2.44}$$

and also from other effects still remaining in the active area of the research. The external torque can appear e.g. as a result of the NBI heating. Since the second diamagnetic term is much larger in the poloidal rotation than in the toroidal rotation and non-diamagnetic effects are strongly damped in poloidal rotation (as the varying magnetic field and collisions cause), the measured frequency of the MHD mode 2.43 can be approximated as [33]:

$$\omega_{(m,n)} \simeq n\left(v_\phi/R\right) + mv_{\theta,dia}/r \tag{2.45}$$

where the diamagnetic second term in 2.44 gives the poloidal rotation $v_{dia,\theta}/r$ whereas it is neglected in the v_ϕ.

Combining all the characteristics of the mode gives perturbation in the form [33]:

$$\xi(r,\theta,\phi,t) = \hat{\xi}(r)\cos(m\theta + n\phi - \omega_{m,n}t)e^{\gamma t} \tag{2.46}$$

which can be consequently seen as a perturbation of e.g. the measured radiation or electromagnetic field and characterised, if the measurement has a sufficient resolution and coverage in time and space.

3. Electromagnetic emission

This chapter overviews processes of electromagnetic emission in tokamak environment, their role in measurement of plasma parameters and impact on plasma performance.

3.1 Introduction

Electromagnetic radiation in tokamak plasmas represents major source of power losses as well as source of useful information about plasma parameters. There are various processes (covering free-free, free-bound as well as bound-bound emissions) generating radiation ranging from millimetre waves to hard X-ray radiation.

Depending on studied process or plasma parameter, diagnostic can focus on specific part of electromagnetic spectra (soft X-ray detectors, hard X-ray detectors, measurements of D-alpha radiation, etc.), observe interaction of electromagnetic radiation with plasma (interferometry, radiometry, Thomson scattering, etc.) or measure the whole spectrum (bolometers).

The main source of radiation losses is typically bremsstrahlung of hot plasma and line radiation of impurities. Loss of plasma energy due to the radiation can be unfavourable or beneficial depending on the region or situation. For example, radiation cooling near divertor region in the detachment regime (regime with formation of gas cloud in front of the divertor plates) can help to reduce large heat loads to divertor plates whereas radiation cooling in plasma core reduces rate of fusion reactions.

3.2 Types of electromagnetic emission

3.2.1 Bremsstrahlung

Bremsstrahlung (the English integrated German term for the "braking radiation") is a free-free emission resulting from the deceleration of charged particle deflected by another charged particle. Lost kinetic energy and momentum is transferred into radiation (photon) satisfying conservation laws. In the non-relativistic limit ($v/c \ll 1$), radiation fields from the like-particle collision exactly cancel [40] and bremsstrahlung radiation is generated by the electron-ion collisions. Spectral emission ϵ_ν of thermal bremsstrahlung of plasma with Maxwellian distribution can be derived from the Coulomb scattering as [41, 42]:

$$\epsilon_{\text{brem},\nu} = Z_{\text{eff}} n_e^2 \left(\frac{e^2}{4\pi\varepsilon_0}\right)^3 \frac{32\pi^2}{3\sqrt{3}m^2c^3} \left(\frac{2m}{\pi T}\right)^{1/2} \mathrm{e}^{-hv/T} \bar{g}_{ff} \tag{3.1}$$

or in the simplified form:

$$\epsilon_{\text{brem},\nu} = 6.3 \cdot 10^{-54} Z_{\text{eff}} n_e^2 e^{-h\nu/T_e} / \sqrt{T_e} \bar{g}_{ff} \qquad [Wm^{-3}s^{-1}] \tag{3.2}$$

where:

$$Z_{\text{eff}} = \Sigma_i Z_i^2 n_i / Z_i n_i \tag{3.3}$$

is the effective charge, n_e is electron density (m^{-3}), T_e electron temperature (eV), $h\nu$ energy of emitted radiation (eV) and $\bar{g}_{ff}$ the Maxwellian averaged free-free Gaunt factor with quantum-mechanical corrections. The value of $\bar{g_{ff}}$ is approximately one for $h\nu/T_e \sim 1$ (i.e. in the SXR region) and it is in the range from 1 to 5 for $10^{-4} < h\nu/T_e < 1$ (ranging from 2 to 5 in the visible region) [41]. Values for $h\nu/T_e \gg 1$ are not important as bremsstrahlung emissivity is negligible for these frequencies [43, 44].

Integration over frequency gives the formula for the total power flux of the bremsstrahlung radiation:

$$P_{\text{brem}} = 6.3 \cdot 10^{-53} Z_{\text{eff}} n_e^2 \bar{g} \sqrt{T_e} \qquad [Wm^{-3}]. \tag{3.4}$$

There is a low-frequency limit of the applicability of the relation 3.1 given by combination of plasma frequency $\omega_p = \sqrt{\frac{ne^2}{\epsilon_0 m_e}}$ and cyclotron frequency $\omega_c = \frac{eB}{m_e}$ depending on mutual direction of magnetic field and electromagnetic wave. Dispersion relation and frequency limits can be found e.g. in [5]. Under these limits, electromagnetic radiation undergoes strong reabsorption leading to thermal equilibrium where emission starts to follow the black body radiation:

$$\epsilon_\nu = \frac{8\pi h\nu^3}{c^2(e^{\frac{h\nu}{T_e}} - 1)}. \tag{3.5}$$

In tokamaks, these limits lay in the region of radio waves and have negligible impact on the relation of total bremsstrahlung radiation 3.4.

Relativistic effects can be neglected as $v/c \ll 1$ for most particles in tokamaks which can be also seen from the approximated formula for the relativistic bremsstrahlung derived in [45] (more details can be found in [44]):

$$P_{\text{brem,rel}} \simeq P_{\text{brem}}(1 + 5.1 \cdot 10^{-6} T_e) \tag{3.6}$$

where T_e (eV) in tokamaks typically reaches several keV.

Diagnostic tool issues

In fusion plasma devices, bremsstrahlung emission covers broad continuous range of spectrum from visible to soft X-ray (SXR) radiation and presents a source of valuable information about plasma such as effective ion charge, MHD activity, concentration of plasma impurities and their transport (however, contribution of line radiation is often higher than contribution of Z_{eff} in 3.1 or 3.4), an estimate of plasma position, electron temperature, etc.

Effective ion charge can be estimated from equation 3.1 when electron temperature, density and part of bremsstrahlung spectra is known. Region of measured spectra is chosen so that it doesn't contain any spectral lines. At most tokamaks (JET, ASDEX, DIII-D and COMPASS) region with wavelength of cca 2nm around 523.5nm is selected.

MHD activity can be detected from bremsstrahlung due to the related perturbation of electron temperature and density. Typically, core MHD activity is detected via SXR detectors as bremsstrahlung is significant source of emission in the SXR region (due to temperature reaching several keV) whereas lower energies are radiated mainly from plasma edge and are mixed with other radiation processes which makes plasma perturbations more difficult to recognise. It has to be also taken into account that the SXR bremsstrahlung in the plasma core is often mixed with line radiation of heavy impurities.

Bremsstrahlung can also serve to measure electron temperature when slope of its spectrum (given by $\exp\left(-h\nu/T_e\right)/\sqrt{T_e}$) is found [41] (at least the part which is not disturbed by the recombination and line radiation) or from ratio of two or more measurements with appropriately different spectral sensitivity (usually, the lower limit of the measured energy spectrum is given by thickness of a beryllium filter) as the ratio depends only on T_e. However, bremsstrahlung spectrum is usually mixed with other sources of radiation in tokamaks.

Non-thermal bremsstrahlung can also appear in tokamaks when fast (suprathermal) particles (e.g. runaway electrons) leave plasma and hit a wall. It is usually detected by the hard X-ray detectors.

3.2.2 Line radiation

Despite high temperatures in the plasma core (in order of keV), plasma edge contains non-negligible populations of neutral hydrogenic species due to relatively low electron temperatures (tens of eV), plasma interaction with first wall and transport phenomena. Ideally, such hydrogen isotopes would be the only source of line radiation, but plasma impurities are unavoidable. Impurities with higher atomic number Z can keep bound electrons up to high electron temperatures present in the plasma core. Their ionization and subsequent emission of line radiation can lead to significant cooling and degradation of plasma performance or even termination of a plasma discharge. One of the main contributors to plasma impurity density is interaction of plasma with a first wall. Therefore, material of the first wall determines elements of significant part of impurity populations in plasma. A choice of such material is restricted by its performance in harsh conditions as exposure to high power fluxes (in order of $10\mathrm{MW/m^2}$), neutron fluxes or ionisation radiation damage. Another source of contamination of plasma are residual particles from atmosphere such as oxygen and nitrogen after vacuum vessel opening. There are several ways how to reduce influx of impurities from vacuum vessel including so-called boronization, .i.e deposition of a thin layer of carborane ($C_2B_{10}H_{12}$) on the first wall during glow discharge. Measuring of impurities provides useful information conditions of the first wall of a tokamak. The intensity of plasma-wall interaction and edge plasme radiation can indicate important plasma processes like transition to the high confinement mode (L-H transition) or presence of edge localized mode (ELM).

Total radiation power per unit volume produced by line radiation can be expressed as:

$$P_{\text{line}} = n_e \Sigma_i n_i L_i, \tag{3.7}$$

where L_i [$\mathrm{Wm^3}$] is the line radiation cooling factor for ion population i. Unfortunately, due to the complexity of atomic processes, calculation of L_i is very complicated and therefore simplified assumptions are used in practice. One of the simplifying applicable assumption is the average ion model [46] where ions of high-Z elements are replaced by averaged ion to treat complicated and still not fully described (in case of high-Z elements) atomic processes. In the plasma core the radiation can be characterised with complicated CRSS models or under some circumstances by simpler CE. The constrains for the models are determined by ratios of atomic collision rates [47]. The situation is more complicated in the region of plasma edge where plasma transport of impurities dominates over relaxation times of excited ion states (especially during ELMs) and therefore, time-dependent models have to be applied, e.g. non-coronal model described in [48] where L_i depends also on $n_e\tau_i$ where τ_i represents effective impurity residence time in plasma.

Diagnostic tool issues

Measurement of the D_α emission (line radiation produced by Balmer-alpha transition from 3rd to 2nd lowest energy level in the deuterium atom) is the basic and widely used diagnostic in tokamaks as it provides information on intensity of plasma-wall interaction when deuteron escapes confined plasma and recombines with electron to form a deuterium atom which subsequently falls to lower energy state. Therefore, measurement of D_α emission can serve as good indicator of L-H or H-L transition, ELM or other turbulent behaviour in the region of plasma edge. ELMs are also well pronounced on measurements of spectral lines of impurities present in the first wall such as Beryllium or Boron after boronization. Actually, line radiation of elements from first wall components can be better than D_α as they can exhibit higher contrast between the intensive plasma-wall interaction during ELMs (caused e.g. by material sputtering) and the less intensive plasma-wall interaction during the inter-ELM phase. Diagnostics measuring the line radiation in tokamaks are usually based on photo-multipliers with an interference filter.

Besides information about presence or concentration of particular impurities, measuring spectral lines of impurities can also serve as measurement of plasma rotation or ion temperatures due to the the Doppler effect. Regions of the measurement are given by local temperatures (under assumption that thermalisation overcomes transport of particles) determining distribution of ionisation states. For example, at COMPASS, poloidal rotation and ion temperature in the plasma edge can be derived from measurements of line radiation of two times ionised carbon by diagnostic consisting of collecting optics, high resolution spectrometer and CCD camera [49]).

Several diagnostics are based on intentional injection of impurities into plasma to observe their line radiation. For example lithium-beam emission spectroscopy (Li-BES) [50], [51], [52] measures line radiation of lithium. In the Li-BES diagnostic, lithium atoms are extracted from a thermionic ion source, accelerated and neutralised (in sodium vapour) so that they can reach plasma without being deflected by the tokamak magnetic field. Interaction of the beam with plasma excites its lithium atoms to higher energetic states emitting photons during spontaneous emission. Since the intensity of this emission is proportional to local electron density, it can provide electron density profile. Intensity of Li emission is usually measured using an appropriate interference filter and detector system e.g. the CCD camera, Photomultiplier or Photodiode or Avalanche Photo Diode.

3.2.3 Radiation from recombination processes

The term recombination covers several processes during which an electron is captured by an ion like radiative recombination (free electron recombines with an ion while a photon takes the extra energy and momentum), three-body recombination (two electrons and an ion interact so that one electron is captured and the second remains free with extra energy), dielectronic recombination (free electron captured providing its energy to excite another bound electron) and charge exchange recombination (electron jumps from one ion to another). Electromagnetic emission is produced immediately only by the radiative recombination while others can lead to excited electrons emitting line radiation (described in the previous section 3.2.2) during subsequent spontaneous emission.

The radiative recombination contributes to a continuum spectrum with energies higher than electron binding energies (the limit can be slightly lower due to the quantum lowering [47]) as it it can be seen form the energy-conservation equation of the interaction (for hydrogen-like ions):

$$h\nu = \frac{1}{2}mv_e^2 + \frac{Z^2 R_y}{n^2} \tag{3.8}$$

where R_y is Rydberg constant (13.6 eV), Z charge of an ion, n principal quantum number and v_e velocity of an electron. Spectral emissivity can be derived from 3.8 and Maxwellian distribution of electrons to the form similar to the Bremstrahlung emissivity $\epsilon_{\nu,\mathrm{brems}}$ given by 3.1 [41, 53]:

$$\begin{aligned} &\epsilon_{\nu,\mathrm{rec}} \propto \mathrm{e}^{E_i/T_e}\epsilon_{\nu,\mathrm{brems}} && \mathit{for} \quad \epsilon_\nu > \xi_i \\ &\epsilon_{\nu,\mathrm{rec}} = 0 && \mathit{for} \quad \epsilon_\nu < \xi_i \end{aligned} \tag{3.9}$$

where E_i is ionisation potential of given ion. Total recombination radiation is summation over ionisation states and types of ions (exact formula is rather complex and it can be found e.g. in [41, 53]). As it is obvious from 3.9, the radiative recombination becomes noticeable for lower temperatures or in the presence of impurities with higher Z, i.e. for T_e close to the binding energies.

Diagnostic tool issues

In tokamaks, favourable conditions for recombination processes typically occur in the divertor region, especially during the detachment regime, during plasma wall interaction and in the scrape-of layer (region with magnetic field lines ending on a material surface). During a detachment regime, recombination is a key process for creation of cloud of neutral particles helping to shield divertor plates and smoother redistribution of heat flux. In the case of plasma wall interaction, neutralisation of hydrogen isotopes allows measurement of their characteristic lines which can give information about the intensity of the plasma wall interaction. Inverse ionization processes can subsequently return particles to a confined plasma (plasma recycling). Mostly line radiation of bound electrons is useful for diagnostic purposes as it was described in the chapter 3.2.2. Another example is e.g. charge exchange recombination spectroscopy (CXRS) using charge exchange recombination between particles of diagnostic beam injected into plasma and plasma impurities for measurement of their temperature (from line broadening) or rotation (from the Doppler shift of spectral lines).

3.3 Role of electromagnetic emission in plasma performance

Electromagnetic emission has an important role in a plasma performance as it represents a considerable fraction (seferal tens of %) of its power losses. The power balance in tokamaks can be written as:

$$P_\Omega + P_{\text{ext}} + P_\alpha = \frac{\partial}{\partial t} W + P_{\text{transp}} + P_{\text{rad}} \tag{3.10}$$

where P_Ω is the ohmic heating, P_{ext} the heating of external power sources, P_α the heating by alpha particles from thermonuclear reactions, W the plasma thermal energy and P_{transp} the transport power losses. The ohmic heating depends mainly on temperature and effective ionic charge as $P_{OH} = \eta j^2$ where $\eta \propto f(Z_{\text{eff}})Z_{\text{eff}} \ln\Lambda\, T^{-3/2}$ and f is a numerical factor between 1 (for $Z = 1$) and 0.58 (for $Z = \infty$) [1]. The plasma resistivity can be also increased by drifts, turbulences (anomalous resistivity) or effects caused by trapped particles. In contrast to the radiation losses, dependence of the plasma resistivity on its density is negligible (logarithm of the square root inside the Coulomb logarithm) and for higher plasma densities, the radiation losses could exceed the ohmic heating. As the plasma temperature increases towards higher (fusion relevant) temperatures, the ohmic heating becomes ineffective (for technically achievable plasma currents and magnetic fields) and the plasma is usually heated predominantly by auxiliary heating and by alpha particles which can be expressed as (for the D-T reaction, i.e. reaction between deuterium and tritium) $P_\alpha = n_D n_T \langle\sigma v\rangle E_\alpha$ where $\langle\sigma v\rangle$ is the averaged D-T fusion fate coefficient and E_α the energy of the alpha particle from the D-T reaction [1].

Power losses due to the electromagnetic emission can be expressed by summarising all types of radiation in the previous chapter 3.2 in the form:

$$P_{\text{rad}} = P_{\text{line}} + P_{\text{brems}} + P_{\text{recomb}} = n_e^2(R_{\text{line}} + R_{\text{brems}} + R_{\text{recomb}}) = n_e^2 R_{\text{rad}} \tag{3.11}$$

where the R terms depends on T_e , Z_i and except R_{brems} also on ionisation states (and weakly on plasma density) [41].

Besides radiation, the plasma losses a significant amount of energy due to the transport $P_{\text{tranps}} = \nabla \cdot J$ where J is the heat flow due to conduction and convection. These losses can be expressed via the energy confinement time, defined as:

$$\tau_E = \frac{W}{P_{\text{heat}} - dW/dt} \tag{3.12}$$

where P_{heat} is the total heating power, i.e. the denominator represents the power losses. For practical reasons, the radiation losses are sometimes excluded from the energy confinement time as statistical studies have shown that it leads to a more reliable empirical fit and it also allows for a better description and prediction of P_{transp} via scaling of τ_E [54].

The radiation losses can exceed the plasma heating when the plasma density or the concentration of impurities increases above critical values (as it can be derived from equation 3.10). It typically occurs locally but it can lead to instabilities causing a termination of the whole plasma discharge. The global limit for the plasma density was found empirically as the Greenwald limit described in section 2.5 and it can be found below the limit given by the radiation [55].

At higher temperatures and with a low impurity contamination, the radiation losses are caused mainly by bremsstrahlung which is exceeded by the alpha heating at 4.4 keV (ideal ignition) as the alpha heating increases much more rapidly, see Fig 3.1 (otherwise, the tokamaks could not be considered as a potential source of energy) and the effect of thebremsstrahlung losses on ignition decreases [3].

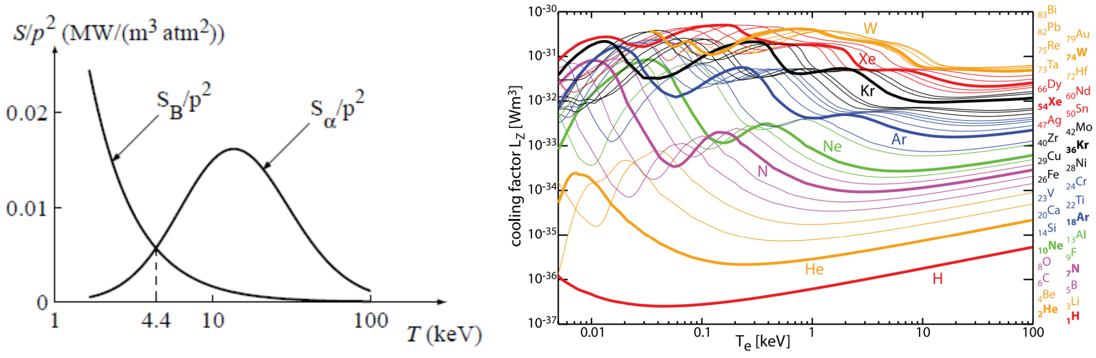

(a) (b)

Figure 3.1: (a) Heating by alpha particles (S_α) and bremsstrahlung radiation losses (S_B) normalised by pressure as a function of the temperature [3]. The intersection point corresponds to the ideal ignition when the plasma can heat itself by the fusion reactions. (b) Line radiation cooling factors for different elements with respect to the plasma temperature [56].

The radiation losses represent an unavoidable significant part of the power losses and can be only lowered by a reduction of plasma impurities, in particular the ones with a higher atomic number, see Fig. 3.1b. On the other hand, the density of the power losses caused by particles reaching the first wall or the divertor can be reduced significantly which is important for the divertor region as it will be described in the following part.

3.3.1 Detachment regime

Reduction of heat flux reaching plasma facing components is essential for prolonging lifetime of plasma facing components and improvement of plasma performance. Normally, particles entering SOL are directed along magnetic field lines to the divertor plates as it is illustrated in the Fig. 3.2. During the detachment regime, a ”cloud” of neutrals is formed in front of the divertor plates which allows volumetric power losses via radiation. The detachment regime can be achieved under increased plasma densities when more impurities are released by plasma facing components which increases radiation losses. As the temperature in the divertor region decreases (< 5 eV), electrons and ions can recombine to form neutrals. These recycled neutrals help to shield the divertor plates from the heat flux leaving the confined plasma via (volumetrical) radiation losses. The detachment regime can be improved by a puff i.e. “seeding” of impurities into the divertor region to increase radiationlosses and cooling in the divertor region. Another advantage of the detachment regime is more efficient pumping of helium ash due to the higher neutral particle densities established in the divertor region in front of the pumps [57]. Disadvantage is that neutral particles and impurities from the divertor region can penetrate into the confined plasma which can increase plasma radiation losses or even destabilise plasma by rapid asymmetric increase of radiation and plasma cooling, i.e. by multifaceted asymmetric radiation from the edge (MARFE) instability. Probability of MARFE can be reduced by partial detachment when only inner part of divertor (inner strike point) is detached. Distribution of plasma radiation during experiments aimed at plasma detachment at COMPASS are analysed in the section 5.2.5.

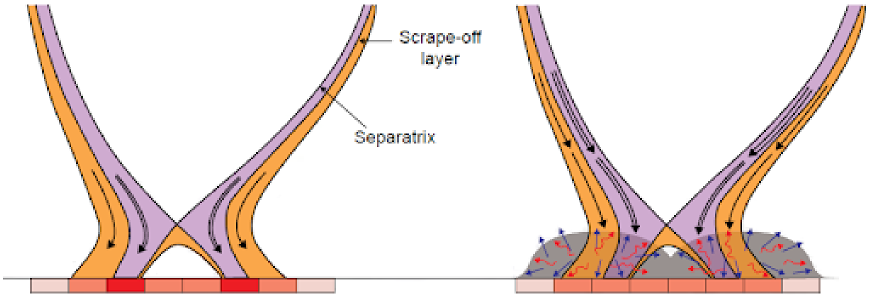

Figure 3.2: Localised (left) and volumetric (right) losses of plasma energy in the divertor region (long black arrows illustrates plasma flux, blue arrows represent neutral atoms and red arrows radiation losses) [57]

.

4. Simulation of MHD equilibria

The chapter describes reconstructions of MHD equilibria performed with the FIESTA code [58] and its contributions to COMPASS experimental campaigns and impact on COMPASS-U design.

4.1 Introduction

Reconstruction of MHD equilibrium is important in many areas of fusion research since plasma is confined by the magnetic field defining plasma shape, influencing its performance and affecting its stability. For this reason the knowledge of MHD equilibrium is crucial for both experiment design and plasma control, but also for physics studies of experimental results. One example is improvement of accuracy of tomographic reconstructions in the next chapter 5.

In this chapter, reconstructions of MHD equilibria are performed by the Fiesta code [58], which was at first applied at COMPASS to design coil current waveforms to achieve higher values of upper triangularity of upper triangularity and subsequently compared with equilibrium reconstructions obtained with EFIT, which is run routinely as a post-discharge analysis and uses signals measured by coils. The second part of the chapter describes application of the Fiesta code as a main tool used in the process of design of equilibrium and coils for the COMPASS-U tokamak. In order to find more optimal solution of coil current combinations, Tikhonov regularisation (available in Fiesta) is applied and described. Factor evaluating vertical stability of plasma is also presented.

Reconstructing MHD equilibria requires solving the Grad-Shafranov equation 2.13 (here repeated in convenient form):

$$\nabla^* \psi = -\mu_0 j_\phi = -\mu_0 R^2 p'(\psi) - \mu_0^2 f(\psi) f'(\psi) \tag{4.1}$$

where

$$f = B_\phi R. \tag{4.2}$$

The presence of Ψ on both sides of the equation makes the problem nonlinear and iterative methods have to be applied to find a solution, including boundary conditions. Basically, Grad-Shafranov solvers can be classified as either fixed boundary or free boundary solvers. Fixed boundary solvers have prescribed solution or its derivative on the edge of the domain on the input (e.g. codes such as Helena [59], Chease [60], Scene [61], etc.). Free boundary solvers are usually used when there are known currents outside plasma, but plasma shape itself is unknown except some definition where the boundary is (e.g. EFIT [62], Fiesta [58], Freebie [63], Topeol [64], etc.).

In order to provide MHD equilibria, the Fiesta code (written in MATLAB) can be applied both as a forward equilibrium solver and as a inverse (EFIT) solver. The former method finds equilibrium iteratively by repeating the following steps until satisfactory convergence is reached:

- proposing current density profile j_ϕ as a function of Ψ using given p' and ff' and set to zero outside plasma boundary

- evaluation of updated ψ consisting of ψ_{plasma} due to the plasma and Ψ_{ext} due to the external coils
- determination of the plasma boundary (usually either a limiter or saddle point, i.e. X-point)

whereas the latter (inverse) solver also finds current density profile in the form proposed by [62]:

$$\begin{aligned} p' &= \sum_{i=1}^{n} \alpha_i \Psi^i \\ ff' &= \sum_{i=1}^{n} \beta i \Psi^i \end{aligned} \tag{4.3}$$

by means of the least squares fit (using SVD) of α and β parameters so that the solution fits measured poloidal magnetic flux (or its derivations in form of magnetic field measured by coils).

Basically, the main distinction for the user between both the methods is that the forward (standard Fiesta) solver works with the proposed shape of the current profile (i.e. proposed shape of p' and ff' where amplitude of profile can change) and finds coil currents to fit requirements whereas the inverse (EFIT) solver can fit more parameters including parameters of plasma current profile, currents in coils and conductors, pressure, etc. in order to find equilibrium.

4.2 Equilibria for the COMPASS tokamak

This section compares two different codes with different methods to reconstruct equilibrium at the COMPASS tokamak: the Fiesta code applied as forward predictive equilibrium solver and the EFIT code which is typically applied during post-discharge analysis from measured data.

The COMPASS tokamak is a device with ITER-like shape, two Neutral Beam Injection (NBI) heating systems and accesible H-mode [65, 66]. The main parameters of COMPASS are summarised in Tab. 4.1.

Toroidal mag. field	$B_T = 0.9 - 1.7$ T
Plasma current	$I_p \leq 350$ kA
Major radius	R = 0.56 m
Minor radius	a = 0.23 m
Plasma shape	D, circular, elliptical
Elongation	$\kappa \leq 1.8$
Discharge duration	≤ 500 ms
Plasma volume	V = 0.6 m^3
Plasma surface	S = 5.5 m^2
NBI heating power	$P_{NBI} = 2 \times 0.4$ MW

Table 4.1: Main engineering parameters of the COMPASS tokamak [65].

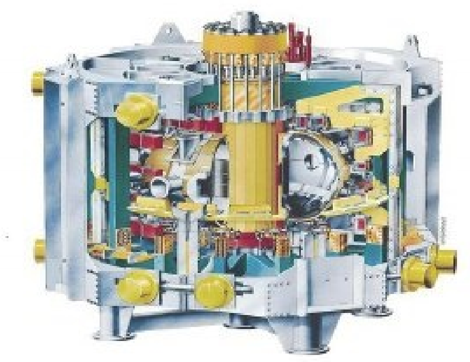

Figure 4.1: Cut through the the COMPASS tokamak.

At COMPASS, MHD equilibria are routinely reconstructed by the EFIT++ code (written in C++ with computational core in Fortran 95 [67]) from measurements of 16 internal partial Rogowski coils (measuring poloidal magnetic field around the vessel, i.e. spatial derivative of reconstructed Ψ), currents in the poloidal field coils circuits (shown in Fig. 4.2a), plasma current and toroidal magnetic field [67]. Plasma current is fitted according to the relations 4.3 with $n = 1$ and zero values at the plasma edge.

In this section, Fiesta is applied as forward equilibrium solver calculating equilibrium for given currents in PF coils, toroidal magnetic field (currents in TF coils), total plasma current and coefficients α_i, β_i in 4.3 defining plasma current profile. Coefficients α_i, β_i are only normalised (by the same value) so that the required total plasma current can be fitted inside the reconstructed plasma boundary. In order to avoid problems with convergence, currents in selected minority of PF coils (see Fig. 4.2a) are not only input, but they are also fitted so that the equilibrium is reconstructed for requested position of magnetic axis. The request for plasma position is introduced by constraining the reconstructed equilibrium to the same ψ above and below the supposed magnetic axis.

An example of MHD reconstruction of the Fiesta code and EFIT++ code for COMPASS is shown in Fig. 4.2a. In this case, proposed current profile adopted coefficients from by EFIT ($\alpha_1 = 1.93 \times 10^6$, $\beta_1 = 1.37$) and the difference is mainly in upper and lower parts of separatrix on the HFS side (where separatrix from Fiesta is about 1 cm closer to the wall).

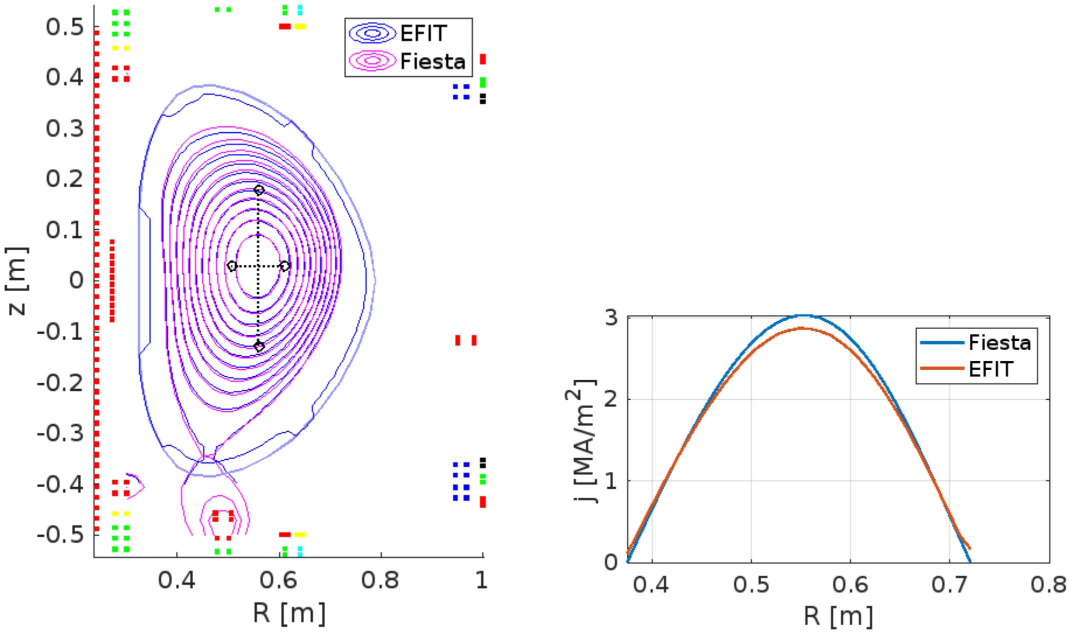

(a)

(b)

Figure 4.2: Equilibrium reconstructed by Fiesta and EFIT (a) and current profiles (b) for discharge #9778, time = 1100 ms. Fiesta equilibrium was reconstructed for applied currents in the shown coils except cyan and black coils which were fitted to find equilibrium at required position by means of fulfilling condition of the same Ψ at the edges of dotted lines. Current profile from EFIT served as input. Fiesta converged into slightly different coefficients (with amplitudes decreased by 2%) of current profile ($\alpha_1 = 1.83 \times 10^6$, $\beta_1 = 1.31$).

The result in Fig. 4.2b provides a comparative information about performance of Fiesta and EFIT since Fiesta applies the same coefficients of plasma current profile as EFIT. These coefficients were fitted by means of measurements of poloidal magnetic field. The Fiesta code allows for a user friendly way how to predict equilibria during experiments. At COMPASS, experiments with increased upper triangularity were performed in order to study its effect on plasma performance and instabilities. In order to extend range of achievable upper triangularities, an additional power source was used to increase the current in the upper PF coil circuit as it is shown in Fig 4.3a. The effect was simulated by implementing additional virtual coil into Fiesta simulations taking inputs in the form of currents in the PF coils during standard discharge (# 9778) and distribution of plasma current. Resulting plasma shapes and upper triangularities are shown in Fig. 4.2 where upper triangularity changed from 0.24 up to 0.14 or 0.34 (depending on applied current ±4 kA) for standard plasma current of 180 kA and the difference from EFIT was about 0.04. There was also change in the radial position and the position of x-point which was eventually slightly compensated by the feedback control (from predicted up to ±1 cm to ±0.3 cm).

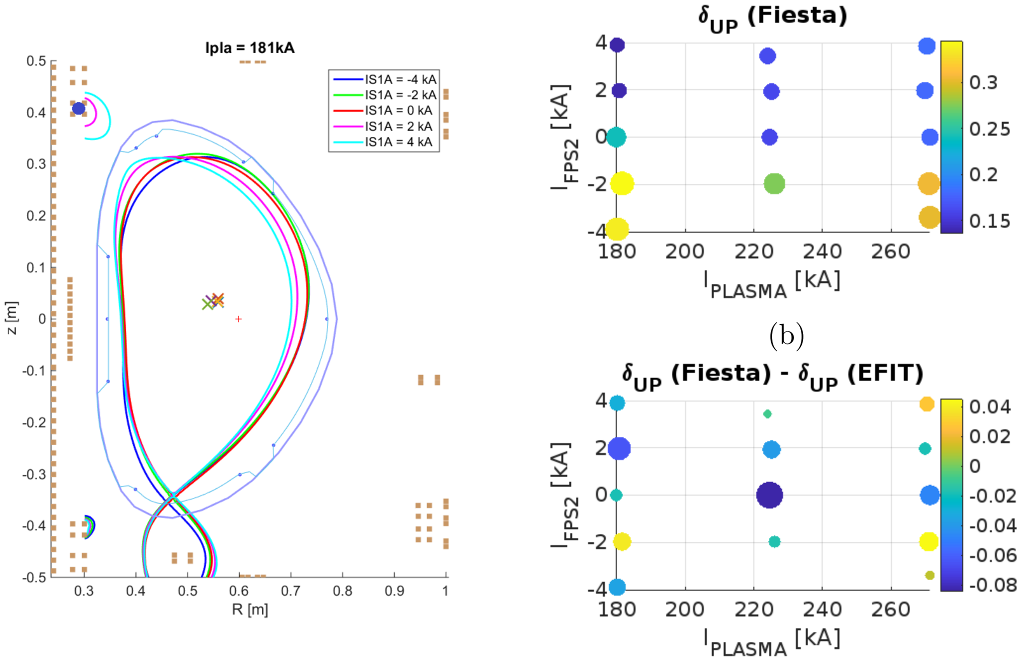

(b)

(a)

(c)

Figure 4.3: Effect of additional coil marked by blue dot (top left) on plasma boundary predicted by Fiesta simulations (a) and scan of plasma triangularity given by Fiesta and EFIT over current in the additional coil and plasma current represented by dot color and size.

4.3 MHD equilibria for COMPASS-U

Experience with Fiesta gained during simulations performed for COMPASS allowed to expand its application to the COMPASS-U project. Its aim is to study plasma performance with high parameters (see Tab. 4.2) and variable scenarios such as negative triangularity or snowflake configurations.

Following sections describe predictive simulations of equilibria for COMPASS-U and optimisation of coil geometry by means of the Fiesta code. Introduction to the chapter includes description of the COMPASS-U tokamak and a method of the MHD reconstruction. Following sections describe application of Tikhonov regularisation as a method of optimisation of the PF coils, plasma scenarios and calculation of vertical stability.

4.3.1 Introduction

The COMPASS-U tokamak is designed as a high magnetic field device (up to $B_{\mathrm{T}} = 5\,\mathrm{T}$) aimed to support ITER operation and to address challenges of the design of the DEMO reactor [68, 69]. Its main parameters are summarised in Tab. 4.2. One of the important steps during a tokamak design is to perform simulations of required MHD equilibria. It provides information about needed coil currents which is a vital input for requirements on power sources, cooling, exerted forces on machine structure, etc.

Toroidal mag. field	$\mathrm{B_T} \leq 5\mathrm{T}$
Plasma current	$I_p \leq 2$ MA
Major radius	R = 0.9 m
Minor radius	a = 0.27 m
Triangularity	$\delta \leq 0.6$
Elongation	$\kappa \leq 1.8$
Flat top length	1-10 s
Plasma volume	$\mathrm{V} = 2.1\ \mathrm{m}^3$
Plasma surface	$\mathrm{S} = 13\ \mathrm{m}^2$
NBI heating power	$\mathrm{P_{NBI}} = 8$ MW
ECRH heating power	$\mathrm{P_{ECRH}} = 10$ MW
Vessel temperature	300°C (goal 500°C)

Table 4.2: Main engineering parameters of the COMPASS-U tokamak design [69].

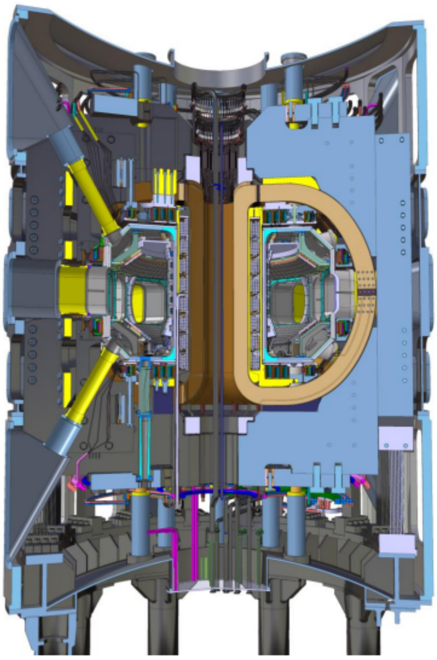

Figure 4.4: Cut through the preliminary design of the COMPASS-U tokamak.

To perform such simulations for COMPASS-U in the Fiesta code, it has to be applied in the opposite way than in the previous chapter. The required equilibrium is specified as the input of a simulation and coil currents are obtained as results. Simulation inputs, see Fig. 4.5, included major plasma parameters, as for example plasma shape, plasma current profile, toroidal magnetic field, etc.. To enhance the accuracy of Fiesta results, it is coupled with METIS [70], a fast transport solver which combines 0D scaling-law normalising heat and particle transport with 1D current diffusion modelling and 2D equilibria. The Fiesta code implements the current profile from METIS in the form of p' and ff' profiles, i.e. coefficients for their spline interpolation. Since Fiesta and METIS use different coordinate systems (see Fig. 4.6b) a special care has to be taken to transfer information between the two codes correctly. The values of p' have to be multiplied by -1 due to the change of sign of $d\psi$. The sign of ff' has to be also changed due to the change of sign of $d\psi$ and B_T. Moreover, METIS applies normalisation of ψ by 2π whereas Fiesta considers whole poloidal flux. Therefore, p' and ff' have to be multiplied by 2π.

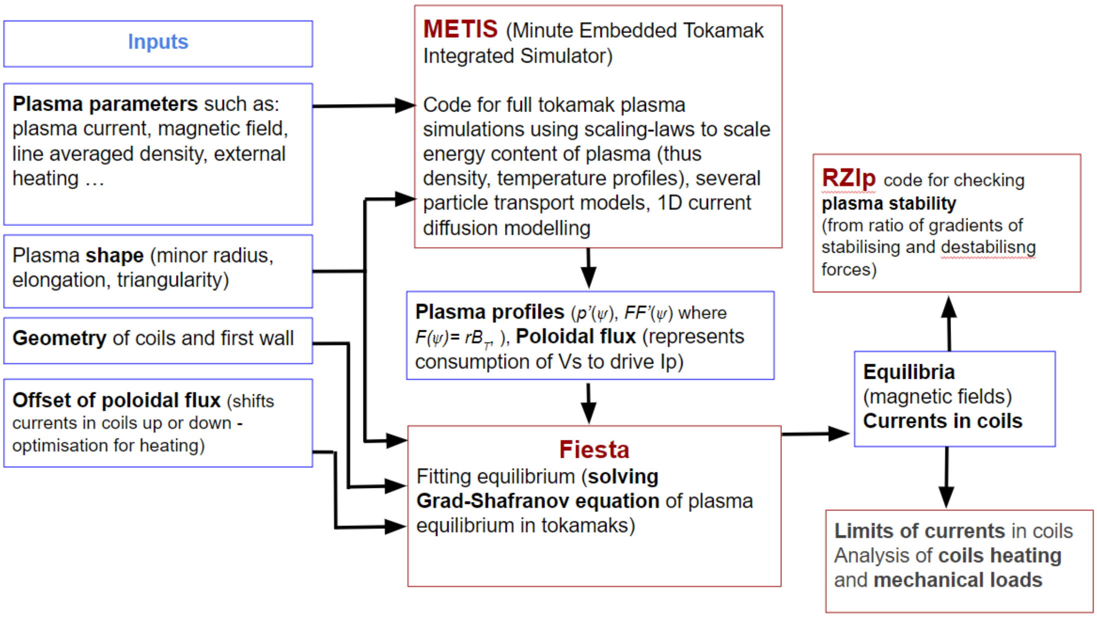

Figure 4.5: Simulations of equilibria in Fiesta with inputs from METIS

Under appropriate weighted constraints, optimal coil currents for required equilibria can be calculated by Tikhonov regularisation technique [71, 72, 73, 74] described in the next section 4.3.2. Plasma scenarios in the next sections were found by introducing following constraints as it is illustrated in Fig. 4.6a:

plasma shape: Specified by several points lying on the separatrix.

null point: Is a point with zero value of poloidal magnetic field. A null point is not neccessarily an x-point and can be positioned outside of separatrix.

X-point: Is a null point which has to be lying on the separatrix.

regularisation par.: Is a parameter for Tikhonov regularisation described in the sec 4.3.2.

poloidal flux ofset: Offset of the poloidal flux ψ.

The separatrix shape for the required plasma parameters was either calculated or taken from METIS and the separatrix points determined with two different approaches. In the section 4.3.4 (finding conservative solution) the points were evenly distributed along the contour. The second approach applied in 4.3.5 used a reduced number of points placed at specific locations to reach specific requirements as clearance from the first wall or certain value of triangularity. An example of the application is shown in Fig. 4.6a. The null point in top region was introduced in order to avoid formation of upper X-point (as requiring zero poloidal field under separatrix can lead to lower upper plasma boundary). Regularisation parameter was adjusted manually together with constraints (shown in Fig. 4.6a) and their weights. Offset of poloidal flux is set at plasma centre from METIS scalings and reflects change in coil currents to drive current in plasma while keeping the same plasma shape.

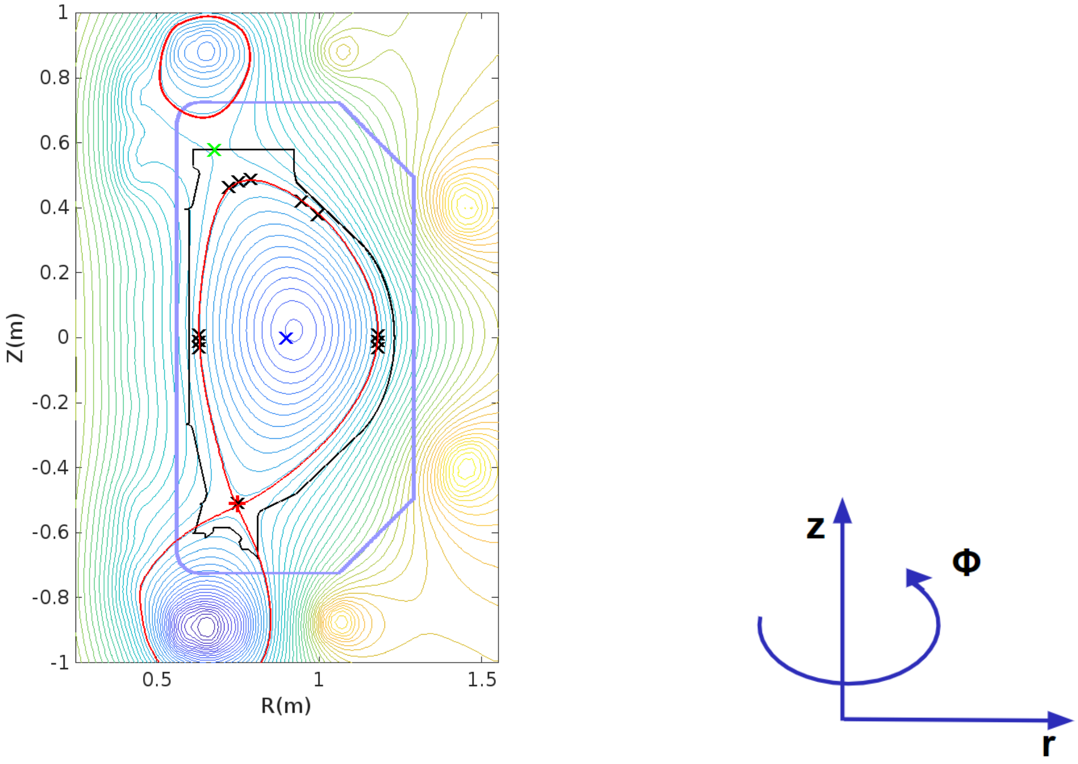

(a)

(b)

Figure 4.6: Illustration of applied requirements (a): points at separatrix as black crosses, position of null point by green cross, position of x-point by red cross and position where poloidal flux offset from METIS is required by red cross and convention of coordinates used in Fiesta (b).

4.3.2 Tikhonov regularisation

Regularisation methods are typically applied to avoid over-fitting or to solve ill-posed problems during inversion. In the Fiesta code, an optimized solution can be found by Tikhonov regularisation [71, 72, 73, 74] which is also key technique for the tomographic reconstruction in the chapter 5 where it is described more in detail. Fiesta implements Tikhonov regularisation as minimization of the form:

$$\|\mathbf{b} - \mathbf{A}\mathbf{x}\|_2^2 + \alpha^2 \|\mathbf{x}\|_2^2 \tag{4.4}$$

where $\mathbf{A}$ is the response matrix, $\mathbf{b}$ is the vector of expected signals, α is the regularisation parameter and $\mathbf{x}$ is the solution. The response matrix can represent green functions corresponding to the required poloidal flux at specified locations and the given poloidal field coil configuration. The expected signals $\mathbf{b}$ can be for example poloidal field at given locations. The nature of found solution, of coil currents for example, is influenced by the regularisation parameter. The higher the parameter α, the smaller the norms of x.

Decomposition $\mathbf{A} = \mathbf{U}\Sigma\mathbf{V}^T$ allows to find a solution as:

$$\mathbf{x} = \sum_{i=1}^{N} \phi_i \frac{u_i^T b}{\sigma_i} v_i \tag{4.5}$$

where u_i^T is i-th column of matrix $\mathbf{U}^T$, σ_i i-th element of diagonal matrix, v_i column of matrix $\mathbf{V}$ and

$$\phi_i = \frac{\sigma_i^2}{\sigma_i^2 + \alpha^2}, i = 1, \cdots, N \tag{4.6}$$

i.e. higher α values suppress components associated with smaller singular values of the response matrix $\mathbf{A}$ since ϕ_i closes to unity for $\sigma_i^2 \gg \alpha^2$ and falls to zero for $\sigma_i^2 \ll \alpha^2$ (with $\alpha = 0$ the regularisation acts as SVD pseudo-inverse).

4.3.3 Vertical stability parameter

There are several definitions of the stability parameters [75, 76, 77]. The stability parameter applied in this chapter is defined according [75] as the ratio of the stabilizing force gradient along vertical axis (due to the eddy currents in the vessel and stabilising plates) F'_s to the destabilizing force gradient acting on the system (due to the currents in coils) F'_d [75]:

$$f_s = \frac{F'_s}{F'_d} = \frac{[\mathbf{I}_p]^T \left[\mathbf{M}'_{p,s}\right] [\mathbf{M}_{s,s}]^{-1} \left[\mathbf{M}'_{s,p}\right] [\mathbf{I}_p]}{[\mathbf{I}_p]^T \left[\mathbf{M}''_{p,c}\right] [\mathbf{I}_c]} \tag{4.7}$$

where $\mathbf{I}_p$ are current vectors, $\mathbf{M}$ inductance matrices and subscripts p, s, c represent plasma, stabilisation conductors, poloidal field coils respectively and ' is differentiation with respect to the vertical axis. Relations of f_s values to stability are summarised in Tab. 4.3. The condition $f_s < 0$ represents the stable region with the negative growth rate of vertical plasma movement. The unstable region with $f_s < 1$ is dominated by plasma inertia where plasma movement occurs on Alfvén time-scale and stabilisation would require very fast active feedback. In the region with $f_s > 1$, the plasma displacement growth rate is mainly given by L/R of passive structures. The condition $f_s > 1.5$ is regarded as a value with sufficient margin for design purposes [75]. Stability parameters for several MHD equilibria are shown in Tab. 4.5.

condition	**stability**
$f_s < 0$	stable (negative growth rate)
$0 < f_s < 1$	growth rate dominated by plasma inertia
$f_s > 1.0$	growth rate dominated by L/R of passive structures
$f_s > 1.5$	acceptable for design

Table 4.3: Relation of f_s values to stability [75].

4.3.4 Optimisation of coil geometry

Geometry of the PF coils is supposed to be designed so that it can efficiently generate required MHD equilibria under engineering constraints (e.g. coil current limits, heat loads, mechanical stresses). In this section, simulations of MHD equilibria are used to asses several variants of the coil geometry with respect to the required coil currents (which is connected to other engineering constraints as coil currents cause mechanical stresses and heating of coils). There are two principal positions a PF coil can have with respect to the TF coils. The first being inside and the second being outside of the TF coils. In the first case, the effect of the coil on a plasma is stronger, due to the closer proximity, than in the second case. The result is that the engineering parameters of the first option can be lower to achieve a comparable effect. The cost of the first option is an increase of required engineering parameters of TF coils. The reason is the cross section of TF coils needs to be enlarged to give space to PF coils and support structure. One possitive effect is a more homogeneous toriodal field, because of the increased distance of the TF coils to plasma.

Design of the coil geometry for COMPASS-U went through several steps in order to meet the engineering (and budget) constraints described in the previous paragraph. At first, the PF coils were supposed to be placed outside the TF coils (as it is shown in blue in Fig. 4.7a). Its advantage is that it is easier to construct and placing TF coils closer to plasma leads to a lower energy consumption. However, placing the PF coils outside the TF coils leads to higher currents for PF coils, worse parameters of the required fast reaction of the PF coils and a lower homogeneity of the toroidal magnetic field (toroidal ripple). Fiesta simulations have shown that placing the PF coils outside the TF coils required unacceptably high currents, especially in top and bottom PF3 coils as it was shown in collaboration with co-authors of the contribution [78]. These results contributed to the decision to put the PF coils inside of the TF coils. Moreover, the CS coils were enlarged in order to deal with required high currents and resulting excessive ohmic power.

coil name	**current range**	**turns**	**total current limit**
CS	± 50 kA	30	1.5 MAt
PF1	± 25 kA	64	1.6 MAt
PF2	± 25 kA	32	0.8 MAt
PF3	± 25 kA	36	0.9 MAt
PF4	± 25 kA	40	1.0 MAt

Table 4.4: PF Coils of the COMPASS-U tokamak and their current limits.

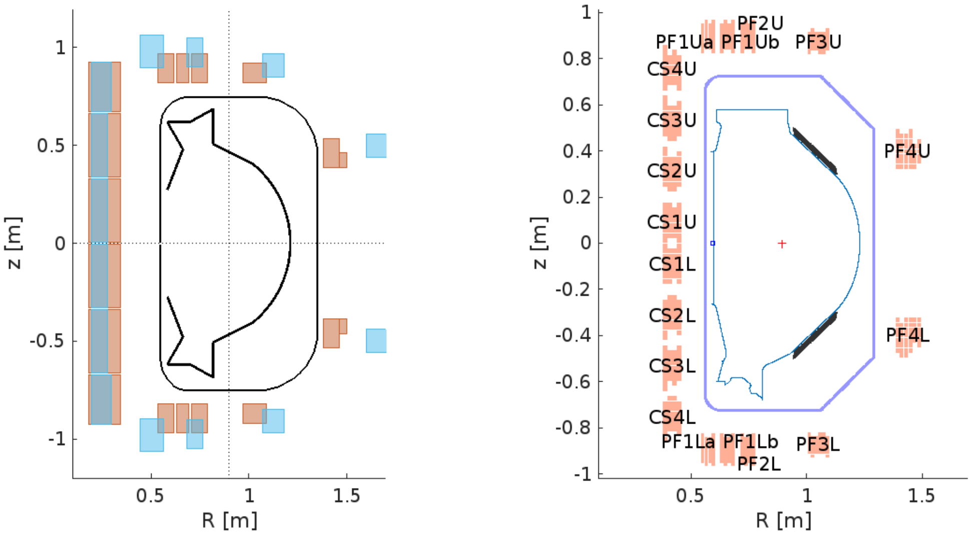

(a)

(b)

Figure 4.7: Initial design of the coil geometry with the PF coils placed outside of the TF coils (blue) and later geometry (orange) with the PF coils inside the TF coils (a) and latest design (b). Black blocks represent stabilising plates used to calculate stability parameter for plasma scenarios. The coil geometry on the left in orange was applied in simulations related to coil geometry optimisation shown in Fig. 4.9a and 4.8 whereas the coil geometry shown on the right was used in the rest of the chapter.

Shift of PF3U and PF3L coils

One of the optimisation parameters, in the design process of COMPASS-U coils, was the radial position of the PF3 coil. The machine design allowed it to be moved by up to 6 cm to LFS. Simulation of MHD equilibria for several scenarios shows that the outward shift of the PF3L and PF3U coils is beneficial. The effect is summarised in the Fig. 4.8. The current in the most stressed coils (PF2L and PF3U) is decreased and it causes a slight current increase in the PF2U. In the case of the baseline scenario with the maximal plasma current, the coil currents changed from 19 kA to 18.5 kA for PF2L and 7.8 to 8.5 kA for PF2U. Changes of the current in other (more distant) coils are negligible.

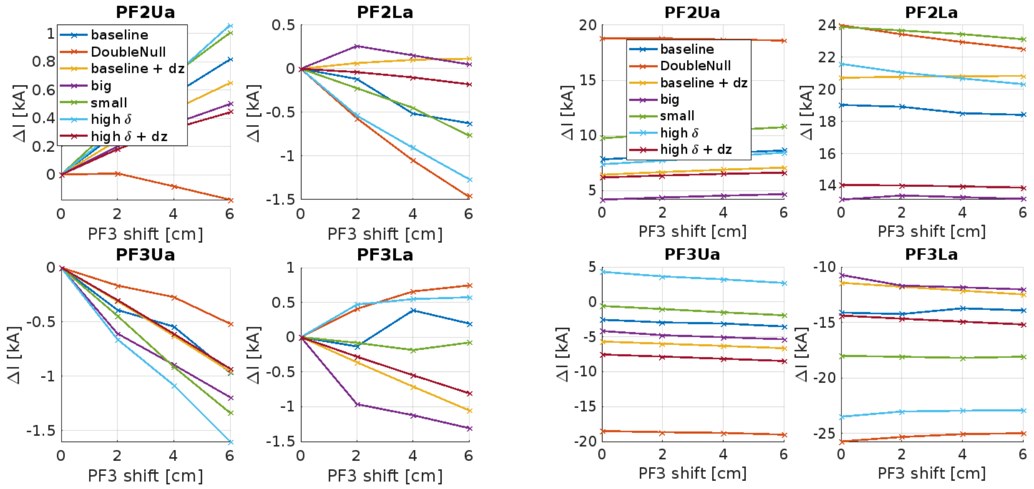

(a)

(b)

Figure 4.8: Requested currents (a) and their change (b) in the coils for different radial positions of the PF3 coil and various plasma configurations: baseline, double null, baseline shifted upwards, big plasma, small plasma, high triangularity and high triangularity shifted upwards (baseline, double null and high triangularity scenarios are described in the next section 4.3.5). The initial geometry is shown in orange in Fig. 4.7a.

Divertor coils

Flexibility of the divertor legs was investigated for different geometries of the divertor coils PF1La, PF1Lb and PFLa: separated coils, PF1La and PF1Lb connected, PF1Lb and PFLa connected, PF1La and PF1Lb connected and PF2La shifted by 2 cm towards LFS and PF1Lb and PF2La connected and shifted by 2 cm towards LFS, see Fig. 4.9a. All these cases allowed a similar range of the strike point positions (about 15 degree range of the HFS leg) under current limits as it is shown in Fig. 4.9. However, the cases with PF1Lb connected to PF1La shows a slightly (by about 3°) broader range of strike point angles for allowed current limits than the geometry with PF1Lb connected to PF2La. Moreover, simulations suggest that configuration with separated divertor coils does not offer higher flexibility of strike point positions and one power source can be spared.

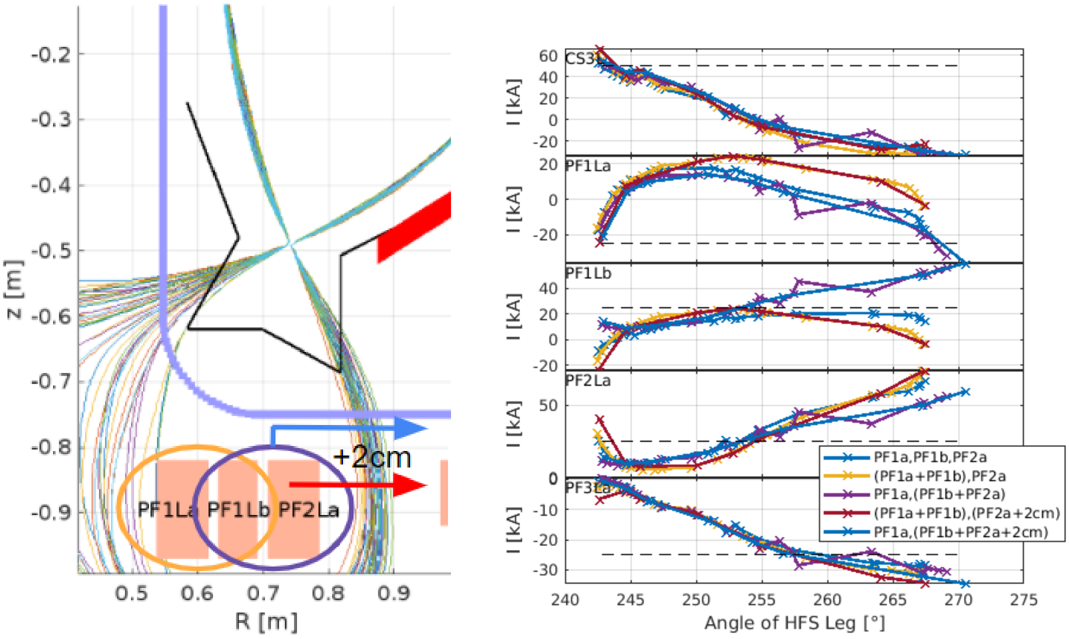

(a) (b)

Figure 4.9: LCFS of the baseline scenario for different strike-point positions with marked configurations (cinnections and shifts) of coils (a) and respective demands on the most affected coils for different coil geometries with corresponding colours (b).

Paired coils in central solenoid

In order to reduce a number of expensive power sources, the possibility to connect the CS coils into pairs shown in Fig. 4.10a was investigated. As it is shown in Fig. 4.10b, the baseline scenario for the paired CS coils with maximal plasma current is still below limits for coil currents although the difference is about 10 kA in CS2U, CS3U, CS4U. The resulting difference in plasma shape was negligible (see Fig. 4.10a).

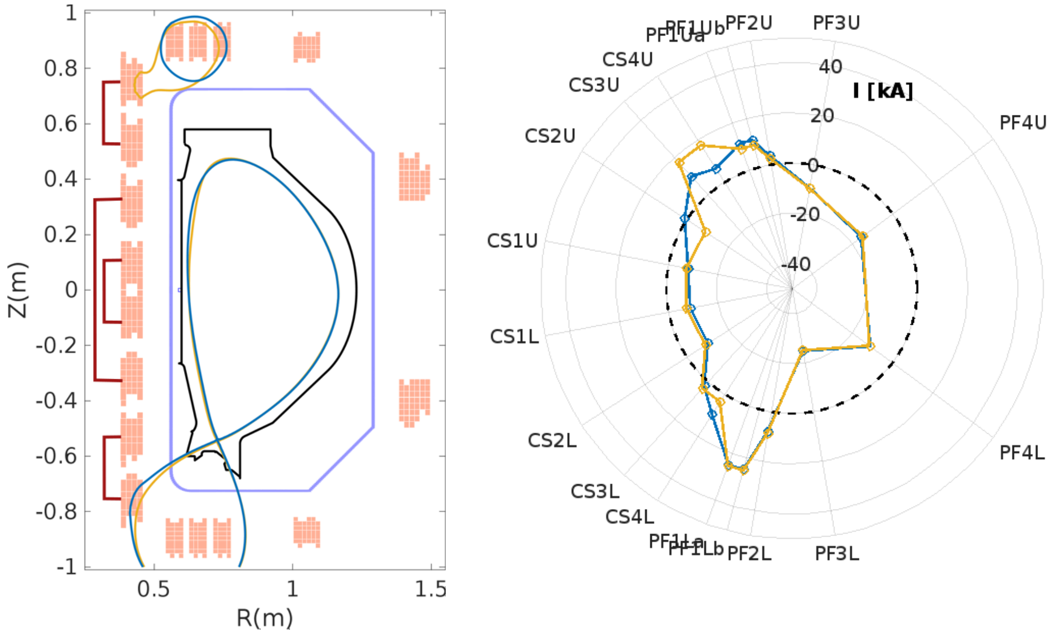

(a)

(b)

Figure 4.10: Coil geometry and connection of the paired CS coils illustrated by red connections (a) and polar plot of the coil currents (b) for the case with the paired CS coils (orange lines) and the single CS coils (blue lines).

4.3.5 Plasma scenarios

Simulations of various MHD equilibria were performed in order to test flexibility and capability of the PF coils and to provide data for calculations of mechanical and heat stresses, theoretical modelling and feedback algorithms. Simulated scenarios span plasma currents ranging from 0.4 MA to 2 MA, toroidal field from 1.25 T to 5 T with pulse duration up to 4 s. The plasma shapes cover triangularities 0, 0.33, 0.5 and 0.6 and elongation 0, 1.4 and 1.8. Simulations are performed according to the setting shown in Fig. 4.11, i.e. with paired coils in the central solenoid. Scenarios consist of three typical phases: ramp-up phase during which the plasma current is driven (mostly by the CS coils) towards the required value, steady state with the constant plasma current and ramp-down phase with a gradual decrease of plasma current. In the ramp-up phase, plasma starts from a circular shape limited by the HFS wall and it is shaped towards the required shape.

The standard scenario (also referred to as #24300) with I_p = 1.4 MA, B_T = 4.4 T, ITER-like shape (triangularity 0.44, elongation 1.8), T_e = 2.5 keV and auxiliary heating (3 MW by NBI and 1 MW by ECRH) is shown in Fig. 4.11 together with a time evolution of its main parameters and currents in the CS coils and the PF coils. The figure illustrates typical features of the COMPASS-U scenarios, especially a dominant range of the CS coil currents consumed during the ramp-up phase (it could be reduced by additional heating) and a high current in the divertor coil PF1L during D-shaped plasma configurations.

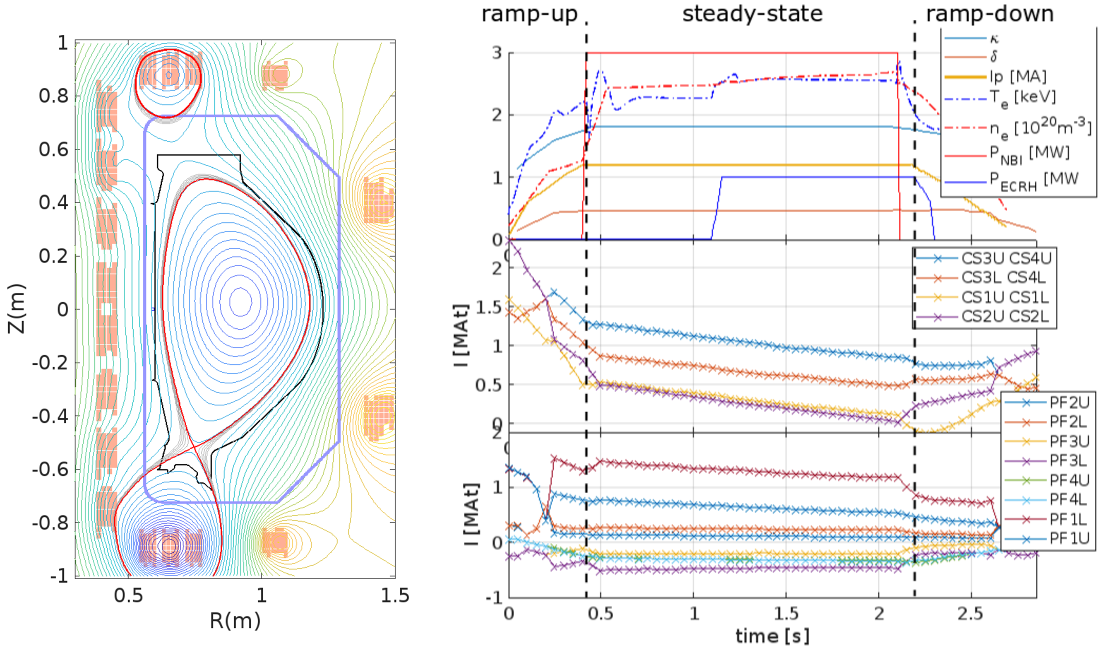

(a) (b)

Figure 4.11: Simulated equilibrium at 1.5 s (a) and time evolution of the main parameters, the CS coils and the PF coils for the standard scenario (#24300).

Equilibria of the selected scenarios with a high triangularity (0.6), double null configuration and snowflake are shown in Fig. 4.12 and their main parameters in Tab. 4.5. These scenarios are topic of interest in fusion research due to the following reasons. Plasma with high triangularity leads to improved pedestal pressure (due to the stabilisation of ballooning modes by moving plasma to HFS) [79, 80, 81]. Double null configuration offers splitting of the heat flux into two divertor regions and it is also observed to offer better fuelling efficiency and overall confinement [82, 83]. On the other hand, it requires precise control of PF coils as a small disbalance can direct most of the heat flux towards upper or lower divertor [83]. Snowflake configuration was proposed in [84, 85] and it was shown to reduce local heat loads to divertor plates [86, 87, 88]. Disadvantage is higher demands on PF coil currents and their precise control. Shown scenarios with maximal plasma current (2 MA) and negative triangularity have $q_{95} < 3$ which implies issues with MHD stability. However, these scenarios are suitable for mechanical and heat analysis to provide a conservative tokamak design. All these scenarios have $f_s > 1.5$ implying vertical stability.

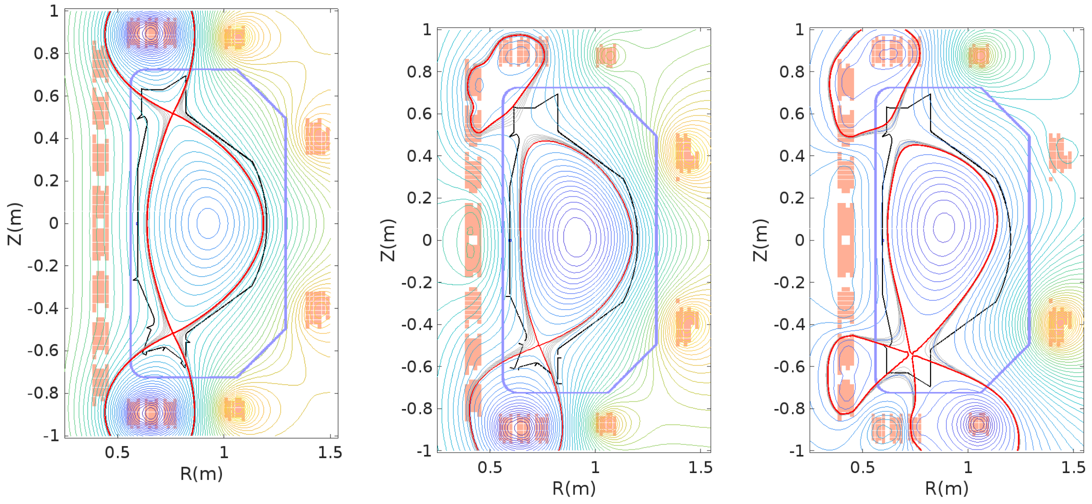

(a) (b) (c)

Figure 4.12: Equilibria (contours of ψ) for the double null (a), high triangularity (b) and snowflake (c) configurations indicating their envelopes (also published in [69]). Red lines represent contour of ψ at separatrix.

Scenario	Max. baseline (1.5s)	Baseline (1.5s)	High δ (1.5s)	Double null (1.5s)	Snowflake (1s)	Negative δ (1.5s)
I_P [MA]	2.0	1.2	2.0	1.2	1.5	1.0
B_T [T]	5.0	4.3	5.25	4.24	5.4	5.1
κ [-]	1.8	1.8	1.8	1.85	1.84	1.4
δ_{upper} [-]	0.4	0.39	0.56	0.53	0.46	-0.24
δ_{lower} [-]	0.55	0.53	0.60	0.53	0.46	-0.28
q_{95} [-]	2.64	3.88	2.54	3.72	3.3	2.65
β_N [%]	1.2	1.2	0.6	1.3	1.0	1.6
T_{e0} [keV]	4.5	3.0	3.5	3.3	3.1	3.3
n_{e0} [$10^{20}/m^3$]	2.3	2.5	2.3	2.5	2.3	2.3
f_s [-]	2.3	2.6	2.0	2.6	2.0	1.86

Table 4.5: Main plasma parameters of selected scenarios. Equilibrium of the baseline (ITER-like) scenario is shown in Fig 4.11, High delta, double null and snowflake in Fig. 4.12 and negative triangularity in Fig. 4.13.

Negative triangularity

Experiments in the DIII-D tokamak indicated that plasma with negative triangularity can reach the confinement similar to H-mode despite the absence of an edge pressure pedestal [89, 90, 91, 92] which leads to a favourable regime without ELM (or with small edge activity). Furthermore, a low impurity retention compared to H-mode plasmas with a similar energy confinement was observed.

In the case of COMPASS-U, negative triangularity $\delta > -0.3$ (compared to -0.4 at DIII-D) for plasma currents up to 1 MA is achievable in Fiesta simulations (under coil current limits from the Tab. 4.4). Higher negative triangularity would require to change the geometry of plasma facing components. The most stressed coil is the PF3 coil taking the role of the divertor coils PF1 and PF2. Higher negative triangularity is also difficult to achieve because of the gap in the coil distribution on the LFS. An additional coil carrying the current 300 kA between PF4u and PF4L could decrease upper negative triangularity by -0.2 and lower negative triangularity by -0.1 as it is shown in Fig. 4.14.

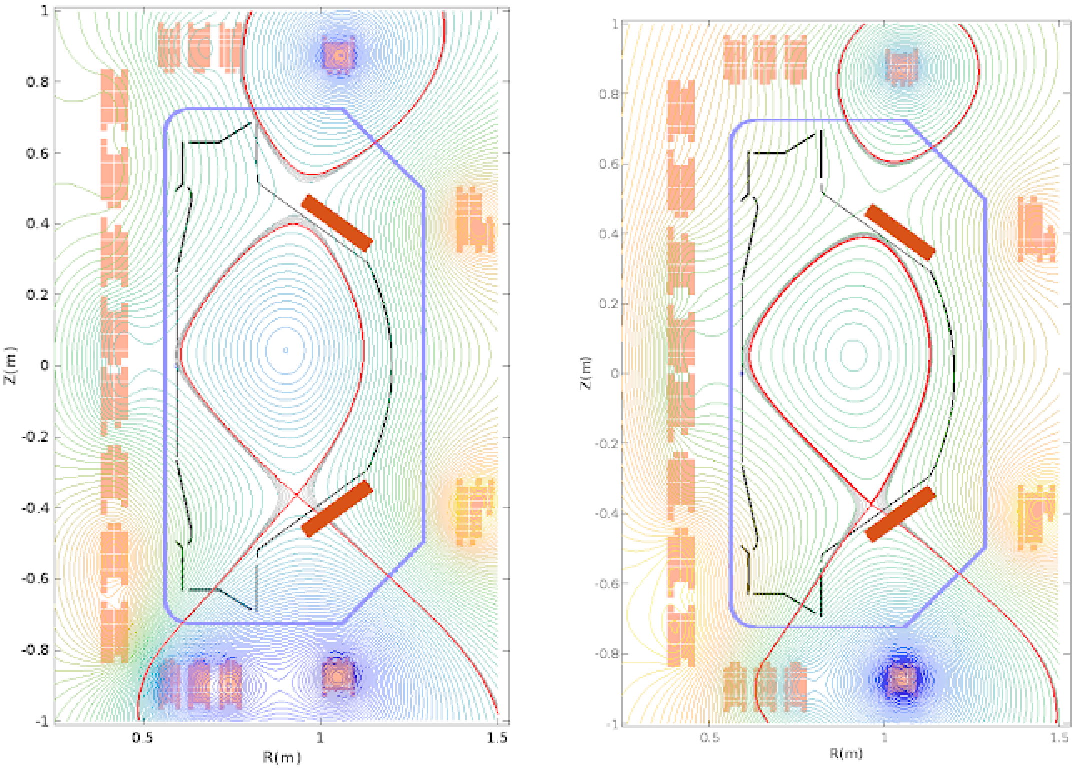

(a)

(b)

Figure 4.13: Equilibria (contours of ψ) with negative triangularity for (a) $I_\mathrm{p} = 500\,\mathrm{kA}, a = 0.27\,\mathrm{m}, \kappa = 1.46, \delta_\mathrm{upper} = -0.27, \delta_\mathrm{lower} = -0.35$ and (b) $I_\mathrm{p} = 1\,\mathrm{MA}, a = 0.27, \kappa = 1.47, \delta_\mathrm{upper} = -0.24, \delta_\mathrm{lower} = -0.28$. Red line represents separatrix.

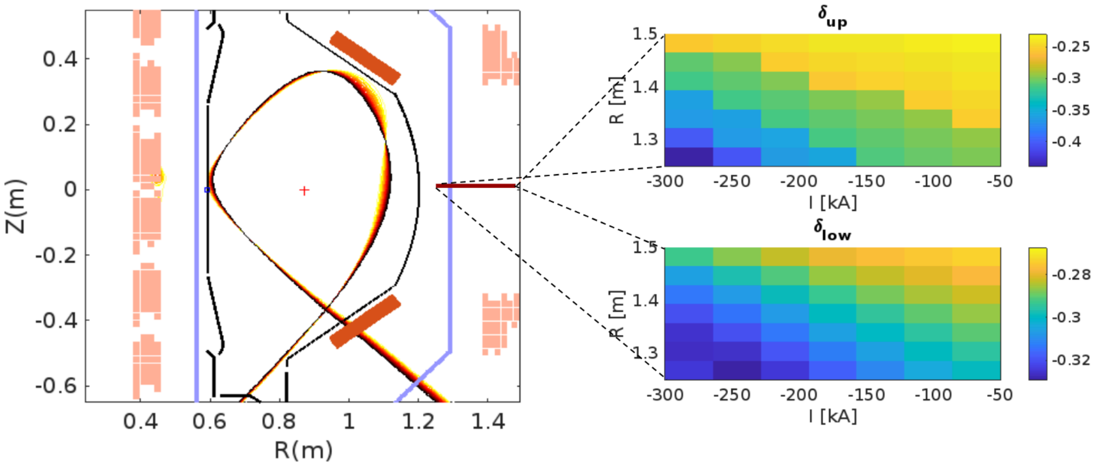

Figure 4.14: Scan over radial positions of the additional coil and its current showing plasma shapes, i.e. separatrix (a) and achieved negative triangularity (b) for the scenario with $I_P = 1$ MA (other main parameters of the scenario are show in Tab. 4.5).

Sweeping strike points

The COMPASS-U tokamak is focused on DEMO-relevant conditions with high heat fluxes to the divertor plates which can reach about 90 MW/m^2 according to the internal report [93]. It is based on scalings from [94, 95], power fluxes from METIS simulations and magnetic equilibria simulated by Fiesta. One of the methods how to reduce the effect of high heat fluxes is a periodical changing, i.e. sweeping of strike point position (e.g. simulations for DEMO in [96] have shown that 20 cm/1 Hz sweeping, with an incident heat flux of 15 MW/m^2 avoided reaching the critical heat flux (boiling) of the coolant in the cooling pipes).

Simulations of the strike points sweeping by Fiesta for COMPASS-U is shown in Fig. 4.15 and 4.16 for frequency 7 Hz and amplitude 3.3 cm. Such sweeping could reduce the heat fluxes towards acceptable values (less than 20 MW/m^2). Simulated sweeping of the strike points requires periodic changes in the coil currents (as shown in 4.15a) which are achievable by the designed power sources as it is shown in Tab. 4.6 where times to reach amplitudes of required current changes are sufficiently small. Faster strike point sweeping could be required e.g. during ELMs. However, frequency of the strike point sweeping is also limited by the vessel self-frequency (9 Hz according to [97]) and it requires placing the coils inside the tokamak vessel and closer to plasma [97].

	R [Ω]	**L [mH]**	**U_{PS} [V]**	**ΔI [A]**	**t_{reach} [ms]**
CS1U+CS1L	1.63	2.10	1000	3,6	8
CS2U+CS2L	1.63	2.10	1000	14	30
CS3U+CS4U	1.63	2.10	1000	6	13
CS3L+CS4L	1.63	2.10	1000	9	19
PF1U	4.54	7.20	660	3	33
PF1L	4.54	7.20	1000	2.2	16
PF2U	2.76	2.65	660	0	-
PF2L	2.76	2.65	660	5,7	23.5
PF3U	4.84	5.27	660	4,7	38.5
PF3L	4.84	5.27	1000	4	21.5
PF4U	6.62	9.59	1000	2	19.5
PF4L	6.62	9.59	1000	0	-

Table 4.6: Main parameters of the coils and times required to reach currents ($\mathbf{t_{reach}}$) to move the strike points by 3.3 cm along the divertor plates for the baseline with $\mathbf{I_P}$ = 2 MA. Required times are derived from the formula: $I = V_b/R\left(1 - e^{-tR/L}\right)$. Values of resistance R, inductance L and voltage of the power sources $\mathbf{U_{PS}}$ for coils correspond to the geometry shown in Fig. 4.7a represented by orange rectangles.

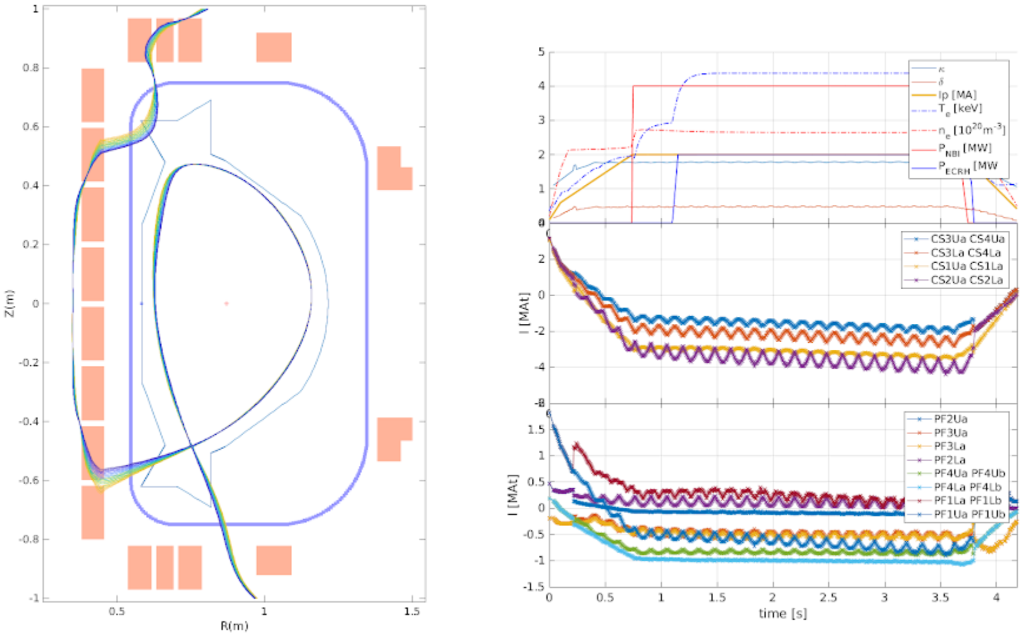

(a) (b)

Figure 4.15: Plasma boundaries (a) and evolution of the coil currents and main plasma parameters (b) for the scenario with sweeping strike points.

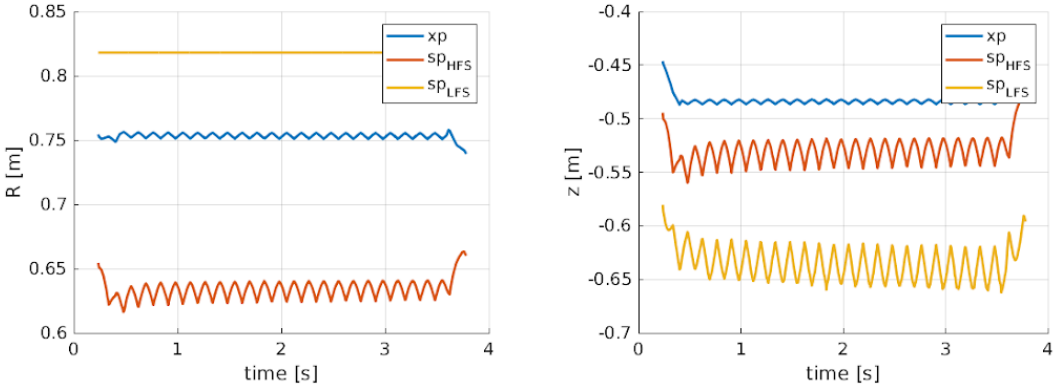

(a) (b)

Figure 4.16: Radial (a) and vertical (b) movement of the strike points and X-point.

4.4 Summary

The chapter overviews the tests of the MHD equilibria reconstruction by the Fiesta code at COMPASS and its application to preliminary equilibria for the COMPASS-U tokamak contributing to its design.

Application of the Fiesta code as a predictive solver finding equilibria for given currents in the PF coils of the COMPASS tokamak is described in the section 4.2, especially for simulations of equilibria during experiments with increased triangularity. Despite differencies between Fiesta and EFIT++ algorithms, the reconstructions of equilibria by Fiesta were shown to be in a good agreement with EFIT++ (e.g. difference in location of separatrix up to 1 cm in upper and lower HFS regions and difference of 0.04 in upper triangularity). Although the proper comparison of both the algorithms would require a more detailed analysis, the tests of Fiesta at COMPASS demonstrated its usability.

The section 4.3 was focused on simulations of equilibria for COMPASS-U associated with the design process of the PF coils. Design of COMPASS-U started with the PF coils placed outside the TF coils since it is easier to construct and it leads to a lower energy consumption. However, Fiesta simulations carried out in the collaboration with co-authors of the contribution [78] have shown that such geometry leads to an unacceptably high current demand in the PF coils which contributed to the decision to put the PF coils inside of the TF coils. Moreover, the CS coils required high currents resulting in excessive ohmic power which led to their enlargement. Furthermore, the section 4.3.4 deals with several cases of a possible optimisation of the coil geometry: connection of the CS coils to pairs to reduce the number of expensive power sources, shifting of the PF3 coil and connection of the divertor coils. Simulations have shown that connection of coils into pairs could still allow to reach MHD equilibria for the baseline scenario with maximal current (2 MA), shifting the PF3 coil towards LFS could lower the current in one of the most stressed divertor coil PF2L and the connection of PF1a and PF1b does not decrease flexibility of strike points.

The last section 4.3.5 shows reconstructed equilibria for the selected plasma scenarios planned at COMPASS-U. It covers the ITER-like scenario, the baseline scenario with maximal plasma current 2 MA, double null configuration, snowflake configuration, negative triangularity and the scenario with sweeping strike points. All the scenarios meet the condition for vertical stability $f_s > 1.5$ presented in section 4.3.3. Scenarios with maximal plasma current 2 MA have $q_{95} < 3$ which implies susceptibility to MHD instabilities. Simulations with negative triangularity $\delta < -0.3$ were achieved for plasma current up to 1 MA although $q_{95} < 3$ implies that lower plasma currents could be more suitable to achieve the MHD stability. The scenario with a slow sweeping of the strike points (7 Hz with amplitude 3.3 over divertor surface) by means of the PF coils could be achieved as required changes in their currents are achievable. However, proper calculation requires to include a model of the vacuum vessel and other passive structures.

5. Tomographic reconstruction of electromagnetic emission and its post-processing

This chapter introduces tomographic reconstruction as a valuable tool for studying instabilities and other plasma processes. The main method used for tomographic reconstructions is described in the introductory section. Following sections provide tomographic reconstructions and their analysis for chosen processes at the COMPASS and JET tokamaks

5.1 Introduction

Tomography allows reconstruction of a local property (e.g. electromagnetic emission) from line integrated measurements in a non-destructive way. The tomography problem can be set as finding an inversion to the following equation (in 2D):

$$f_i = \int g(\mathbf{r}) T_i(\mathbf{r}) \mathrm{d}\mathbf{r} \tag{5.1}$$

where f_i are the line integrated measurements, $g(\mathbf{r})$ the reconstructed property and $T_i(\mathbf{r})$ the geometric function (kernel of the integral representing a contribution of $g(\mathbf{r})$ to the measurement f_i). There are many different tomographic methods. They can be divided into two basic groups: analytical (or transform) methods and numerical (or series expansion) methods. Analytical methods, like the filtered back-projection method [98, 99], are more suitable for situations, where the object can be scanned by many measurements with a regular coverage (however, there are also transform methods reducing problems with an irregular coverage [100]) and they are often used e.g. in medical tomography. Series expansion methods are usually more flexible and more suitable for plasma devices. They find approximated[1] solution as an expansion of g into a suitable set of basis functions b_j with expansion coefficients g_j:

$$g(\mathbf{r}) \approx \sum_j^N g_j b_j(\mathbf{r}). \tag{5.2}$$

transforming the tomography problem into the matrix inversion:

$$f_i = \sum_j T_{ij} g_j = \mathbf{Tg} \tag{5.3}$$

where $T_{ij} = \int T_i(\mathbf{r}) b_j(\mathbf{r}) \mathrm{d}\mathbf{r}$ are elements of the transform matrix. Basis functions can be global (e.g. circular harmonics and Zernike polynomials), natural (in a shape of the area measured by a detector) or local like rectangular shaped pixels which are the most common basis functions and also the ones used in this thesis. Since the inversion is typically an ill-posed (solution is not unique) and

---

[1] A solution could be described precisely only for infinite number of basis functions, but truncation to finite number N makes it approximated.

ill-conditioned (a small change of input results in a big change of output) problem, regularisation methods are often applied to find a unique solution. Conditioning of the problem can be improved by implementation of appropriate regularisation functional introducing a priori information (e.g. expected smoothness of $\mathbf{g}$). Then, the solution can be found e.g. by the Tikhonov regularisation [71], [72], [74], i.e. by minimisation of:

$$\Lambda(\mathbf{g}) = \|\mathbf{f} - \mathbf{T}\mathbf{g}\|_2^2 + \lambda O(\mathbf{g}) \tag{5.4}$$

where λ is the regularisation parameter and $O(\mathbf{g})$ is the regularization functional which can take the form $O(\mathbf{g}) = \|\mathbf{\Gamma}\mathbf{g}\|_2^2 = \mathbf{g}^T\mathbf{H}\mathbf{g}$ where $\mathbf{\Gamma}$ is the Tikhonov matrix and $\mathbf{H} = \mathbf{\Gamma}^T\mathbf{\Gamma}$ symmetric and positive semi-definite operator. Minimisation of 5.4, i.e. $\partial\Lambda(\mathbf{g})/\partial\mathbf{g} = 0$ leads to:

$$\mathbf{g} = \left(\mathbf{T}^T\mathbf{T} + \lambda\mathbf{H}\right)^{-1}\mathbf{T}^T\mathbf{f} \tag{5.5}$$

Basically, the regularisation functional improves conditioning of the problem by increasing eigenvalues of the matrix of inversion [43] and guides the inversion to prefer smooth and physically meaningful solution from an infinite number of possibilities. Essentially, regularisation reduces over-fitting by introducing sanctions of complexity. In order to compensate a noise, the first term in the formula 5.4 can be normalised by expected error bars σ_i into the form of the Pearson χ^2 test [101]:

$$\chi^2 = \frac{1}{L}\sum_i^L\left(\frac{f_i - \sum_j T_{ij}g_j}{\sigma_i}\right)^2 \tag{5.6}$$

representing goodness of fit with the optimal value close to 1 (typically $\chi^2 - 1 = \pm 0.05$ is accepted). The lower values indicates over-fitting while higher values indicates under-fitting. The tomography inversion is carried out by both minimization of 5.4 and optimisation of χ^2 by finding optimal λ (e.g. by the Newton method).

Taking into account geometry of diagnostics, where the view of a detector is given by a cone through a pinhole and $\mathbf{g}$ as isotropic emissivity, the integrated property f_i (also referred as a chord brightness [101]) can be expressed as:

$$f_i \approx P_i \frac{4\pi}{A_i\Omega_i} \tag{5.7}$$

where P_i is a power flux (W/m^2) measured by a detector, A_i its effective area (perpendicular to its line of sight) and Ω_i solid angle observed by the detector.

In experimental fusion devices, where tomographic algorithms have to deal with sparse, often irregular and noisy measurements, the Tikhonov regularisation constrained by regularisation functional in the form of the Fisher information is often applied as it was proven to provide robust and reliable solutions [101], [102], [103]. The Fisher information is defined as:

$$I_\mathrm{F} = \int (\nabla g)^2/g \cdot dS \tag{5.8}$$

which leads to its numerical form:

$$I_\mathrm{F} = \mathbf{g}^T\mathbf{B}^T\mathbf{W}\mathbf{B}\mathbf{g} = \mathbf{g}^\mathbf{T}\mathbf{H}\mathbf{g} \tag{5.9}$$

where the matrix $\mathbf{B}$ is an operator for derivatives of $\mathbf{g}$ and $\mathbf{W}$ is a weight matrix representing $1/\mathbf{g}$. Since $\mathbf{W}$ depends on $\mathbf{g}$, the solution has to be found iteratively. The method is also often referred as Minimum Fisher Regularisation (MFR) [104]. In statistics, the Fisher information is a way to measure amount of information that a variable carries about parameters that define its distribution, i.e. its minimization leads to a simple and smooth solution, in particular in regions with low additional information and less data (acting like Occam's razor principle). In order to improve performance of the MFR, derivatives of $\mathbf{g}$ are carried out in direction perpendicular and parallel to the reconstructed magnetic field with different weights so that the solution with higher smoothness along magnetic field lines is preferred (in accordance with physical expectation). The MFR is described in more detail in the attached article A.3 with several implemented optimisations like adjustments of border conditions (for SXR and AXUV tomography at COMPASS) or symmetrisation of the Fisher information.

Faster versions of the MFR

Non-linearity of the Fisher information requires an iterative approach in its evaluation (otherwise, the solution could use iterations just to find optimal λ) and demands more computational time. The computational time depends mainly on the number of pixels, e.g. the MFR algorithm used in this thesis takes hundreds of ms for several thousands of pixels and grows roughly linearly with their number (growth of the computational time is not so rapid due to the sparse matrix calculation). However, several modifications of the algorithm were proposed allowing a faster inversion, which are suitable for mass data processing. As an example it can serve the Fast MFR allowing calculation of more time slices at once [105] or, for the real-time application suitable, the rolling iteration that uses the previous result as a starting point for the iteration [106]. Application of the rolling iteration on model data is described in the attached article A.2 and applied at COMPASS in the chapter 5.2.3.

Linear methods

The linear methods present another way how to reduce computational time. They are based on matrix decomposition techniques like SVD [107], generalised eigen values (GEV) [108] or QR decomposition [109] aiming at finding the inversion with the linearised regularisation functional (Tikhonov matrix), e.g. in the form of smoothness of the solution and the regularisation parameter λ as median of eigenvalues. Besides fast and direct solution ($\mathbf{g}$), these linear methods also allow fast calculation of the distribution moments like centre of mass, variance and skewness as a scalar multiplication of measured signals and basis vectors in tens of microseconds and without necessity to calculate a solution. Calculation of basis vectors can take tens of milliseconds, but they can be precalculated as they depend on the geometry of the problem, see flowchart in Fig. 5.1. Moments of the radiation distribution provides information about plasma radiation in a compressed form which is more suitable for purposes of the real-time control or mass data processing.

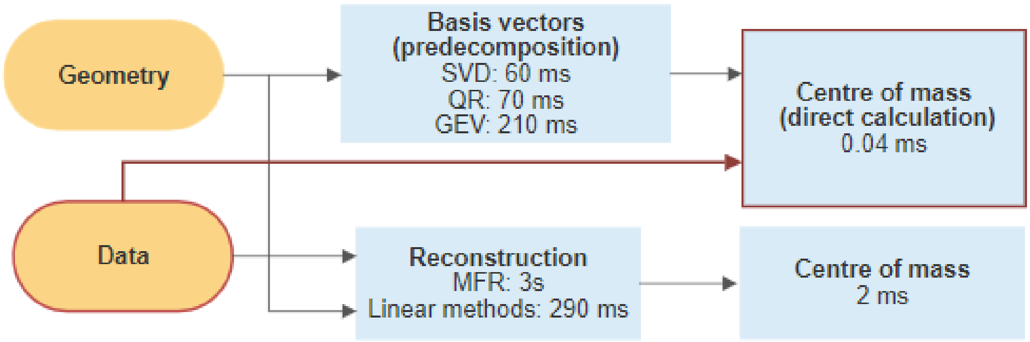

Figure 5.1: Flowchart of calculation of "centre of mass" of the radiation distribution with their computational times. Direct calculation of the "centre of mass" from data (without tomographic reconstruction) is stressed by the red colour. Computational times are only illustrative as they depend mostly on the resolution and CPU (in this case performed for 6300 pixels at Intel Core i7-3630QM).

Disadvantage of the linear methods is a lower precision and robustness than in the case of the MFR. Moreover, magnetic field lines can not be included into fast calculations of the radiation moments as they change in time that requires recalculation of the basis vectors.

The linear methods used in this thesis apply the regularisation functional in the form of smoothness of the solution, i.e. $F(g) = \|\mathbf{C}g\|^2$ where $\mathbf{C}$ is the numerical differentiation matrix. By adopting decomposition $\mathbf{TC}^{-1} = \mathbf{U\Sigma V}^T$, the solution 5.5 can be (after several steps) transformed into the form [107]:

$$g(\alpha) = \sum_j w_j(\alpha) \frac{\mathbf{f} \cdot \mathbf{u_j}}{\sigma_j} C^{-1} v_j \tag{5.10}$$

where u_j and v_j are columns of $\mathbf{U}$ and $\mathbf{V}$, σ_j diagonal elements of the singular values $\mathbf{\Sigma}$, and $w_j(\alpha) = (1 + \alpha/\sigma_i^2)^{-1}$ acts as a low-pass filter suppressing components with higher j as σ_j decreases. This allows to express the radiation centre ("centre of mass") as a scalar combination of the measured signals and basis vectors:

$$\mu_x = \frac{\sum_{k,l} x_k g_{kl}}{\sum_{k,l} g_{k,l}} = \frac{\mathbf{f} \cdot \mathbf{b_x}}{\mathbf{f} \cdot \mathbf{b_0}} \tag{5.11}$$

where the basis vectors are:

$$b_{xj} = w_j(\alpha) \frac{(\mathbf{u}_j)}{\sigma_j} \sum_{k,l} x_k v_j^{k,l} \tag{5.12}$$

$$b_{0j} = w_j(\alpha) \frac{(\mathbf{u}_j)}{\sigma_j} \sum_{k,l} v_j^{k,l} \tag{5.13}$$

Higher distribution moments can be calculated in a similar way. Fast estimation of the optimal value of regularisation factor α can be chosen as median of singular values (med($\mathbf{\Sigma}$)).

Application of the linear methods to SXR data at COMPASS and a comparison with the MFR are described in the attached article and chapter 5.2.2.

5.2 Tomographic reconstructions at COMPASS

In the following sections of this chapter, tomography and its analysis is carried out for SXR and AXUV measurements at COMPASS introduced in the chapter 5.2.1. SXR emissivity is generated mainly by bremsstrahlung and line radiation of heavy impurities. At COMPASS, it is often observed to be poloidally symmetric and localised in the plasma core with monotonic increase towards the plasma centre (as can be seen in Fig. 5.2a). Tomographic reconstructions based on of AXUV measurements often exhibit hollow profiles for diverted (D-shaped) plasmas as it is shown in Fig. 5.2b caused by line radiation of not fully ionised impurities near the plasma edge. Circular (limited) plasmas radiate strongly near limiter with strong plasma-wall interaction [104]. Corresponding intensity is about one order of magnitude higher than radiation measured by the SXR detectors. In several cases, tomography seems to have a tendency to underestimate radiation in divertor region and a bit overestimate radiation inside the confined plasma along detectors observing the divertor (i.e. reconstructing radiation from the divertor inside the confined plasma) due to a sparse coverage. In order to compensate these artefacts, the AXUV-C camera (see Fig. 5.3a) was slightly tilted lower towards the divertor (after discharge #14885).

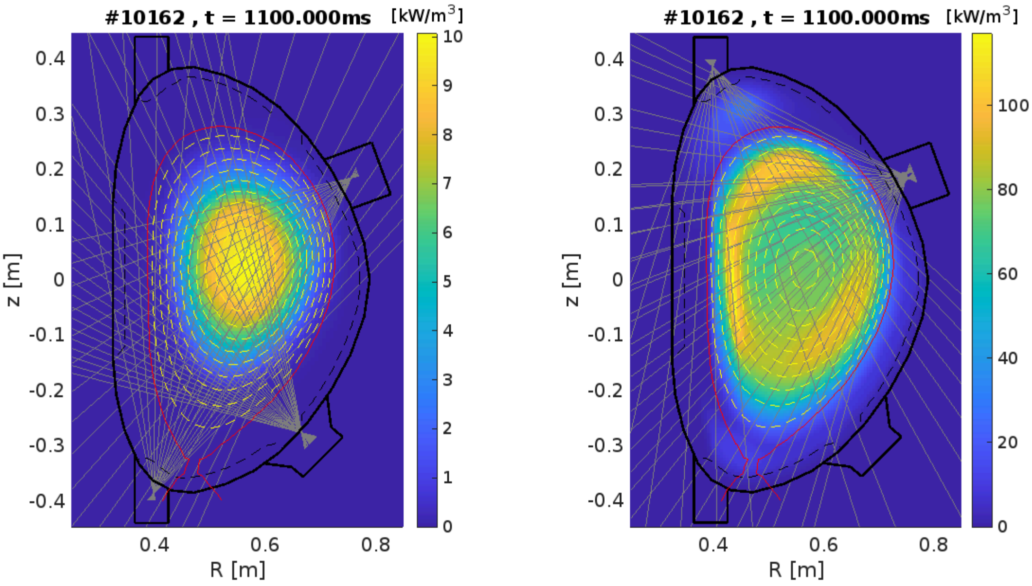

(a) (b)

Figure 5.2: Example of emissivities reconstructed from the measurements of the SXR (a) and AXUV (b) detectors. The red contour represents separatrix whereas the dashed yellow lines the magnetic field lines inside the confined plasma. In this case, the AXUV reconstruction in the divertor region is underestimated due to a sparse coverage.

5.2.1 Multi-array diagnostics of electromagnetic emission at COMPASS

The tokamak plasma is a volume radiator of electromagnetic emission ranging from visible to SXR spectra (with negligible absorption). Assuming a strong toroidal symmetry (along the torus), complexity of the problem can be simplified into the 2D poloidal cross-section of the tokamak plasma. Typically, a pinhole camera concept, i.e. the array of detectors looking through pinhole, is used, and measured signals represent integrated radiation from the whole solid angle of the detection. In order to provide local radiation, the tomographic algorithm (introduced in section 5.1) has to be applied.

At COMPASS, measurement of electromagnetic emission is focused on observations of fast radiating events connected to plasma instabilities and impurity transport. These measurements require a high temporal resolution, hence, photodiodes providing time scales in the range of microseconds are used. The photodiodes are used in two ways described in more detail in the next sections: without a filter as a sort of fast ”bolometers” (AXUV detectors) or with a beryllium filter as SXR detectors.

AXUV detectors

Absolute extreme ultraviolet AXUV photodiodes are often used in tokamaks [110, 111, 112, 113] for a fast measurement of electromagnetic emission (in the order of μs) as they are vacuum compatible [114] and they can sustain temperatures up to 200 °C (with the operational temperature below 80 °C).

At COMPASS, six arrays of 20 silicon photodiodes each (of type AXUV20ELM or AXUV20ELG made by International Radiation Detectors, Inc. which was later acquainted by Opto Diode Corporation) cover one whole poloidal cross-section of the tokamak vessel as it is shown in Fig. 5.3a. The lower limit of detected photon energies is given by the band gap energy (the lowest energy to overcome the forbidden gap between the valence and conduction bands where an electron can participate in conductor) for silicon which is 1.12 eV whereas the upper limit is due to thickness of the diode active layer (30-40 μm [111]) about 6 keV. Responsivity of the photodiodes, i.e. current produced per incident power, is rather close to its theoretical limit given by the ionization energy of silicon 3.65 eV (i.e. energy required to completely remove an electron from the ion to infinity) as $1/3.65 = 0.275$ A/W and roughly constant for photon energies above 200 eV as can be seen in Fig. 5.3b. The drop of sensitivity in the UV region is caused by a layer of SiO_2 acting as an anti-reflection and passivation layer providing protection from the effects of the surrounding environment like oxidation. Extremely small thickness of the passivation layer in the case of AXUV20ELM or AXUV20ELG (3-7 nm of SiO_2 [114]) keeps the absorption of photons in the passivation layer at minimal values. Nevertheless, lower spectral sensitivity in UV region makes application of the AXUV photodiodes as calibrated bolometers problematic. The advantage of AXUV photodiodes is the low response time about 200 ns which allows measurement up to fraction of μs. Basic parameters of the photodiode are summarised in the table 5.1.

Active area (single diode)	0.75 mm x 4.05 mm
Distance between diodes	0.2 mm
Response time	200 ns
Operational temperature	-20 °C to 80°C in vacuum or nitrogen -10°C to 40°C in atmosphere (to avoid oxidation)
Baking in vacuum	up to 200°C
Range of photon energies	1.1 eV to 6 keV

Table 5.1: Basic parameters of the AXUV20ELG photodiode array.

The photodiodes are connected in a conducting direction (with the positive voltage offset 0.3 V on its anode) as a source of current which is amplified and converted into voltage (with transimpedance gain $4.5 \cdot 10^5$V/A) as the COMPASS data acquisition system requires. Signals are sampled with frequency 2 MHz while the amplifier suppress frequencies above 300 kHz in order to avoid aliasing and to deal with a noise. The temporal resolution of the order of several μs allows observation of radiation during fast events like ELMs, disruptions, MHD, etc.

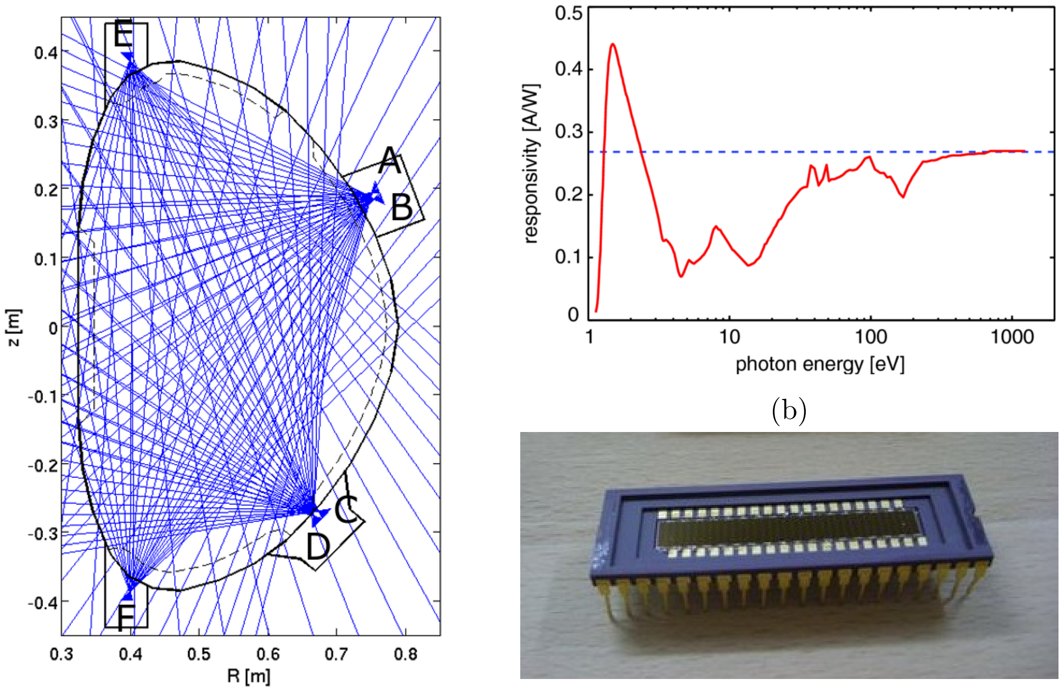

(a)

(b)

(c)

Figure 5.3: Lines of sight of the AXUV photodiodes used as pinhole cameras (a), responsivity with the blue dashed line at 0.27 A/W from manufacturer specifications [115] (b) and the picture of the photodiode array (c).

SXR detectors

The SXR diagnostic system at COMPASS consists of two pinhole cameras placed in the angular ports (see Fig. 5.4a) and one vertical camera from the AXUV system temporally adapted to measure SXR (for pulses #6697-#13213) in order to improve performance of SXR tomography. The two cameras located in the angular ports contains photodiode arrays with 35 detectors (type LD35-5T made by Optronics Inc.) whereas the vertical camera was equipped with the AXUV detector AXUV20ELM due to spatial constraints. The spectral sensitivity (shown in Fig. 5.4b) is given mainly by thickness of the beryllium foil d_{Be} and the diode active layer d_{active} which is about 200 μm thick [116]:

$$f_{\text{det}}(\nu) = \exp\left(-\mu_{Be} d_{Be} - \mu_{Si} d_{\text{dead}} - \mu_{Si_3N_4} d_{Si_3N_4}\right) \cdot \left(1 - \exp\left(-\mu_{Si} d_{\text{active}}\right)\right) \quad (5.14)$$

where μ_{Be}, μ_{Si}, $\mu_{Si_3N_4}$ are absorption coefficients [117] and d_{dead}, $d_{Si_3N_4}$ thicknesses of dead and passivation layers.

Temporal resolution is about 3 μs (constrained by the design of amplifier and data acquisition) which allows investigation of fast MHD processes including internal kink modes (with frequency of about 10-40 kHz) or sawtooth oscillations (below 500 Hz). The spatial resolution of each camera (widths of field of views of individual detectors in the region of main SXR emission) is 1–2 cm.

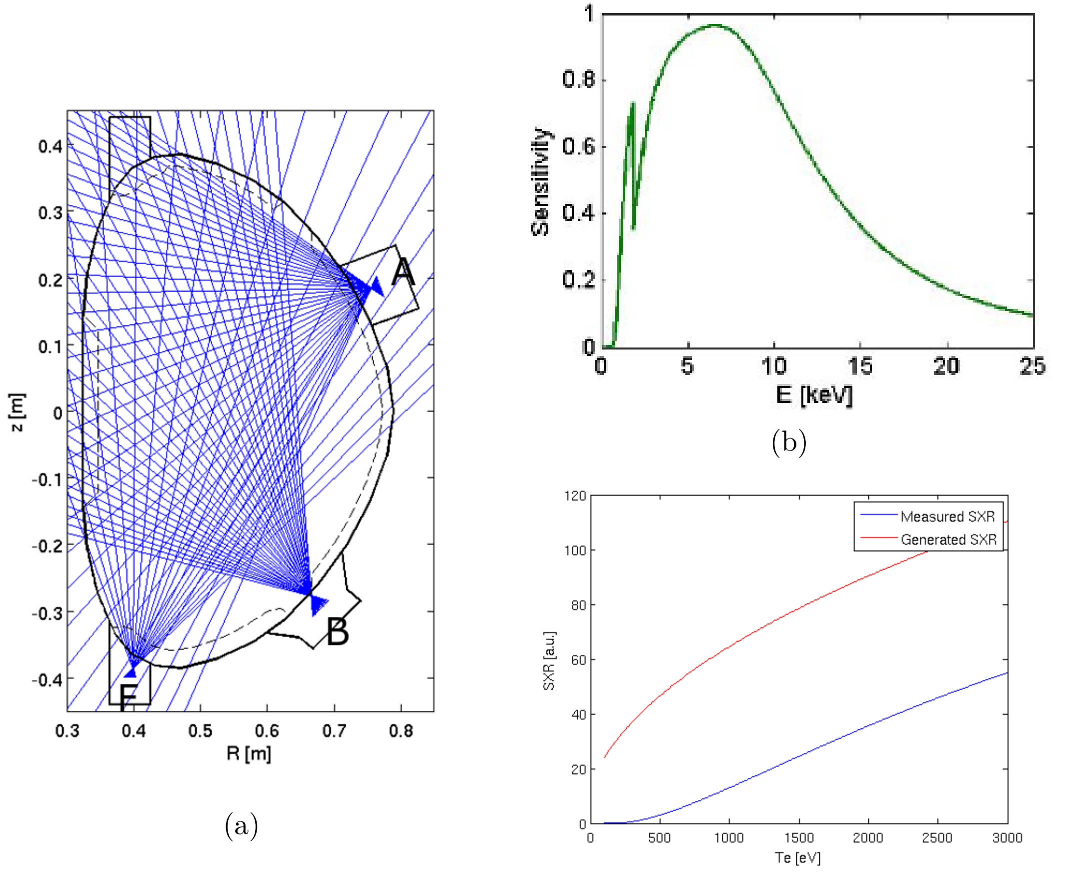

(a)

(b)

(c)

Figure 5.4: Lines of sight of the SXR detectors (a), spectral sensitivity predicted by 5.14 (b) and dependence of generated bremsstrahlung (given by 3.4) and measured SXR on T_e (c).

Active area (single diode)	0.96 mm x 4.6 mm
Distance between diodes	0.03 mm
Operational temperature	-25°C to 75°C
Soldering temperature (max 5 s)	200°C

Table 5.2: Basic parameters of the LD35-5T photodiode array.

Calibration and etendue

Measured signals or the number of the detected photons are proportional to etendue of the detector, i.e. the viewing cone (represented by solid angle Ω) of the detector through the pinhole multiplied by the detecting area (S):

$$G = \int_{\Omega} \int_{S} n^2 \, \mathrm{d}S \cos\theta \mathrm{d}\Omega \tag{5.15}$$

which can be for the pinhole camera set-up rewritten into a more practical form:

$$G = S_{\mathrm{det}} S_{\mathrm{slit}} \cos(\theta)^4 / d^2 \tag{5.16}$$

where d is the perpendicular distance between the slit and the detector, θ is the angle to the normal vector of the detector surface S_{det} and S_{slit} is surface of the pinhole, see Fig. 5.5a. Lines of sights can be found by the spatial calibration as it is illustrated in Fig. 5.5, i.e. by measuring detector response with respect to the position of the light source. The spatial calibration has to be performed after each replacement of the photodiode.

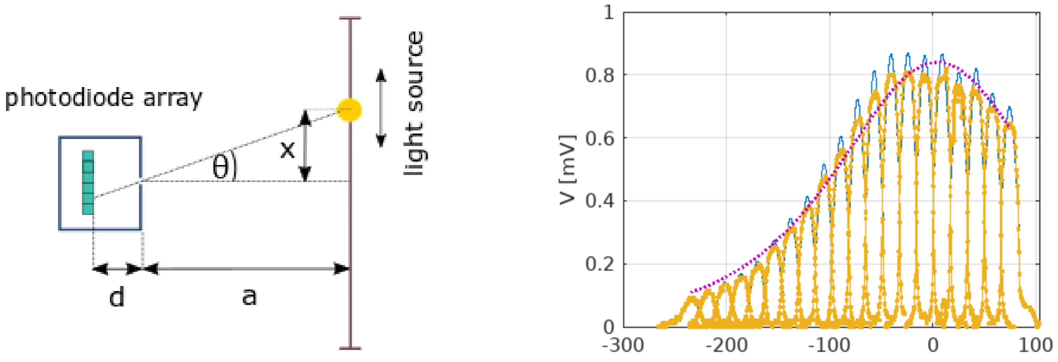

(a)

(b)

Figure 5.5: (a) Spatial calibration scheme and (b) response of individual channels of the photodiode array with respect to the position of the movable light source (orange) together with the Gaussian fit (blue) which was applied to find individual centres of LOS.

The relative response of the AXUV diodes during the relative calibration has shown a very small variation (about 1% as it was shown in [118]). The calibration of the SXR detectors was performed at CEA Cadarache, see Fig. 5.6 showing relative responses of detectors (with difference up to ±10%) with respect to the voltage of SXR source (applied to accelerate electrons producing bremstrahlung radiation).

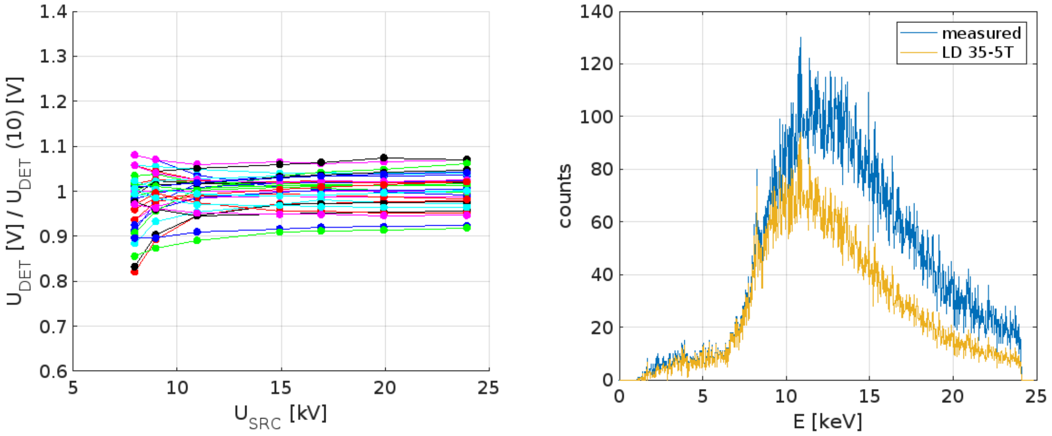

(a) (b)

Figure 5.6: Calibration of the LD35-5T photodiode (measuring SXR) at COMPASS using the SXR source at CEA Cadarache: the relative response of the channels of the LD35-5T photodiode with respect to the voltage of the SXR source and the spectrum of the SXR source under the accelerating voltage 24 kV measured by the Si PIN diode (blue) compared to the spectrum recalculated for photodiode LD35-5T (orange). Drop of energies below 6 keV is caused by 83 cm distance in the air between the detector and the SXR source.

5.2.2 Comparison of the SXR emission distribution with magnetic axis

Reconstruction of the SXR emission and calculation of its radiation centre (its ”center of mass”) can provide supplementary information about the plasma position, in particular when radiation distribution is less affected by asymmetries caused by radiation of impurities, assymetries in auxiliary heating, MHD modes, etc. Its comparison with the magnetic axis of the plasma configuration can also reveal systematic errors in measurements of magnetic field (e.g. caused by drifts of the integrqated signals of the diagnostic magnetic coils [105]). Moreover, the radiation centre and higher moments of the radiation distribution have a potential for the real-time plasma control as they carry information about the plasma behaviour compressed into only few numbers.

At COMPASS, measurements of the SXR radiation are advantageous for comparison with the magnetic axis as its significant part is generated by bremsstrahlung (depending on plasma density and temperature according to the formula 3.4) and thus highly localised in the plasma core; as it is illustrated in Fig. 5.2a. This assumption is acceptable for pure plasmas with low amount of impurities. At COMPASS, SXR can be strongly affected by impuritiy radiation e.g. after impurity puff as it is shown in Fig. 5.23 which also indicates low amount of impurities before the puff. An example of comparison of SXR radiation centre from the MFR with magnetic axis is shown in Fig. 5.7 where both the radial and vertical coordinates of the SXR radiation centre exhibit a systematic shift with respect to the reconstructed magnetic axis but follow the same trend. Besides systematic errors in both diagnostics, the difference in a radial position could be also consequence of plasma shape (in the case of D-shaped plasmas) and of the Grad-

Shafranov shift. These effects could be reduced by comparing centre of mass of SXR radiation with centre of mass of plasma current (current centroid). Comparison of SXR radiation centre with magnetic axis or their trends is practical as magnetic axis is commonly referred to as a plasma parameter and used for real-time plasma control. A lower vertical coordinate of the magnetic axis could be caused by systematic errors of diagnostics. For example, Photron camera indicates that plasma separatrix is higher than the one reconstruced by EFIT in the case shown in Fig. 5.9. AXUV radiation centre is also shown in Fig. 5.7 with a lower radial coordinate than SXR, which is a consequence of the higher radiation near the limiter.

Furthermore, the response of the vertical coordinates of the magnetic axis and the SXR radiation centre to fast vertical kicks (used to affect ELMs) is also shown in Fig. 5.8 illustrating the response of the plasma to faster changes. The vertical coordinate in both the cases reacts in the same way, i.e. with the same trend and systematic difference up to 1 cm.

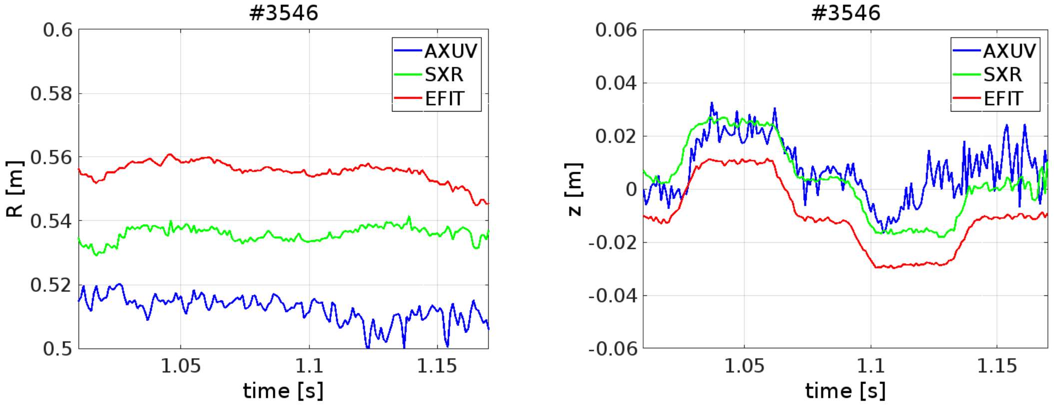

(a) (b)

Figure 5.7: Horizontal (a) and vertical (b) coordinates of the radiation centre from the MFR for the SXR and AXUV measurements and the magnetic axis during the circular pulse with a varying vertical position (published in [119]).

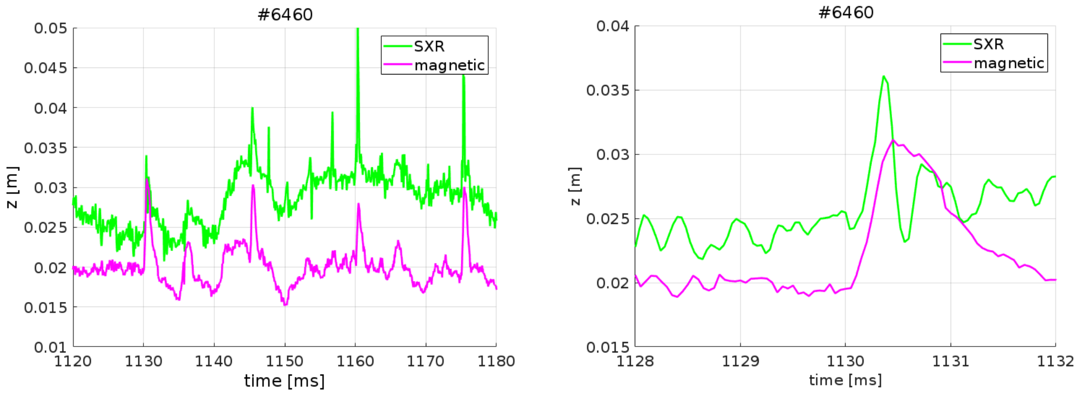

(a) (b)

Figure 5.8: Vertical coordinates of the SXR radiation centre from the MFR and of the magnetic axis during the pulse with vertical kicks at 1130ms, 1145ms, 1160ms and 1175ms (a) with the first kick in detail (b).

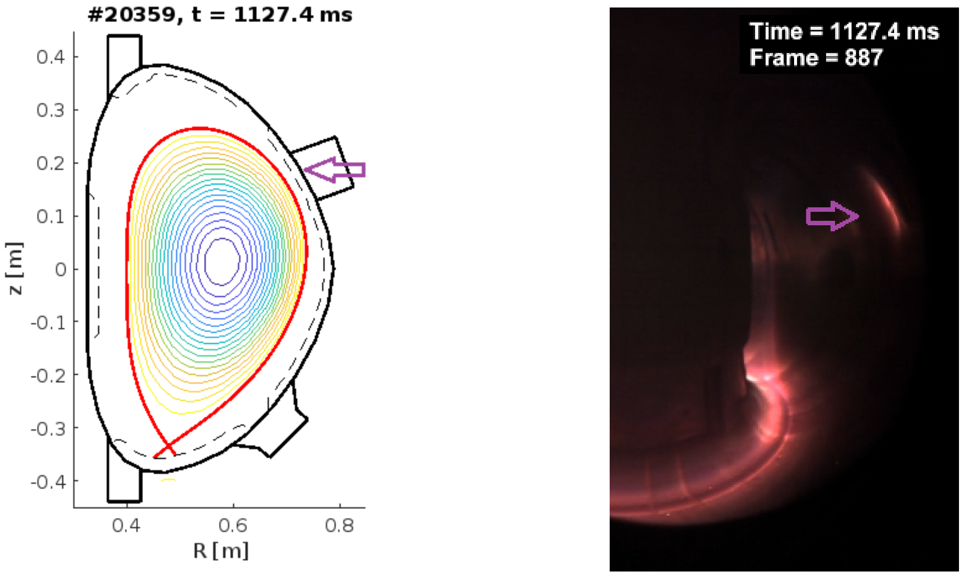

(a) (b)

Figure 5.9: (a) Example of the EFIT equilibrium and (b) view from the Photron camera measuring the visible radiation. The camera indicates a strong plasma-wall interaction (marked by the purple arrow) in the upper part of the vessel whereas EFIT shows the gap of 2 cm between the wall and plasma separatrix.

Performance of linear methods

Linear methods (as described in the chapter 5.1 and in the attached article A.3) allow for a fast tomography and a direct calculation of the distribution moments from a scalar multiplication of data with precalculated basis vectors (given by geometry of the problem) at the expense of a lower precision (compared to the MFR).

In this section, the linear methods based on SVD, QR and GEV decomposition are compared to the MFR algorithm, especially differences of their reconstructed radiation centres from the magnetic axis. All methods search for a smooth solution via isotropic differentiation, i.e. along Cartesian's coordinates instead of anisotropic differentiation allowing to find a smooth solution with respect to the magnetic field lines. This allows fast calculation of the radiation centre as the precalculated basis vectors 5.13, 5.12, shown in Fig. 5.10, remain the same. This leads mainly to higher poloidal asymmetries in SXR reconstructions as it is indicated in Fig. 5.11, but the radiation centre still has a potential to carry a useful information about the plasma position. Comparison of SXR radiation centres calculated by linear methods with EFIT during the discharge #5737, shown in Fig. 5.12 illustrates usual relation of the SXR radiation centre and magnetic axis at COMPASS introduced in the previous section. The SXR radiation centre has typically lower radial position which could be explained by the Shafranov shift and D-shaped plasma configuration. The vertical position of the SXR is typically higher than magnetic axis reconstructed by EFIT. It is also shown in Fig. 5.12 that removing extremes, i.e. lowest and highest values of the reconstructed emissivity from calculation of the radiation centre can reduce a difference between the magnetic axis and the radiation centres. However, this approach can not be used for a direct calculation of the radiation centre from the basis vectors.

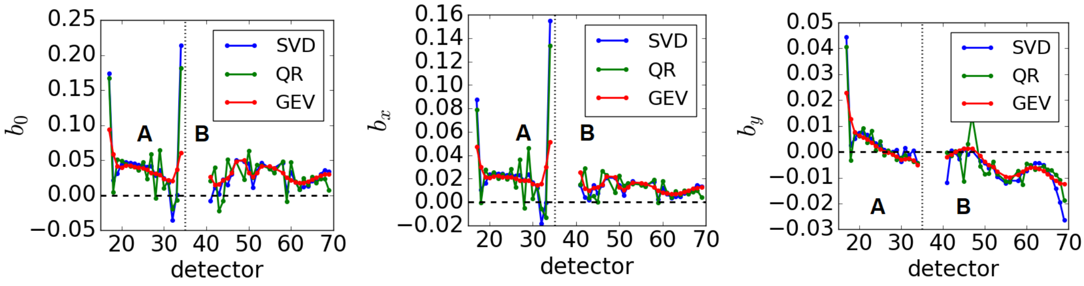

(a) (b) (c)

Figure 5.10: Basis vectors b_0 (a), b_x (b), b_y (c) for calculation of the radiation centre from the SXR detectors at COMPASS by means of the linear methods based on SVD, QR and GEV decomposition. Dotted line separates the detector numbers for the camera A and B.

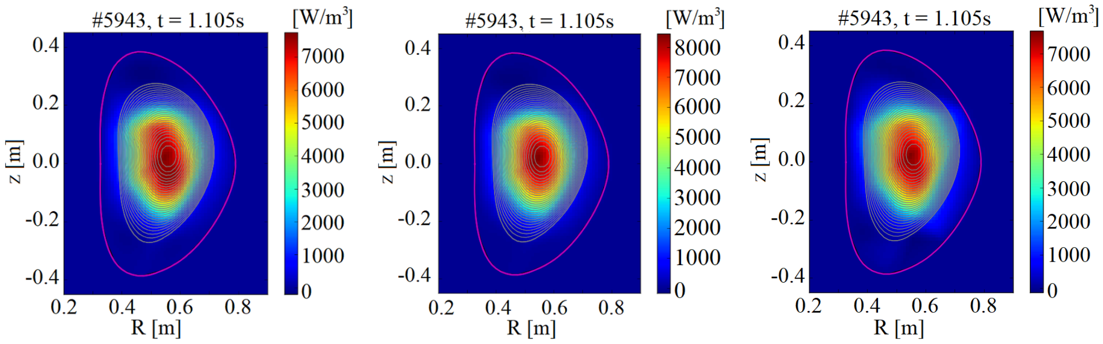

(a) Reconstruction for SVD (b) Reconstruction for QR (c) Reconstruction for GEV

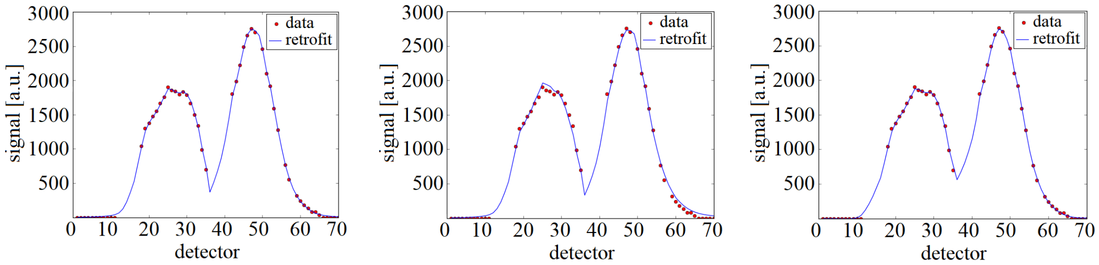

(d) Data and retrofit for SVD (e) Data and retrofit for QR (f) Data and retrofit for GEV

Figure 5.11: Example of SXR reconstruction by means of SVD, QR and GEV decomposition (top) and the measured data with retrofit (bottom).

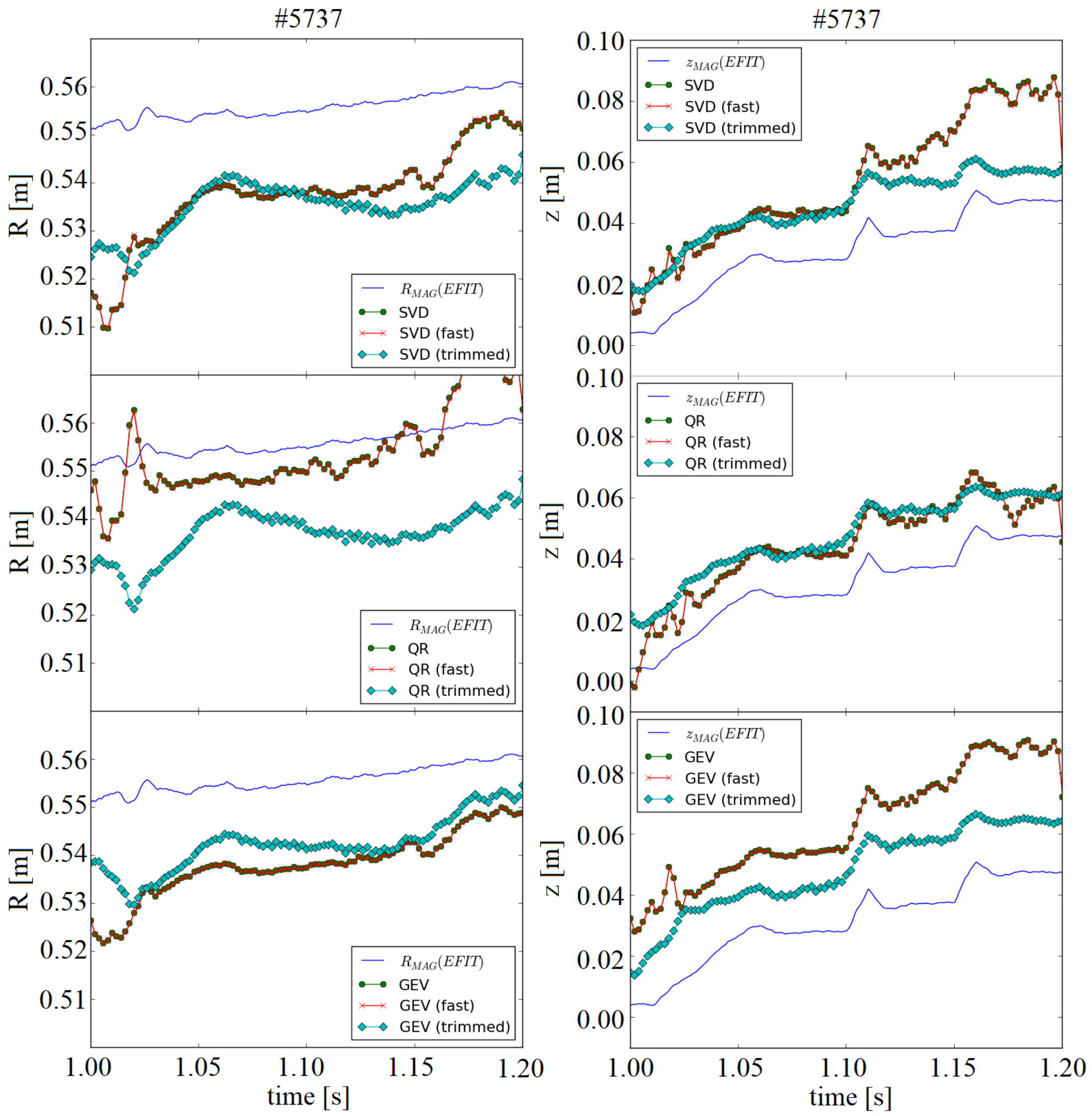

Figure 5.12: Comparison of the SXR radiation centres from different linear methods (SVD, QR and GEV from top to bottom respectively) with the magnetic axis during the D-shaped pulse #5737. The lines labelled as trimmed correspond to calculations including only emissivities ranging from 10% to 90% of the reconstructed maximal value.

Systematic shifts between the SXR radiation centre and the magnetic axis from EFIT shown in Fig. 5.12 are typical for D-shaped COMPASS discharges as it is shown in the histograms in Fig. 5.13 and corresponding table 5.3 covering 90 various discharges (between #5735 and #6173). In these cases, the MFR method exhibits the best stability, i.e. the lowest deviations of the SXR radiation centre from the magnetic axis. Among the linear methods, the method based on GEV decomposition shows results closest to the MFR and with the lowest deviation of SXR radiation centre (1 cm in radial coordinate and 1.3 cm in vertical coordinate). All methods were applied on square pixels with the size of 1 cm.

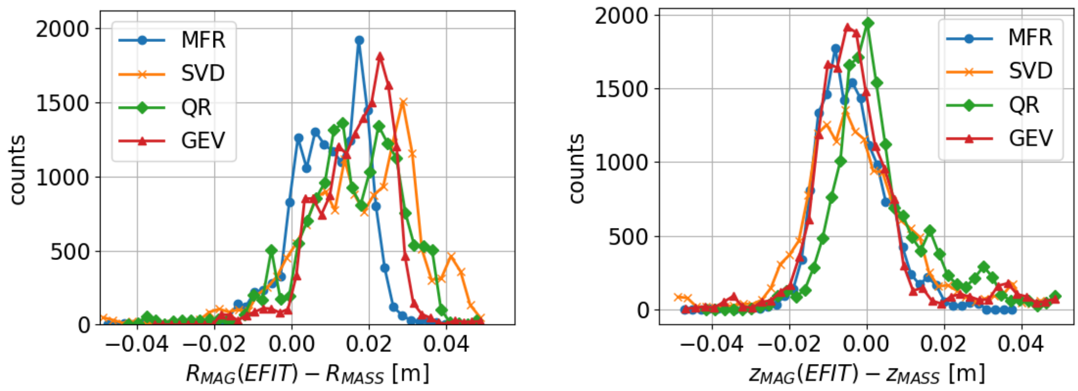

(a) (b)

Figure 5.13: Histograms of radial (left) and vertical (right) differences between the magnetic axis (reconstructed by EFIT) and the centre of mass of the SXR radiation from the linear methods (SVD, QR, GEV) and from MFR. Data were obtained from 90 various discharges (between #5735 and #6173) with a typical D-shaped configuration.

Method	$\mu(\Delta r)$ [m]	$\sigma(\Delta r)$ [m]	$\mu(\Delta z)$ [m]	$\sigma(\Delta z)$ [m]
MFR	0.010	0.009	-0.004	0.009
SVD	0.018	0.015	-0.002	0.014
QR	0.016	0.013	0.004	0.013
GEV	0.016	0.010	-0.002	0.013

Table 5.3: First two moments corresponding to the histograms in Fig. 5.13 showing differences between the magnetic axis (reconstructed by EFIT) and the centre of mass of the SXR radiation. Radial and vertical differences are represented by $\Delta r = R_{MAG}(EFIT) - R_{SXR}$ and by $\Delta z = z_{MAG}(EFIT) - z_{SXR}$ respectively.

5.2.3 Radiation losses measured by AXUV

Total radiation losses represents an important element of tokamak power balance (as mentioned in section 3.3) depending on profiles of the plasma temperature, density and ion species (as described by the formula 3.11) which can be calculated from reconstructed pixel emissivities and pixel dimensions.

At COMPASS, radiation losses measured by AXUV can be described predominantly by averaged plasma density measured by the interferometer and by plasma regime, see Fig. 5.14a and scaling in Fig. 5.15. The dependence of radiation losses on temperature is partly projected into its dependence on density as plasma temperature is related to plasma density (increasing plasma density often leads to a redistribution of the available energy supplied by the plasma heating into more particles and thus the plasma temperature decreases), as it is shown in Fig. 5.14c. There are differences among trends of radiation losses with respect to plasma density and temperature caused by different amount of impurities and different plasma profiles. Accumulation of impurities is highest during ELM-free H-mode as the transport from the plasma core is significantly reduced. During these pulses, plasma density is often uncontrollable and can rise even without any gas puff into tokamak vessel due to an accumulation of particles released from the tokamak wall. ELM-free H-modes often ends with a disruption or H-L transition. The plasma parameters are more ”stable” during ELMy H-mode (when taking into account only inter-ELM parts) as the transport of particles causing ”self-cleaning” of the plasma core significantly rises during ELMs.

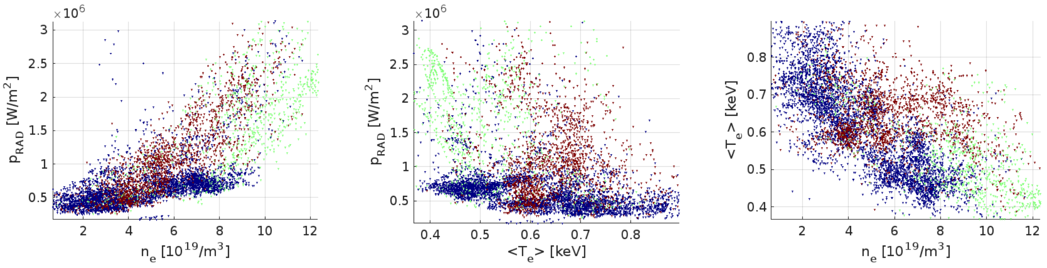

(a) (b) (c)

Figure 5.14: (a) Dependence of the radiation losses seen by AXUVs at COMPASS on averaged density $\langle n_e \rangle$, (b) on averaged electron temperature $\langle T_e \rangle$ and (c) dependence of $\langle T_e \rangle$ on $\langle n_e \rangle$ during L-mode (blue), H-mode (red) and ELM-free H-mode (green). Radiation losses are normalised to plasma cross-section (poloidal area).

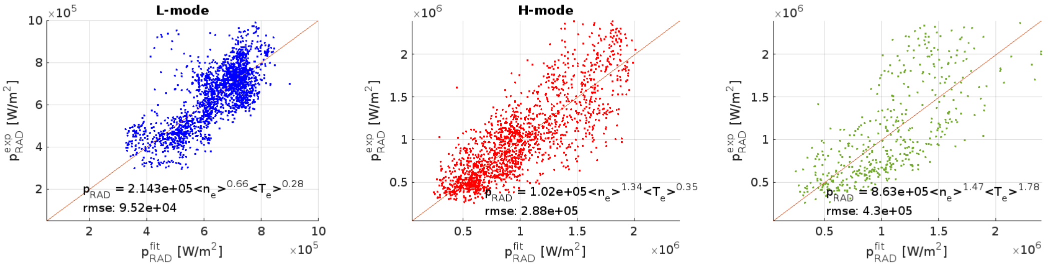

Figure 5.15: (a) Scaling of the radiated power measured by AXUV with $\langle T_e \rangle$ and $\langle n_e \rangle$ during L-mode (blue), (b) ELMy H-mode (red) and (c) ELM-free H-mode (green). Radiation losses are normalised to plasma cross-section.

5.2.4 Radiation during ELMs at COMPASS

ELM is edge localised mode is an instability causing the quasi-periodic relaxation of a pressure gradient at plasma edge leading to expulsion of particles and energy from the confined plasma which increases plasma-wall and radiation, in particular in the divertor region, see section 2.4.3. During ELMs at COMPASS, the radiation losses (seen by the AXUV detectors) can increase by 50% in total and several times in the divertor region due to radiation of released particles from the walls during ELM. The radiation losses during ELMs seen by AXUV grow approximately proportionally to the loss of energy indicated by EFIT, see Fig. 5.17. A possible nonlinear behaviour if observed could indicate a significant influx of impurities from divertor plates during ELMs [120]. The measured radiation losses represent a relatively low fraction of the energy loss seen by EFIT (28% compared to 50% at JET [120]) which could be caused by a sparse coverage of the divertor region and a lower sensitivity of AXUV in the UV region (where the line radiation of light impurities can be typically observed).

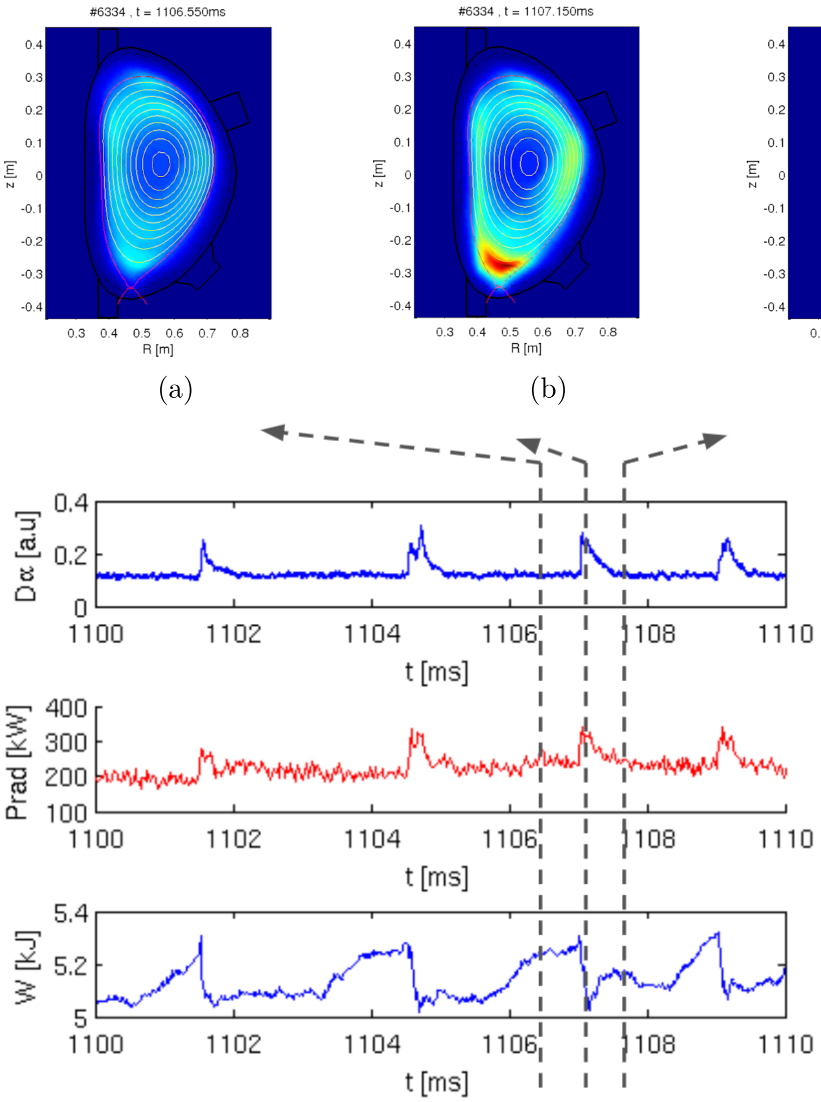

(a) (b) (c)

(d)

Figure 5.16: Tomography reconstruction before (a), during (b) and after (c) ELM and evolution of D_α radiation, radiated power and plasma energy (d).

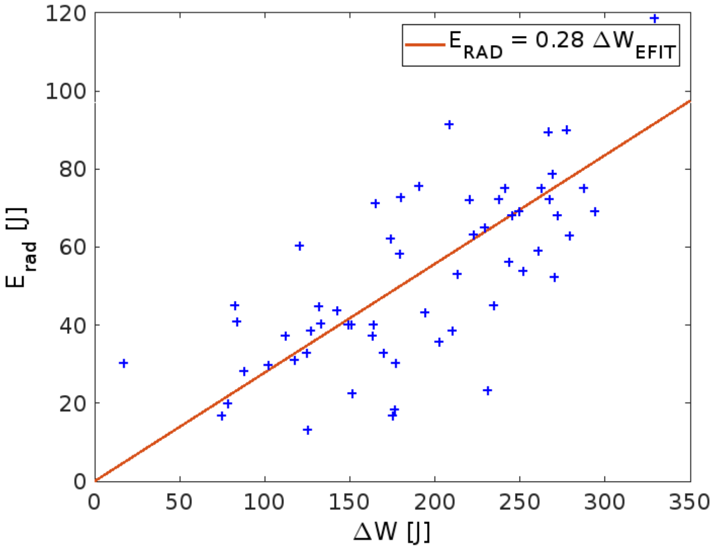

Figure 5.17: Radiated energy seen by AXUVs detectors grow proportionally to the loss of energy indicated by EFIT.

AXUV detectors can observe fast events including propagation of ELM and its filamentary structure. At COMPASS, analysis of ELM filaments by means of AXUV is complicated by background with high noise at higher frequencies but AXUV detectors have potential to be used for observation of filaments as it is demonstrated by Fig. 5.18a showing propagation of filaments with apparent poloidal velocity 1320 m/s moving upwards.

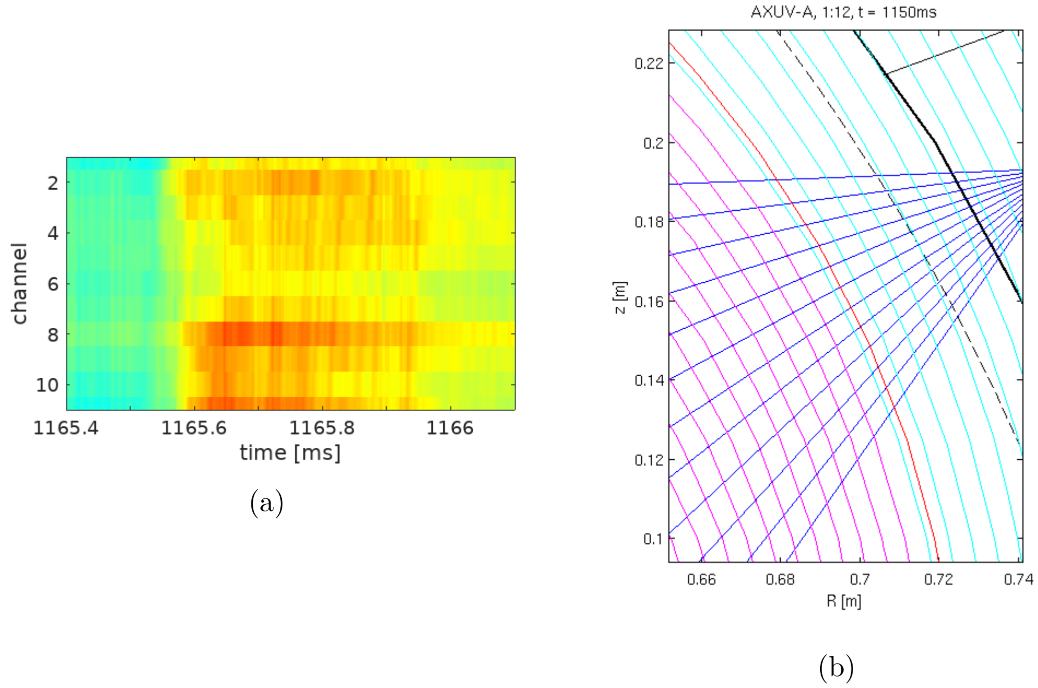

(a)

(b)

Figure 5.18: (a) Intensity of electromagnetic emission measured by AXUV detectors illustrating propagation of ELM filaments as red stripes and (b) lines of sights of used AXUV detectors. Filaments crosses poloidal distance 6.6 cm per 50 μs resulting in apparent poloidal component of velocity 1320 m/s which is in agreement with velocities seen by the fast visible photron camera [121].

5.2.5 Radiation during impurity seeding at COMPASS

The detachment regime allow reduction of the heat flux reaching plasma facing components by cooling of escaped particles via radiation and friction in the cloud of neutrals formed in the divertor region as described in chapter 3.3.1. It can be achieved naturally at higher plasma densities or induced by impurity seeding.

At COMPASS, the open divertor and a relatively short connection length require high plasma densities ($> 10^{20}\mathrm{m}^{-3}$) leading to unstable ELM-free regimes. The detachment regime at lower densities with sustainable ELMy H-mode can be achieved only by means of impurity seeding [122]. Impurity seeding with argon or neon into the divertor region can significantly decrease heat flux reaching the divertor at COMPASS [123, 122]. AXUV tomography during N_2 seeding in Fig. 5.19 shows a rapid increase of the plasma radiation near the X-point after opening the valve with N_2 in divertor region. Simultaneously, the temperature and heat flux measured by the probes start to drop from 50 eV to 5 eV and from 40 kW to 5 kW, respectively. The radiated power in the divertor region increases approximately three times during the N_2 seeding, its maximum moves upwards and seems to be independent on the used N_2 in flow. The decrease of the heat flux reaching the divertor approximately corresponds to the increase of the radiation losses near the divertor region (35 kW) as it is shown in Fig. 5.22. On the other hand, radiation of the confined plasma increases with the N_2 puff as nitrogen penetrates to the plasma core (also visible on comparison of SXR with the temperature and density profiles from Thomson scattering in Fig. 5.23) and it is compensated by the increased ohmic power due to the increased resistivity as shown in Fig. 5.20. This behaviour indicates that there is an optimal value of the N_2 flow rate allowing a significant reduction of the power reaching the divertor while keeping stable impurity radiation losses from the confined plasma and that it lies between $2.0 \cdot 10^{20}$ m^{-3}s^{-1} and $3.7 \cdot 10^{20}$ m^{-3}s^{-1} (for the applied scenario with $\mathrm{I_p} = 210$ kA and $n_e = 4 \cdot 10^{19}$ m^{-3}). Accumulation of impurities in the plasma core is also indicated in Fig. 5.23 as a ratio of the reconstructed SXR profile and pure bremsstrahlung which can be measured by the SXR detectors according to their spectral sensitivity and to the temperature and density profiles from Thomson scattering:

$$f(Z_\mathrm{eff}) = \frac{P_\mathrm{sxr}}{P_\mathrm{brem}(Z_\mathrm{eff}{=}1)} = Z_\mathrm{eff} + P_\mathrm{line}/P_\mathrm{brem} \tag{5.17}$$

where Z_eff is effective charge given by equation 3.3, P_sxr is measured SXR emission, $P_\mathrm{brem}(Z_\mathrm{eff}{=}1) = \Sigma_\nu \epsilon_{\mathrm{brem},\nu} f_\mathrm{det}(\nu) h \Delta\nu$ pure bremsstrahlung seen by the SXR detectors, $\epsilon_{\mathrm{brem},\nu}$ bremsstrahlung emissivity given by 3.2 and $f(\nu)_\mathrm{det}$ detector sensitivity given by 5.14. The ratio 5.17 represent upper limit of effective charge.

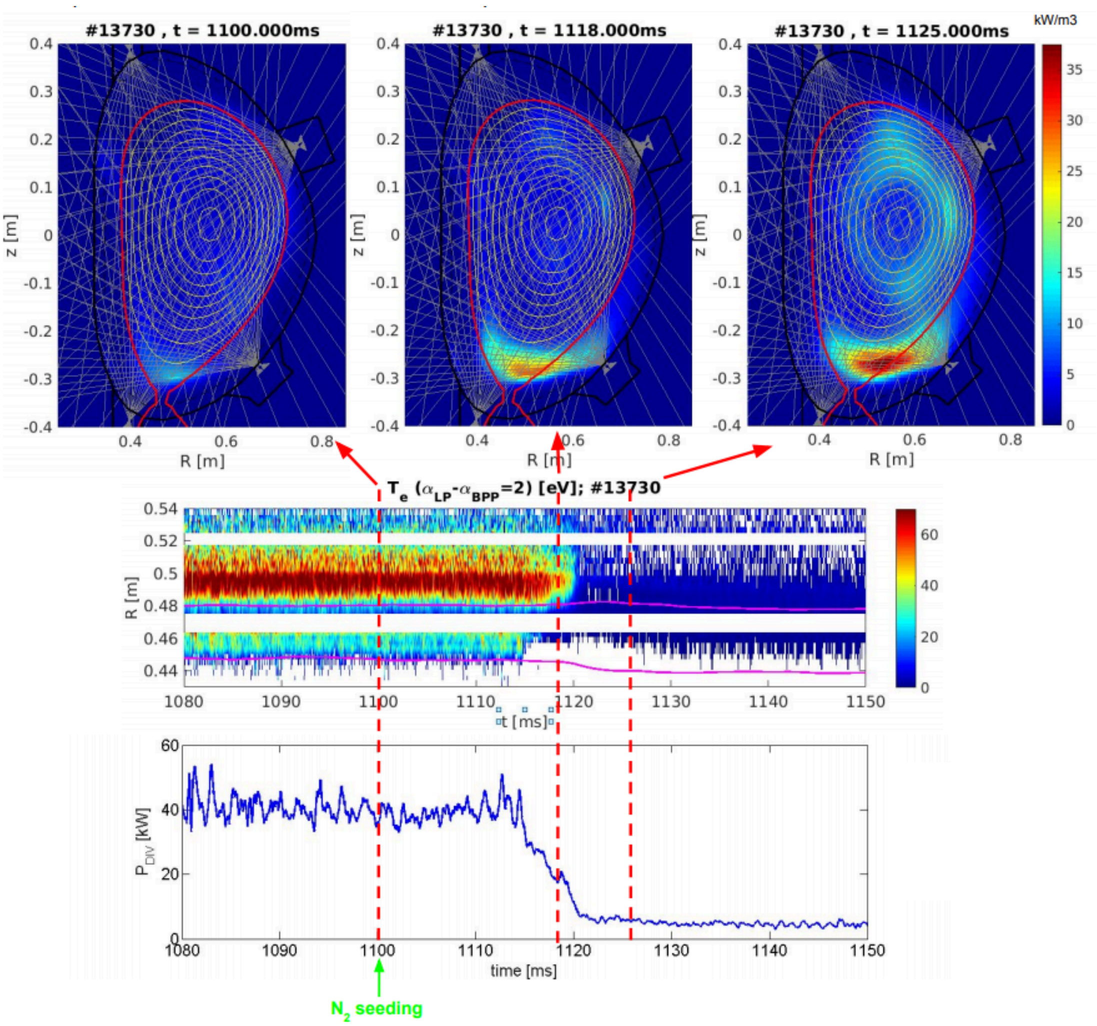

Figure 5.19: Reconstructed radiation measured by AXUV (top), the temperature profile at the divertor measured by the divertor probes (middle) and the total power reaching the probes (bottom) during the experiment with N_2 seeding. AXUV reconstructions are shown at three moments: before N_2 seeding (marked by the green arrow), during formation of a region with an increased radiation near the divertor region accompanied by a decrease of the temperature and total power reaching the divertor (P_{DIV}) and during a phase with the stabilised low power reaching divertor (5 kW) and temperature (below 5 eV).

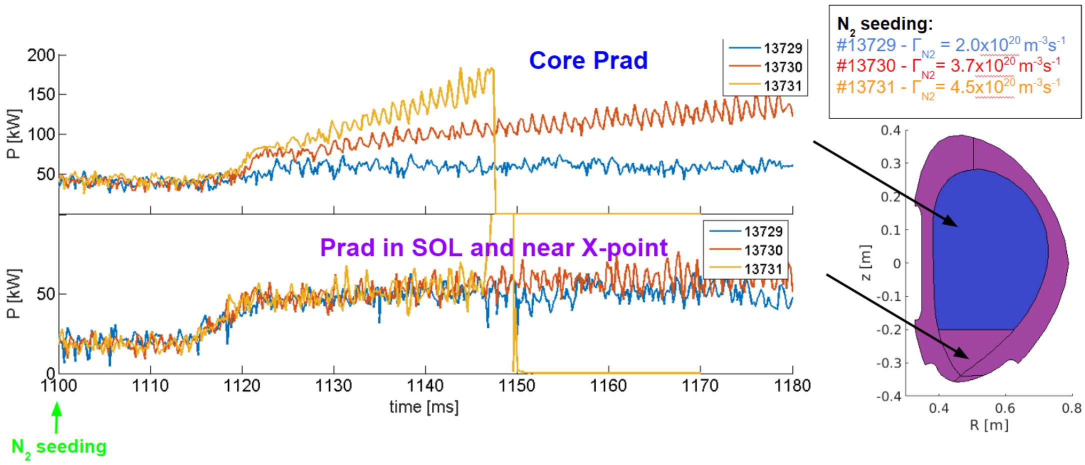

Figure 5.20: Effect of N_2 seeding on radiated power from the plasma core and from SOL and the region near X-point. Top-left plot shows evolution of radiation from the plasma core shown as the blue region in right figure. Bottom-left plot shows radiated power from the magenta region. Legend on top-right shows N_2 flow-rates during the discharges.

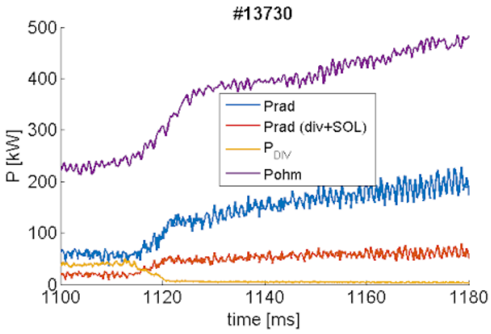

Figure 5.21: Total radiation losses seen by AXUV (Prad), radiation losses near the divertor and in the SOL (Prad (div+SOL)), Power reaching the divertor (Pdiv) and ohmic heating (Pohm).

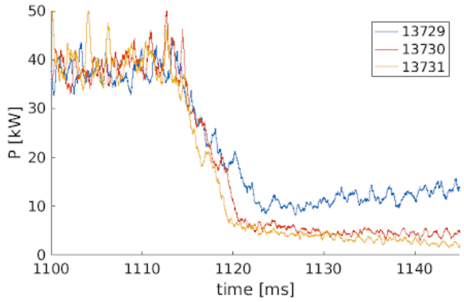

Figure 5.22: Power reaching the divertor during the discharges with different N_2 seedings: #13729 with $2.0{\cdot}10^{20}$ $m^{-3}s^{-1}$, #13730 with $3.7{\cdot}10^{20}$ $m^{-3}s^{-1}$ and #13731 with $4.5{\cdot}10^{20}$ $m^{-3}s^{-1}$.

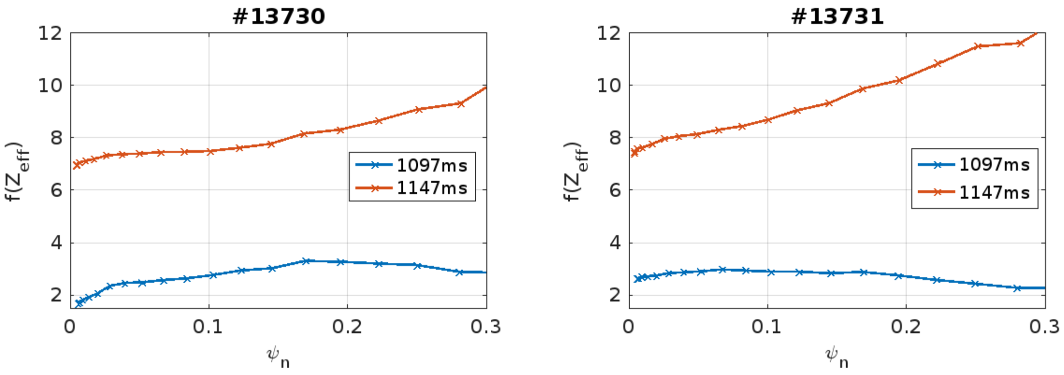

(a) (b)

Figure 5.23: Profiles of upper limits of effective charge Z_{eff} given by 5.17 representing accumulation of impurities during #13730 and #13731. Blue lines correspond to time before the N_2 seeding whereas red lines correspond to time after the N_2 seeding.

5.3 Application of tomography at JET

The Joint European Torus (JET) is a large tokamak (with major radius 2.96 m) with NBI and ICRH heating which is capable to run experiments with tritium. [1, 124, 57]. In order to focus experiments to the needs of the ITER tokamak, the JET machine went through several upgrades, in particular plasma facing components and the NBI heating. The ITER-like wall was installed in 2011 [125] consisting of beryllium limiters and a carbon composite divertor tiles coated by tungsten. The NBI heating system was increased from 20 MW up to 34 MW [126]. The main parameters of the JET tokamak are summarised in Tab. 5.4.

Toroidal mag. field	$B_T = 3.45$ T
Plasma current	$I_p = 4.8$ kA
Major radius	R = 2.96 m
Minor radius	a = 1.25 m
Elongation	$\kappa \leq 1.8$
Discharge duration	20-60 s
Plasma volume	$V = 100$ m^3
Plasma surface	$S =$ m^2
NBI heating power	$P_{NBI} \leq 34$ MW
ECRH heating power	$P_{ICRH} \leq 7$ MW

Table 5.4: Main engineering parameters of the JET tokamak [124, 57].

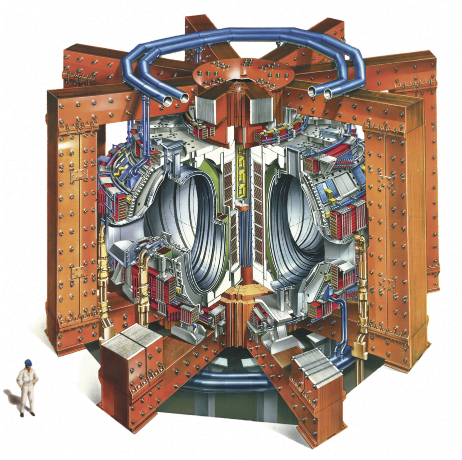

Figure 5.24: Cutaway drawing of the JET tokamak.

Application of SXR tomography at JET is challenging due to the geometry of the SXR diagnostics as it is shown in section 5.3.1. Following subsections are focused on reconstruction of $m > 1$ modes and reconstructions during mitigated disruptions.

5.3.1 Soft X-ray detectors at JET

The SXR radiation at JET is measured by three cameras H, V and T at different toroidal positions, see Fig. 5.25. The cameras V and T contain the photodiode array LD-35T, i.e. the same as at COMPASS. Their main parameters are listed in Tab. 5.2 whereas the camera H accommodates OSD196-OG(CER) [127] with the detection area 14×14 mm^2 and 250 μm of the Si substrate. Moreover, the cameras used to have different thickness of beryllium filters, see Tab. 5.5 causing a different spectral sensitivity, see Fig. 5.26.

Appropriate compensations have to be applied in order to perform tomographic reconstructions. For example, different beryllium filters can be compensated by an appropriate normalisation. Normalisation constants can be calculated by 1D tomography (abelisation) providing the total radiation seen by individual cameras which can be applied to normalise signals from different cameras relatively. However, this approach can lead to artefacts in reconstructed image as measurements from cameras can differ not only in profile amplitudes but also in their shape. Different toroidal locations of the SXR cameras can be compensated by applying appropriate time delays. However, an appropriate time delay does not have to be the same for the whole reconstructed region. Several other techniques are discussed in the next sections.

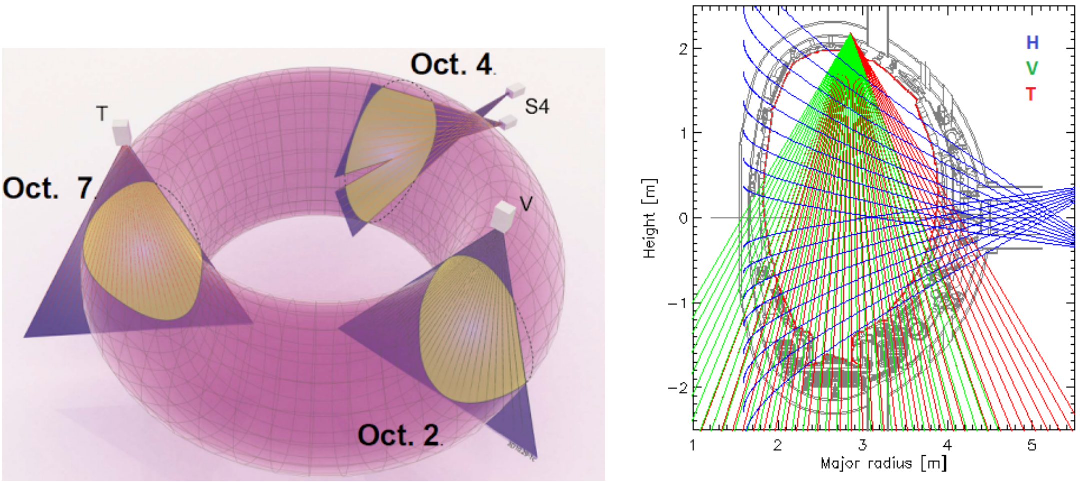

(a) (b)

Figure 5.25: Geometry of the SXR detectors at JET in 3D (a) [128] and the lines of sights projected to the poloidal cross-section.

Camera	#88000 #92504		
T	250	100	250
V	250	250	250
H	350	350	250

Table 5.5: Widths of the Beryllium filter (in μm) for the cameras V, T and H at JET. Filters were changed after pulses #88000 and #92504.

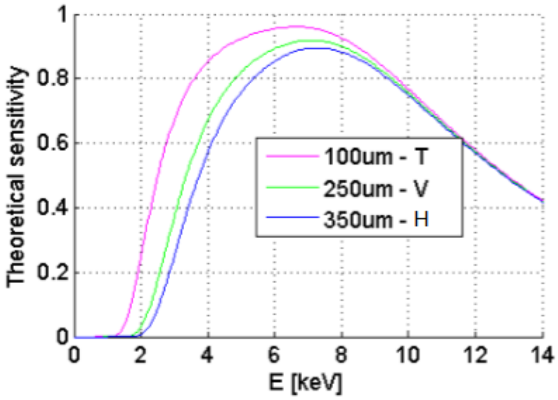

Figure 5.26: Theoretical spectral sensitivity of the SXR cameras at JET for the Be filters at thicknesses and 250μm of the diode active layer (transmitivities were taken from [117].

5.3.2 Techniques for reconstruction of MHD modes at JET

SXR tomography can provide positions and sizes of MHD modes which are among key parameters for comparison of their modelling with experiments. However, observation of MHD modes by means of SXR tomography at JET is complicated by different toroidal positions of the cameras, their different spectral sensitivity and in the case of higher mode numbers also by a sparse coverage of the plasma by the detectors. Different spectral sensitivities can be partly compensated by a relative calibration of the cameras which can be carried out by a ratio of radiated powers calculated from tomography using individual cameras. It can be done either by modified Abel transformation where pixels correspond to a space between nested magnetic surfaces (and not to regular annulus) or by MFR with a very high preference on smoothness along magnetic field lines, which is typically a more robust approach. Different toroidal positions can be, in the case of $m = 1$ modes, compensated by shifting a measurement of the cameras in time to synchronise measurements with respect to the mode phase. However, the reconstruction of the modes with higher numbers is limited by a sparse coverage of the plasma by SXR detectors.

Rotational tomography

A sparse coverage of the plasma could be compensated by rotational tomography which uses measurements from different phases (times) of MHD modes as measurements from a different geometry by rotating lines of sights according to the mode rotation. This brings more equations to the tomographic inversion and could allow reconstruction of the modes with higher m numbers. The process requires filtering out band-pass of frequencies close to the mode (and higher harmonics) and rotating chords along magnetic field lines reconstructed by EFIT. However, this approach turned out to have issues with convergence as it is sensitive to the precision of EFIT and it is also affected by changes of the emissivity during the mode rotation.

Tomography in frequency domain

Nevertheless, in order to obtain mode position and size, it is not necessary to fully reconstruct the MHD mode structure, but it can be sufficient to find a range of the flux coordinates where the mode appears. One possibility is tomographic reconstruction of amplitudes of the observed frequencies with preference of solutions with a very high smoothing along magnetic field lines (by applying high weights for derivatives along the magnetic field lines in the MFR). This approach also automatically solves the problem with observation of the modes at different phases due to different toroidal positions of the cameras. However, different higher harmonics for different channels (e.g. edge channel can see the $m = 1$ once per turn while a middle channel can see it twice) and the fact that the mode is not represented by one exact frequency given by the discrete Fourier transformation but rather by a narrow band of frequencies often leads (also together with a different sensitivity of the cameras) to artefacts in reconstructions and spatial aliasing. Localisation of MHD activity by means of MFR reconstruction in the frequency domain is demonstrated in Fig. 5.27 showing expected "ring" corresponding to an MHD mode with the frequency 25 kHz and also several artefacts in the plasma centre and on the HFS.

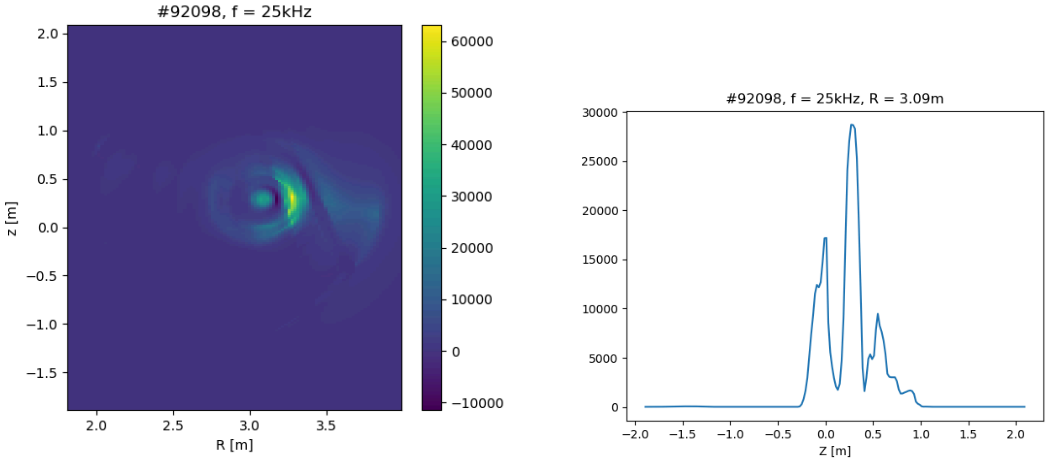

(b)

(a)

Figure 5.27: 2D reconstruction (a) and vertical profile (b) at the frequency 25 kHz.

Superposition of band-pass filtered data

The MHD mode can be also localised by tomography of the band-pass filtered data using just one camera in order to avoid issues with different toroidal positions and different spectral sensitivities of the cameras and applying preference on solution with a high smoothness along the magnetic field lines. In this approach, it has to be taken into account that as the mode rotates, it affects different channels with a different intensity (e.g. $m = 2$ mode can be seen at certain time just by one channel). Resulting reconstructions for $m > 1$ modes typically leads to "rings" changing their radius in time (e.g. in the case of $m = 2$ mode, a "ring" slowly grows until a collapse to a small ring when the mode is seen mainly by one channel) as the mode rotates through lines of sights. The moment when the ”ring” has the largest radius could represent the position of the mode allowing its localisation as it is shown in Fig. 5.28.

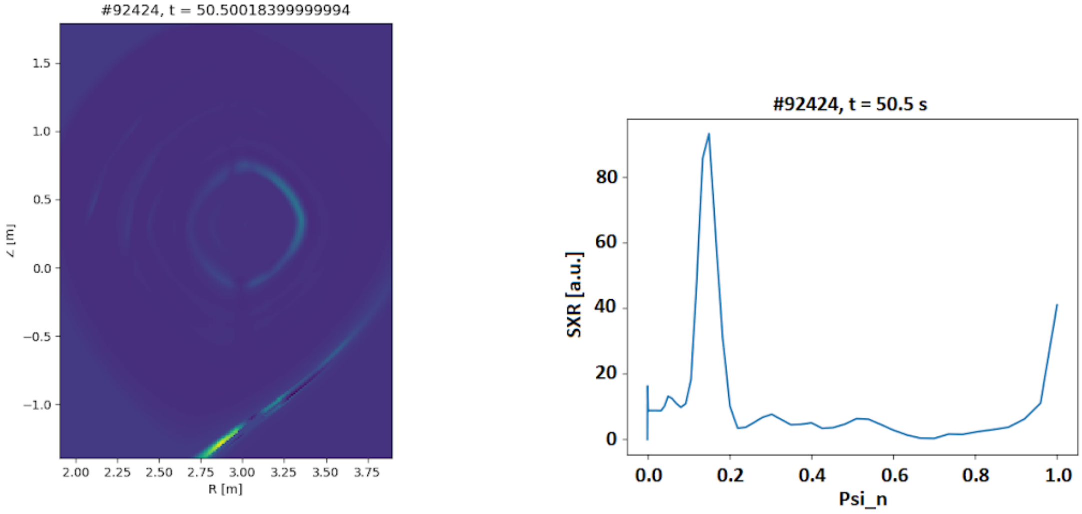

(a) (b)

Figure 5.28: SXR reconstruction of the band pass filtered data (a) and its 1D averaged profile (b) at ψ_N.

Options and limitations

From the above mentioned methods, the last one using the band-pass filtered data from one camera was observed to provide a reliable solution with a good convergence in most of the cases. However, it has several limitations as a method for finding the mode size. It strongly depends on the magnetic field and any misalignment between the SXR camera and the reconstructed equilibrium broadens the reconstructed ring. The plasma coverage is relatively sparse as a distance between chords in the plasma core is ~ 5 cm. Reconstruction can be affected in the case the mode position exceeds coverage of plasma by camera (e.g. on LFS in the case of camera V, see Fig. 5.25b) or in the case when a mode is localised in a region with low SXR radiation due to a lower temperature.

However, localisation of the mode as a position with maximum SXR is more straightforward and can supplement magnetic diagnostics, in particular in cases when the profile of safety factor q is flat and the mode position from EFIT can be affected by larger error. Moreover, it can also contribute to an estimation of the mode width as its calculation from magnetic measurements also depends on the mode position. Under several approximations (circular plasma, ideal wall, neglecting plasma current in the plasma edge outside the mode), the mode width can be expressed as [129]:

$$w \approx 4\sqrt{\frac{1}{2}\frac{R}{nB_T}\frac{r_c}{s_r}\cdot\left(\frac{r_c}{r_r}\right)^m B_{\theta 1}\left(r_c\right)} \tag{5.18}$$

where m, n are mode poloidal and toroidal numbers, $B_{\theta 1}\left(r_c\right)$ is poloidal magnetic perturbation, r_r is radial position of the mode (resonant surface corresponding to rational number of q), s_r magnetic shear at the mode position and r_c radial position of coil.

5.3.3 SXR tomography during mitigated disruptions

One among negative effects of disruptions, i.e. sudden terminations of plasma, are high heat loads which can damage plasma facing components, in particular in the case of larger machines like ITER with a higher ratio of the stored plasma energy and the interacting surface of the plasma facing components. One possibility how to mitigate these negative effects of the disruptions is to redistribute the heat loads in time and space by puffing impurities into the plasma in an early stage of the disruption, causing increased radiation losses and a plasma cooling before its termination. Impurities, typically inert gasses (due to their non-reactive properties) or their mixture with hydrogen, can be puffed by one disruption mitigation valve (DMV) or by their combination (in order to deal with radiation asymmetries). Behaviour of the plasma during the disruption depends on amount of the puffed impurities (and on a position of the valve or valves). Too weak impurity puff doesn't cause any significant loss of the plasma energy via radiation whereas too intense puff can cause a violent MARFE disruption. SXR are suitable in providing information about the transport of impurities into the plasma core and its cooling with a good temporal resolution as they are generated by the line radiation of impurities and by bremsstrahlung of hot particles from the plasma core [130, 131]. In order to distinguish between the two processes contributing to the SXR signal, additional information is required (e.g. plasma temperature and density). Tomography provides a local emissivity from the line integrated measurements which allow for an easier interpretation of the SXR signals and a distinction between the radiation from the hot core (contributed by bremsstrahlung) and the radiation from the plasma edge where bremsstrahlung is below detector's sensitivity and the line radiation of impurities can play a dominant role. It allows to see the plasma cooling as a drop of SXR in the plasma core (even though a signal from the detector directed to the plasma core is still increasing due to a line radiation of impurities puffed into plasma). Cooling of the plasma core can be also measured by ECE providing fast measurements of the temperature profile, but there can be present cutoff regions for ECE frequencies due to high electron densities.

A complex analysis of the mitigated disruptions requires an evaluation of the radiation losses, their asymmetry, heat loads of the plasma facing components, induced forces in the coils, impurity transport, delays and durations of the thermal and current quenches, etc. This section focuses on SXR tomography and its performance as a tool which can provide information about the impurity transport and the thermal quench during the mitigated disruptions with the Argon puff at higher plasma parameters with $I_{\text{plasma}} = 2.5\text{MA}$, $B_{T,0} = 2.5\text{T}$, $P_{\text{NBI}} = 14\text{MW}$. At JET, the mitigated disruption can be performed by puffing impurities just before disruptions initiated by the error field induced by the external coils (causing e.g. $n = 1$ mode) or solely by the impurity puff into a stable plasma which is the case of the disruptions in this section.

Since the SXR cameras at JET have different spectral sensitivities which can cause artefacts in reconstructions and a 1D profile of SXR has a potential to provide satisfactory information about penetration of impurities into the plasma core and its cooling, abelisation of one SXR camera (i.e. 1D reconstruction where pixels forms nested surfaces between magnetic field lines) could be a good choice for the reconstruction. However, this assumption of the total poloidal symmetry can cause problems with convergence. Instead, 2D tomography from one SXR camera with a restriction to search for solutions with a high smoothness along the magnetic field lines can be also applied and provides an acceptable solution as it can be seen in Fig. 5.29 showing hollow profiles of the SXR radiation corresponding to the line radiation caused by the Argon puff. The hollow profile shrinks as Argon penetrates into the plasma core as it is indicated by the reconstructed SXR profile in the next Fig. 5.30.

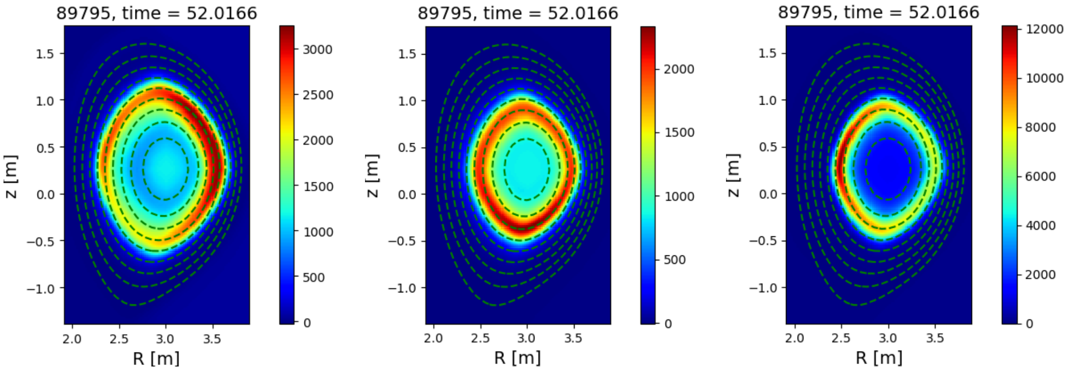

(a) Camera V (b) Camera H (c) Camera T

Figure 5.29: Tomography reconstructions preferring solutions with high smoothness along the magnetic field lines using data only from one camera. The hollow profile of the SXR distribution corresponds to the line radiation of Argon penetrating into the plasma core from its edge after the Argon puff.

An example of the reconstructed SXR profiles after the puff of Argon into plasma is shown in Fig. 5.30b where the penetration of impurities into the plasma core is observable 3 ms after opening the valve t_{DMV} just before the time of the disruption (t_{D}) and fast drop of core SXR indicating thermal quench starts 6 ms after t_{DMV}. The time of the disruption is chosen as a time of the peak of the plasma current corresponding to a collapse of the plasma current profile. Comparison of the reconstructed SXR in the plasma core and near the plasma edge with a different amount of the Argon puff in Fig. 5.31 shows increased delays of the beginning of the thermal quench and a slower evolution of the edge SXR emission until the disruption with the decreasing amount of the Argon puff. In this case, the slowest disruption occurred for the puff with 1% of Argon (the rest was deuterium) at a pressure of 0.3 bar whereas lower amounts of Argon did not lead to a plasma termination.

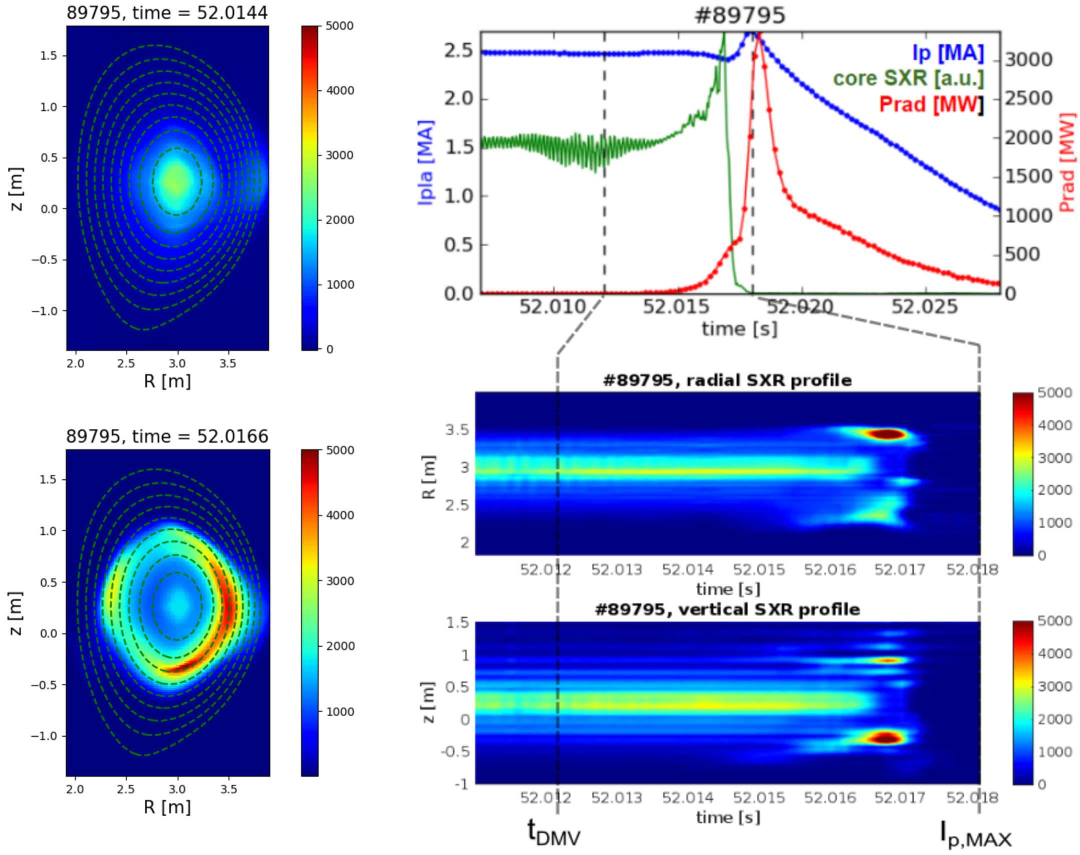

(a) (b)

Figure 5.30: SXR reconstruction (a) and evolution of the profiles (b) during the mitigated disruption. t_{DMV} represents the time of the opening of the disruption mitigation valve releasing Argon into the plasma whereas t_D represents the time of the disruption.

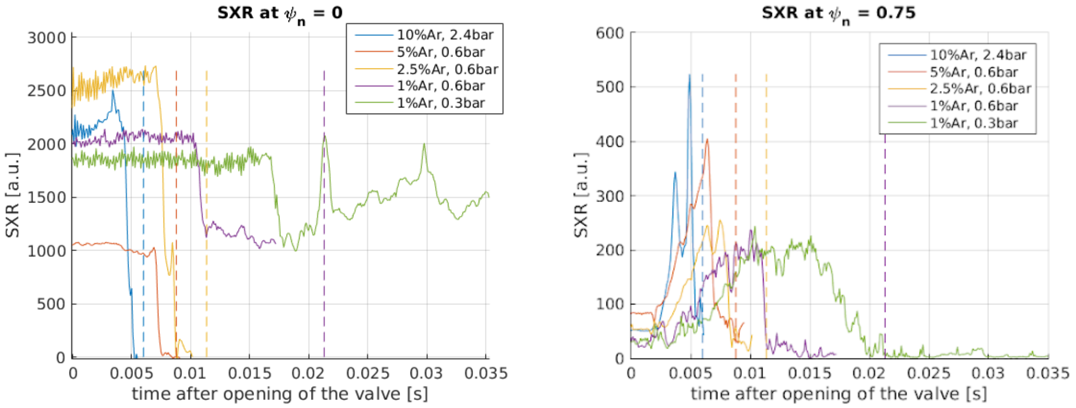

(a) (b)

Figure 5.31: (a) SXR at the plasma centre (at $\psi_n = 0$) and (b) near the edge SXR (averaged SXR at $\psi_n = 0.75$ contour). Times of the disruptions are marked by the vertical dashed lines. ψ_n is poloidal flux (described in 2.2) which is normalised so that it goes from 0 at magnetic axis towards 1 at separatrix.

5.4 Summary

The chapter covers several cases of application of the Minimum Fisher Regularisation (MFR) tomographic algorithm and its modifications at COMPASS and JET including description of the SXR and AXUV diagnostics at COMPASS and its calibration and the SXR diagnostic at JET. The chapter is related to the enclosed article A.2 dealing with optimisation of the SXR tomography.

The section about the SXR and AXUV detectors at COMPASS 5.2.1 also includes description of their spatial calibration which represented a considerable part of the work and also the relative calibration of SXR at CEA Cadarache showing a relative difference up to 10% in the detectors response.

In section 5.2.2, the SXR and AXUV tomography was compared with EFIT showing the same trend of the magnetic axis and the radiation centre during the discharges. The radiation centre can provide supplementary information about the plasma position which has a potential to be used for the real-time plasma control and its comparison with the magnetic axis can reveal systematic errors. As expected, there was a small difference in the vertical positions (about 1 cm) whereas the radial positions have shown a greater difference possibly caused by an increased radiation near the HFS limiter in the case of the circular discharges and by the plasma shape and Shafranov shift in the case of the D-shaped discharges. The difference between the positions of the magnetic axis and the reconstructed radiation centre could be also caused by a systematic error of EFIT as it is indicated in Fig 5.9 where the Photron camera indicates the plasma-wall interaction despite a 2 cm gap between the wall and separatrix reconstructed by EFIT.

Section 5.2.2 continued with testing reliability of the calculation of the radiation centre by the linear tomographic methods on the COMPASS SXR data which extends the work in the attached article A.3. The linear methods allow faster tomography than MFR and direct calculation of the distribution moments (e.g. radiation centre) at the expense of a lower precision. The differences between the direct calculations of the vertical positions of the radiation centre and the vertical positions of the magnetic axis reconstructed by EFIT were mostly smaller than the pixel resolution (1 cm). The differences in the radial positions exhibited a systematic shift towards LFS indicating the effect of plasma shape and the Shafranov shift. The shift was higher in the case of the linear methods than in the case of MFR. Among the tested linear methods, the method based on GEV decomposition shows the closest results to the MFR and with the lowest deviation of the SXR radiation centre (1 cm in the radial coordinate and 1.3 cm in the vertical coordinate).

The subsequent sections presented several cases of application of tomography at COMPASS. Section 5.2.3 dealt with the radiation losses seen by AXUV tomography. It started with comparison of the radiation losses during L-mode, ELMy H-mode and ELM-free H-mode showing a higher increase of measured radiation during H-mode with respect to the plasma density. A higher density is related to a lower plasma temperature due to dilution of the ohmic heating energy into more particles and due to increased radiation losses. Section 5.2.4 regards the radiation measured by AXUV during ELMs showing an expected (roughly) linear dependence of the radiation losses on the loss of the plasma energy seen by EFIT. Section 5.2.5 refered to the radiation losses measured by AXUV during the experiments focused on the detachment regime. The tomographic reconstructions of SXR and AXUV show that there is an optimal nitrogen puff reducing the heat flux reaching the divertor plates while keeping stable impurity radiation from the plasma core and avoiding the MARFE instability.

Section 5.3 shows several cases of application of tomography at JET. The SXR diagnostics are JET is not suitable for tomography of $m > 1$ modes due to the sparse plasma coverage, different berylium filters (until pulse #95204) and different toroidal positions of the SXR detectors. However, useful information about the modes could still be provided by tomography. The techniques for localisation of the $m > 1$ MHD modes are discussed indicating tomography of the band-pass filtered data as a possible method. Furthermore, SXR tomgoraphy during the mitigated disruptions demonstrates applicability of 2D tomography from one camera finding a solution highly smoothed along the magnetic field lines. Using only one camera allows to avoid issues with different berylium filters and finding a solution highly smoothed along the magnetic field avoids issues with missing the second camera for the 2D tomography. This approach is close to 1D tomography (abelisation), but allows a poloidal asymmetry and it is less constrained by the magnetic field which improves its convergence. It can be applied in order to observe propagation of the impurities towards the plasma core.

6. Sawtooth instability and its influence on selected plasma processes at COMPASS

The chapter provides a brief introduction into physics of the sawtooth instability followed by its characterisation at COMPASS and a study of its effect on selected plasma processes such as L-H transition, H-L transition, transition to ELM-free H-mode and ELM itself.

6.1 Introduction

The sawtooth instability was first reported in [132] (1974) and it is currently a common instability occurring in baseline tokamak scenarios [1]. It is associated with cyclic slow increases and fast drops of the core temperature which can be consequently seen as a sawtooth pattern (giving the instability its name) on several diagnostics such as measurement of the soft X-ray SXR radiation.

Although this instability affects a significant volume of the plasma, it hardly ever leads to a termination of a discharge. One of its main direct consequences is a limitation of the temperature and current density gradients in the plasma core.

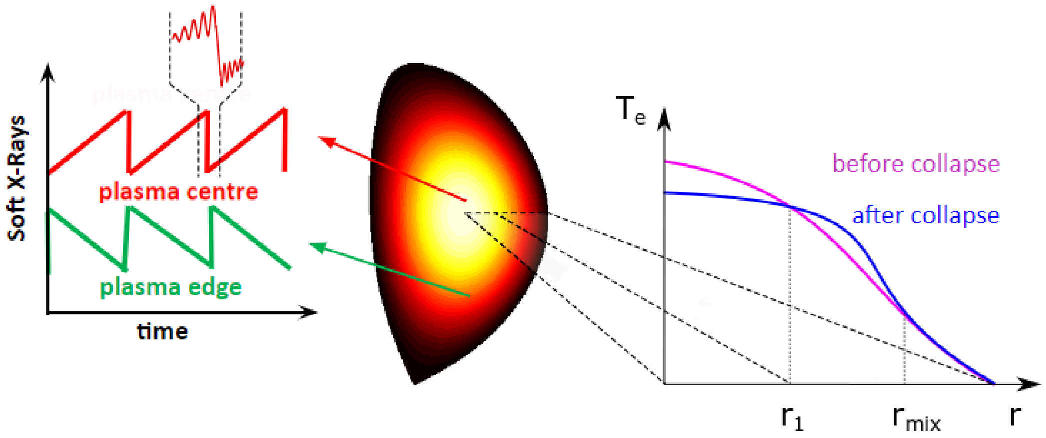

Figure 6.1: Evolution of the temperature profile and typical soft X-ray signals during the sawtooth instability.

The sawtooth instability is one of the most important topics in fusion physics for several reasons. Fusion-born alpha particles are predicted to lead to a longer sawtooth period. However, longer sawteeth were shown to trigger other instabilities such as Neoclassical Tearing Mode below their threshold causing further degradation of the plasma confinement [134, 135, 136, 137]. Nevertheless, the effect of the sawteeth instability is not purely negative as it can also help to remove

---

[1] Sawtooth oscillations were also observed in solar flare radio emission which suggests that this instability can be universal for current carrying toroidal plasmas [133]

a helium ash and impurities from the plasma core [138]. The sawtooth instability can be avoided by application of an additional heating in some operational scenarios, but it is still typically present in baseline plasma scenarios including ITER. In these scenarios, the sawtooth period can be controlled so that it does not trigger NTM. On the other hand, it is favourable to have the sawtooth period longer than the slowing down time of alpha particles [139]. Optimally controlled sawtooth instability can provide sawtooth period short enough to avoid seeding other instabilities and still longer than the slowing down time of alpha particles [139]. Otherwise, a significant part of their energy is lost before they can heat the core plasma. The sawtooth period can be controlled via several actuators including 2.4.1 electron cyclotron current drive (ECCD), ion cyclotron resonant heating (ICRH), Neutral Beam Injection (NBI) [139] affecting stability of internal kink mode which limits sawtooth cycle (as it will be described in next sections). The effect of NBI, which is installed at COMPASS. is studied in 6.4.1.

It is also observed that the sawtooth instability can help trigger a transition to a state with a better plasma confinement (H-mode) [140, 141, 142, 143, 144]. Overall, the sawtooth instability strongly affects the magnetic topology and profiles (in particular temperature and current profiles) of the plasma and has an impact on many plasma processes. The effect of the sawtooth instability on selected plasma processes at the COMPASS tokamak is the main focus of this chapter.

6.2 Theoretical background

The sawtooth instability has a periodic behaviour with a cycle which can be divided into four phases: ramp-up phase, precursor phase, fast collapse and post-cursor phase as shown in Fig. 6.1. Each phase has its own physical background and models.

6.2.1 Sawtooth ramp-up phase

The ramp-up phase represents the longest part of the sawtooth cycle. During this phase, the temperature profile gradually steepens (temperature rises in the plasma core and can decrease at its edge as it shown in Fig. 6.8) and the plasma current diffuses into the hotter and more conductive plasma core ($\sigma \propto T^{3/2}$) which leads to further steepening of temperature and current profiles. This process continues up to the point when the plasma becomes unstable and an internal kink mode ($m = 1$, $n = 1$) develops. Basically, duration of the ramp-up is constrained by a time required to reach conditions for an internal kink mode and a subsequent sawtooth crash to take place. These conditions are specified in the next section.

6.2.2 Pre-cursor phase

The pre-cursor phase represents the development of the internal kink mode (described in 2.4.1) and a growing displacement of the plasma core column as shown in Fig 6.2 (typically seen in signals of the magnetic or SXR diagnostics as oscillations with several tens of kHz as indicated in Fig. 6.1). A necessary condition for the internal kink mode instability is $q < 1$ (i.e. when an average inverse pitch of the magnetic field lines goes below one, see (2.33). It can be also seen as a point when a destabilising effect of the poloidal magnetic field overcomes a stabilising effect of the toroidal (axial) magnetic field (it takes energy to bend the magnetic field lines). Furthermore, the ideal internal kink mode becomes unstable when β_{p1} defined by formula 6.3 exceeds a critical value which can be derived from 6.2. The growing displacement of the hot core subsequently triggers the next phase called the sawtooth crash.

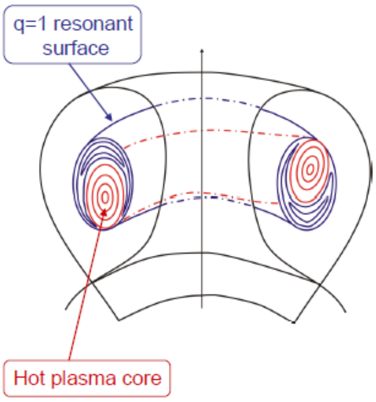

Figure 6.2: Displacement of the hot core during the internal kink mode [40].

Energy principle based on ideal MHD

Stability of the internal kink mode can be determined by the energy principle via change in the potential energy δW as a result of an arbitrary plasma displacement as it is shown in section 2.4.1 (i.e. expressing stability via sign of $\delta W = -\frac{1}{2}\int \vec{\xi} \cdot \vec{F} dV$, where $\vec{\xi}$ is the displacement and $\vec{F}$ the force). In the cylindrical approximation shown in the chapter 2.4.1, δW_{MHD} was expressed via the 4th order of expansion as lesser orders vanished. Taking into account the toroidal geometry modifies δW_p into:

$$\delta W_{\mathrm{MHD}} = \left(1 - \frac{1}{n^2}\right) \delta W_{4,cyl} + \frac{1}{n^2} \delta W_{4,tor} \tag{6.1}$$

where

$$\delta W_{4,\mathrm{tor}} \sim 3\left(1 - q_0\right) \left[\frac{13}{48(\nu + 4)} - \beta_{p1}^2 \int_{r_1}^{r_2} \frac{dr}{r_1} \left(\frac{r}{r_1}\right)^{\nu-5}\right] \tag{6.2}$$

as it was derived in [12] under assumption of the current profiles $j = [1 - (r/a)^\nu]$ with $q(0) \ll 1$. Here, r_1 and r_2 represent the radial positions at $q = 1$ and $q = 1$ and ν is a coefficient of the current profile.

$$\beta_{p1} = \left(2\mu_0 \int_0^{r_1} \left(\frac{r}{r_1}\right)^2 \left(-\frac{\mathrm{d}p}{\mathrm{d}r}\right) \mathrm{d}r\right) / B_{\theta 1}^2 \tag{6.3}$$

For $n = 1$, the cylindrical contribution vanishes and $\delta Wp = \delta W_{4,\mathrm{tor}}$ (note that for $n \gg 1$, the toroidal contribution vanishes and $\delta Wp = \delta W_{4,\mathrm{cyl}}$). The form of $\delta W_{4,\mathrm{tor}}$ implies that there is a critical pressure leading to the instability of the internal kink mode (if also $q(0) < 1$). However, the fact that δW for the internal kink mode is characterised by higher orders of δW expansion indicates that also other subtle effects such as sheared flows, collisionless kinetic effects related to high energy particles and thermal particles, non-ideal effects localized around $q = 1$, plasma shape, etc. may play a role. In practise, the Porcelli heuristic sawtooth crash trigger model is often used.

Porcelli model

Porcelli proposed a heuristic sawtooth crash trigger model [145] for different instability regimes which turned out to give reliable predictions [146, 147, 148, 149]. The model is based on the energy principle of the kink mode introduced in chapter 2.4.1 and includes other effects like resistivity, high energy ions and diamagnetic drifts. The model takes into account the potential energy of the internal kink mode in the form:

$$\delta\hat{W} = \delta\hat{W}_{\mathrm{core}} + \delta\hat{W}_{\mathrm{fast}} = \delta\hat{W}_{\mathrm{MHD}} + \delta\hat{W}_{\mathrm{tr}} + \delta W_{fast} \tag{6.4}$$

where $\delta\hat{W}_{\mathrm{MHD}}$ can be described by equation 6.2, $\delta\hat{W}_{\mathrm{tr}}$ is contribution of collisionless thermal trapped ions (also known as the Kruskal–Oberman term [150]) and δW_{fast} represents fast non-thermal particles. The Porcelli model predicts that the sawtooth instability is triggered when one of three following criteria (addressing different instability regimes) is met [145]:

$$\begin{aligned}
&-\delta\hat{W}_{\mathrm{core}} > c_{\mathrm{h}}\omega_{\mathrm{dh}}\tau_{\mathrm{A}} && \textit{effect of hot trapped ions}\\
&-\delta\hat{W} > \frac{1}{2}\omega_{*\mathrm{i}}\tau_{\mathrm{A}} && \textit{ideal internal kink}\\
&-c_{\rho}\hat{\rho}_i < -\delta\hat{W} < \frac{1}{2}\omega_{*\mathrm{i}}\tau_{\mathrm{A}} \quad \text{and} \quad \omega_{*i} < c_*\gamma_\rho && \textit{resistive effects}
\end{aligned} \tag{6.5}$$

where $\omega_{*i} = \frac{1}{n_{i1}r_1 eB}\frac{dp_i}{dr}$ is the ion diamagnetic frequency at $q = 1$, $\omega_{\mathrm{dh}} = \frac{T_{\mathrm{i}}}{eB_1 n_{\mathrm{i}} r_1}\frac{\mathrm{d}n_{\mathrm{i}}}{\mathrm{d}r}$ the magnetic drift frequency of hot ions, γ_ρ the resistive growth rate of internal kink, c_ρ, c_*, c_{h} numerical factors depending on plasma profiles (details in [145]) of order of unity, $\hat{\rho}$ the normalised ion Larmor radius $\hat{\rho}_i = \rho_i/r_1$ and the potential energies are normalised so that $\delta\hat{W} = \delta W R_0^3\mu_0/(6\pi^2 B_0^2|\xi|^2 r_1^4)$ [151].

The first inequality in 6.5 relates to the effect of high-energetic trapped particles as a consequence of conservation of the third adiabatic invariant (i.e. the magnetic flux through their precessional drift orbits). It becomes relevant when the high-energy trapped particles complete many orbits within a characteristic perturbation time $\left|\delta\hat{W}_{\mathrm{core}}^{-1}\right|\tau_{\mathrm{A}}$.

The second inequality in 6.5 reflects a regime when a negative change of the potential energy is sufficiently high to rely on the ideal internal kink mode model and other effects can be neglected.

The last two criteria in 6.5 describe a regime with $\delta\hat{W}$ small enough so that subtle resistive effects in a narrow layer near $q = 1$ become important. In this regime, the internal kink mode can be stabilised by diamagnetic frequency effects as it is expressed by the last criteria ($\omega_{*i} < c_*\gamma_\rho$) when the diamagnetic frequency ω_{*i} is larger than the growth rate of the mode γ_ρ evaluated at $\omega_{*i} = 0$ [145]. The last condition can be transformed into a condition for the magnetic shear at $q = 1$ [145] (since the growth rate depends on s_1):

$$s_1 = \frac{r_1}{q_1}\frac{dq}{dr} > s_{\mathrm{crit}} \approx \beta_{\mathrm{i1}}^{7/12}\frac{r_1}{L_n}\left(\frac{r_1}{L_p}\right)^{1/6} S^{1/6}\rho_{*i}^{1/2} \tag{6.6}$$

where $S = \tau_R/\tau_\mathrm{A}$ is the Reynolds (Lundquist) number, β_{i1} is the ion toroidal beta at the q = 1 surface, $L_n = n/|\mathrm{d}n/\mathrm{d}r|$ the density decay length and $L_p = p/|\mathrm{d}p/\mathrm{d}r|$ the pressure decay length.

The relation of the change of kink mode potential energy to the sawtooth crash trigger according to the last two conditions of the Porcelli model is summarised in Fig. 6.3.

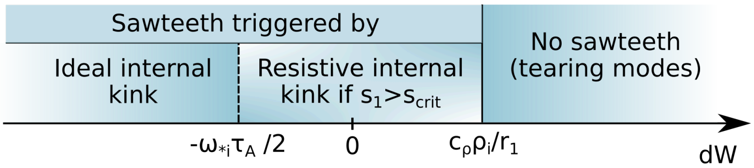

Figure 6.3: Criteria for the sawtooth crash trigger according to the Porcelli model.

Duration of sawtooth period

Duration of the sawtooth period is determined by a time required to reach the criteria for the sawtooth crash. If the current diffusion is a dominant mechanism, i.e. reachíng the condition $q(0) < 1$ by itself, the sawtooth period scales with the resistive time:

$$T_{saw} \sim \tau_R = \mu\sigma r_1^2 \tag{6.7}$$

which is indeed (roughly) observed, especially in experiments with a significant population of energetic particles prolonging the sawtooth period to a time closer to the ressistive time [16, 145].

However, the behaviour of the sawtooth period is often more complex as it is indicated by the second bracket in equation 6.2 where steepness of the current profile (ν) can compete with the pressure gradient (β_p) and as it is illustrated by the Porcelli model taking into account various subtle effects. In the cases when stability of the internal kink mode is associated with the critical pressure gradient or critical β (below which is the kink mode stable), the sawtooth period can be also linked with the plasma pressure, energy and energy confinement time [145]: $T_{saw} \sim \tau_E$.

6.2.3 Sawtooth crash

During the sawtooth crash, the heat is expelled from the plasma core to the edge, the central temperature drops rapidly, the temperature profile flattens (as shown in Fig. 6.1) and the heat pulse travels outward. There are several models describing a subsequent sawtooth crash.

Kadomtsev model

The first model was proposed by Kadomtsev [152] and it can still serve as an introduction into the mechanism behind the sawtooth crash. The Kadomtsev model [1] relies on resistive MHD allowing formation of magnetic X-point on the side with crowding magnetic field lines. Magnetic reconnection results in a creation and growth of a magnetic island. The hot core partially surrounded by this cooler island is then expelled to the edge and a new cylindrically symmetric magnetic field structure is established as it is illustrated in Fig. 6.4. In the Kadomtsev model, the reconnection process is concerned with the helical magnetic flux ψ_h with respect to the $q = 1$ surface. The field of ψ_h can be (for a large aspect approximation with $a/R \ll 1$) expressed as [1]:

$$B_h = \frac{d\psi_h}{dr} = B_\theta - (r/R)B_\phi = B_\theta(1 - q) \tag{6.8}$$

Redistribution of ψ_h during the re-connection in the Kadomtsev model is shown in Fig. 6.5. The initial helical magnetic flux $\psi_{h,i}$ starts with an extremum at r_1 ($q = 1$ surface) as it results from equation 6.8 and reconstructs into the final helical magnetic flux $\psi_{h,f}$ so that the fluxes with the same values at the opposite sides of r_1 connects to form the final helical flux with the same value at the radius r_f. The final helical flux is formed through the rule for conservation of helical flux [2]:

$$\left.\frac{d\psi_{h,i}}{dr}\right|_{r_i^-} dr = \left.\frac{d\psi_{h,i}}{dr}\right|_{r_i^+} dr = \left.\frac{d\psi_{h,f}}{dr}\right|_{r_f} dr \tag{6.9}$$

and via condition that the poloidal area of the plasma elements are conserved (under assumption that only the helical magnetic flux is changing and the toroidal magnetic field remains constant):

$$r_i^+ dr + r_i^- dr = r_f dr \tag{6.10}$$

Integration of the equation 6.10 for circular plasma:

$$\int_0^r r dr = \int_{r_-}^{r_1} r_- dr_- + \int_{r_1}^{r_+} r_+ dr_+ \tag{6.11}$$

can result in:

$$r_f^2 = r_+^2(\psi) - r_-^2(\psi) \tag{6.12}$$

showing that $q = 1$ surface moves to $r = 0$ and all surfaces starting with $q < 1$ are expelled outside the $q = 1$ surface. There are no changes outside the mixing radius r_{mix} which determines the end of the reconnection region and can be defined from the condition $\psi_{h,i}(r_{\text{mix}}) = \psi_{h,i}(0) = \psi_{h,f}(r_{\text{mix}})$.

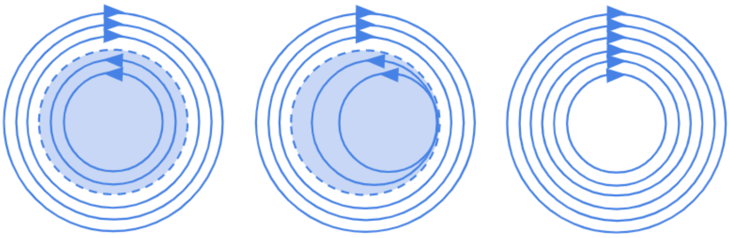

Figure 6.4: Development of magnetic field lines during the sawtooth crash according to the Kadomtsev model.

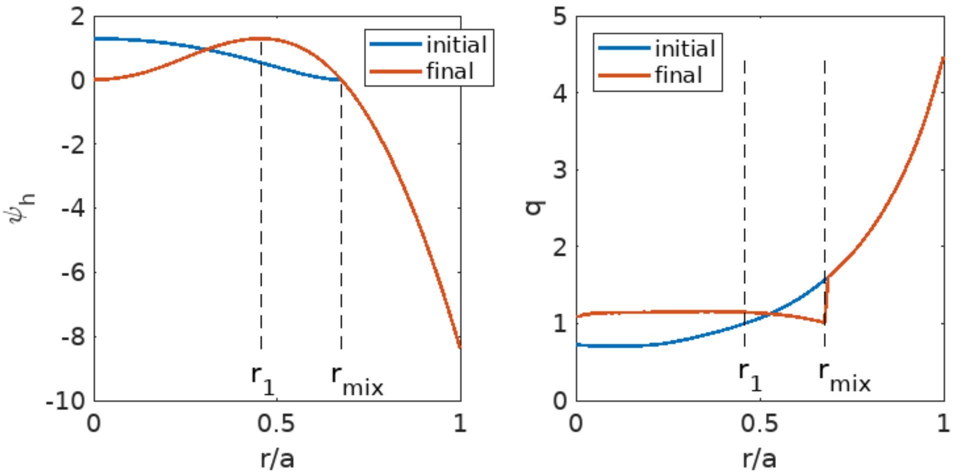

Figure 6.5: Helical magnetic flux and q profiles before and after magnetic reconnection with respect to the radial profile normalised by minor radius a according to the Kadomtsev model for discharge #7690. The initial profiles given by the METIS simulation were transformed into the final profiles according to equations 6.8, 6.9 and 6.10.

Duration of the sawtooth crash phase is in the Kadomtsev model given by the reconnection time from the Sweet-Parker reconnection model as a geometric mean of the resistive diffusion time τ_R and the Alfvénic time τ_A:

$$\tau_C = \sqrt{\tau_A \tau_R} = \sqrt{\frac{\mu_0^{3/2} r_1^3 \sqrt{n_e}}{\eta B_P}} \tag{6.13}$$

where η is plasma resistivity.

However, the Kadomtsev model has several problems such as shorter observed collapse times than predicted and sometimes observed $q(0) < 1$ even after the sawtooth crash. Alternative sawtooth crash trigger models, including quasi-interchange model [1, 153], the ballooning mode model and others (see [139] and references therein) were proposed, but they turned to be in a contradiction with measurements of the electron temperature by the electron cyclotron emission imaging system with high spatial and temporal resolutions on the TEXTOR tokamak [154, 155], where the sawtooth crash was observed to occur in a non-chaotic way and the hot plasma flowed through X-point of the instability, which was localized in the region of a good curvature (X-point on the inner side of torus with a good curvature is in contradiction with the ballooning theory).

Partial reconnection model

Currently, the widely accepted sawtooth crash trigger model is the partial reconnection model [145], which is not in conflict with electron temperature measurements on TEXTOR and observed $q(0) < 1$ after the sawtooth collapse. In the partial reconnection model, the sawtooth crash begins by a magnetic reconnection as in the Kadomtsev model, but the magnetic island grows only until it reaches its critical width. Inner core and magnetic island regions than undergo two different relaxation processes [139]. The core relaxes according to [153] (reaches a state with the minimum energy while conserving the magnetic helicity, i.e. $\nabla \times \vec{B} = \lambda \vec{B}$) whereas the island vanishes during the next ramp phase by means of diffusion of current sheets [146].

A posssible explanation for the incomplete reconnection was proposed in [156] and further examined for sawtooth in tokamaks in [157] as a result of the diamagnetic effect halting the reconnection when $v_{\mathrm{d,i-e}} = |\mathbf{v}_{d,\mathrm{i}} - \mathbf{v}_{d,\mathrm{e}}| > v_{\mathrm{A}*}$ where v_A is the outflow velocity from the reconnection region and $\mathbf{v}_{*i,e}$ the radial diamagnetic velocities $\mathbf{v}_{*i,e} = -\left(\nabla P_{*i,e} \times \mathbf{B}\right) / \left(Z_{i,e} e n_{i,e} B^2\right)$.

6.2.4 Post-cursor phase

After a sawtooth crash, a post-cursor phase can also appear which seems to be a sign of the incomplete magnetic reconnection during the sawtooth crash. The remaining magnetic island can be seen in signals of the magnetic and SXR diagnostics as in the case of the pre-cursor phase and vanishes during relaxation processes as it was described in the previous section about the partial reconnection model.

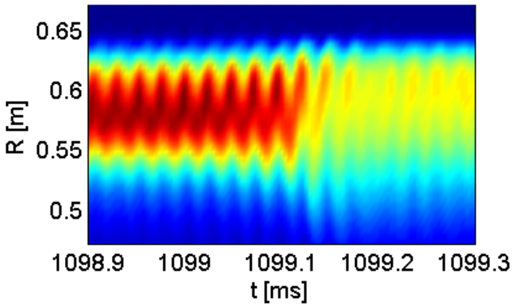

Figure 6.6: Horizontal profile of the SXR emission published in the attached article A.3. The oscillations show a kink mode before and after the sawtooth crash (#6071) illustrating partial magnetic reconnection at COMPASS.

6.2.5 Effect of NBI

Besides plasma heating, NBI also affects stability of an internal kink by changing a plasma rotation (gyroscopic stabilization) and a distribution of fast particles [139]. Fast particles can be trapped in banana orbits (represented by the first criterion in equations 6.5) or passing (completing full orbits). In the co-current regime, (i.e. NBI directed in the same direction as plasma current) passing particles can be stabilising, if they are inside the $q = 1$ region, and destabilising, if they are outside the $q = 1$ region, whereas in the case of counter-current regime (i.e. NBI directed in the opposite direction to the plasma current) the effect of passing particles is opposite [139].

The sawtooth period can exhibit a minimum in the counter-current regime as it is observed at JET [158] or MAST [159] or in the co-current regime as seen in TEXTOR [160]. Numerical modelling of the kink mode potential energy revealed that the minimum of sawtooth period is caused by energetic particles in the case of JET [139], flow effects in the case of MAST (relatively high NBI power applying a big torque to a relatively small plasma resulted in a high toroidal rotation) [159] and a competition of these effects in the case of TEXTOR [160] where the minimum occurred when the plasma toroidal rotation stopped. The effect of the NBI heating on the sawtooth instability at COMPASS is described in chapter 6.4.1.

6.3 Used signals and data processing

For a simple detection of a sawtooth instability, a single detector measuring the core SXR emission (e.g. 24th detector of the camera A shown in Fig. 5.4a) is usually the most suitable whereas the tomography reconstruction of the 2D SXR profile (described in section 5.1) from all SXR signals can provide more details about dynamics of the instability.

In the following sections, sawtooth parameters (in particular the period of the sawtooth cycle) is compared with the following plasma quantities: averaged electron density n_e, central electron temperature $T_{e,0}$ (from Thomson scattering), β_p (from EFIT), plasma thermal energy W (from EFIT), NBI power P_{NBI}, resistive time τ_R and confinement time τ_E.

The resistive time (representing a speed of redistribution of the plasma current during a sawtooth) is represented by its global (averaged) value and it was estimated by substituting the averaged resistivity $\eta = \frac{U_{loop}}{I_{plasma}} \frac{S}{2\pi R_0}$ into the equation for the resistive time 6.7:

$$\tau_R = \mu a^2 \frac{I_p}{U_{loop}} \frac{l}{S} \tag{6.14}$$

The energy confinement time τ_E is calculated with the ssumption of $dW/dt = 0$ during the steady state phases from 3.12:

$$\tau_E = \frac{W}{P_{ohm} + c_{nbi} P_{NBI}^{inj}} \tag{6.15}$$

where c_{nbi} is a rough estimation of absorption for NBI depending on injected NBI power (due to the divergence and consequent flipping of NBI beam) and plasma density [161]:

$$c_{nbi} = (1 - e^{-P_{NBI}/P_c})(1 - e^{-n_e}) \tag{6.16}$$

where $P_c = 230$ kW.

Most of the selected plasma parameters are global (averaged). Although local quantities (e.g. β_{p1} instead of β_p) could be more appropriate for characterisation of the sawtooth behaviour, the global quantities are more easily measured and they can still serve for characterisation of the sawtooth behaviour (as it will be shown in the next sections). The values correspond to the middle of the sawtooth phase, but no significant change in the fitted trends was observed for different phases of sawteeth. One exception is the central temperature T_{e0}, which is measured with a higher frequency (60 Hz) than the frequency of sawteeth at random sawtooth phases and can change significantly during one sawtooth period as it can be seen in Fig. 6.8. Nevertheless, the measured central temperature T_{e0} shows dependencies on the sawtooth period under appropriate statistics shown in the next sections.

Fitting in the following chapters was performed by the Trust region reflective method [162] using so-called Robust least square regression by means of bisquare weights (included in a toolbox of MATLAB 2020a). The root mean square error (RMSE) was chosen to represent the goodness of fit.

Analysed events were detected semi-automatically (checked manually after automatic detection) as follows: sawtooth crashes as peaks in the derivative of the core SXR signals smoothed by a triangular function, ELMs were detected as peaks in the D_α signals and L-H transitions or H-L transitions as a steep rise or fall in D_α by means of the algorithm described in [163].

6.4 Characterisation of the sawtooth instability at COMPASS

At the COMPASS tokamak, the sawtooth instability is present in the vast majority of the D-shaped scenarios and vanishes only in rare cases, e.g. when a sufficiently high counter-current NBI heating is applied and other MHD modes infuencing the current density profile are present. The most suitable diagnostic for detection of the sawtooth instability are SXR detectors, described in the chapter 5.2.1. An example of evolution of the SXR radiation and its tomographic reconstructions during the sawteeth are shown in Fig. 6.7. Typically, the sawtooth period is about 2 ms during the L-mode, but it can increase up to 10 ms during the NBI heating in H-mode. The inversion radius ranges from 0.06 m to 0.1m. The sawtooth crash typically lasts less than 0.1 ms, which is of the same order as it is estimated by the Kadomtsev model (substituting 6.14 into equation 6.13), but also the observed post-crash oscillations indicating an incomplete reconnection are often observed on the SXR signals, especially during the NBI heating.

Even though the sawtooth instability originates in the plasma core, it is observed that at COMPASS, a small device where the core and edge plasmas are coupled, it strongly affects numerous plasma processes even at the plasma edge including the L-H or H-L transitions or occurrence of ELMs. Behaviour of the sawtooth instability at COMPASS is described in the following subsections, 6.4.1, 6.4.1, whereas its influence on selected plasma processes is shown in section 6.5.

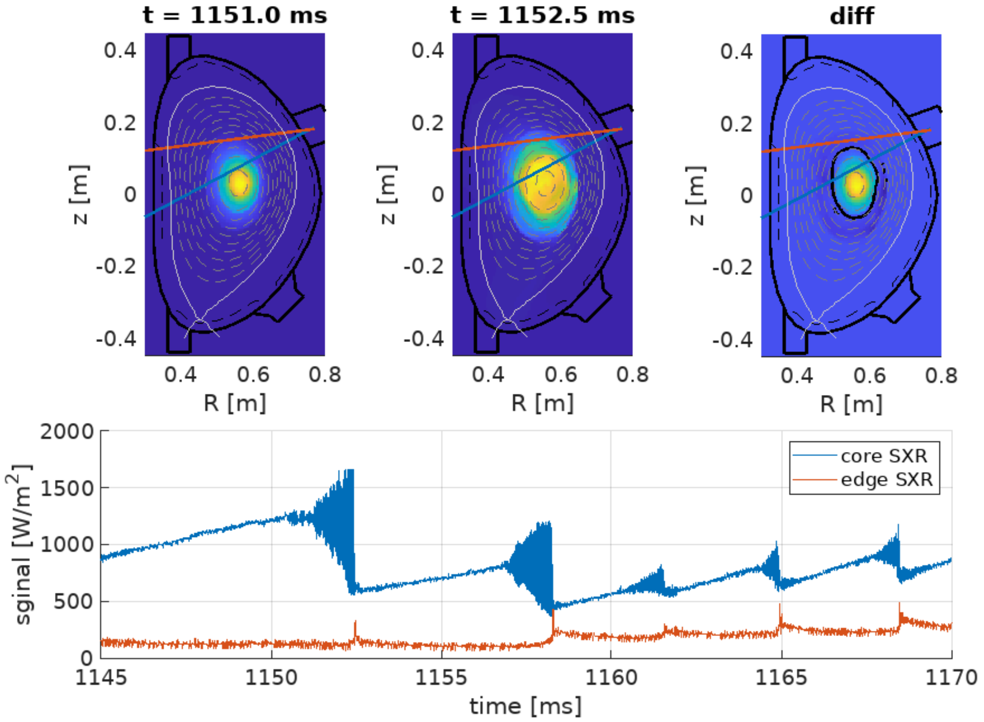

Figure 6.7: Examples of the reconstructed SXR emissivity profiles (from discharge #5751). Peaked SXR emissivity profile before sawtooth crash (top-left), broader SXR emissivity profile after the sawtooth crash (top-middle), their difference indicating inversion radius (black ring in the plasma core) and evolution of the SXR signals from the plasma core and edge showing a typical sawtooth pattern with precursor and postcursor oscillations (top-right bottom). In this case, the maximal estimated reconstructed emissivity dropped from 18 kW/m^3 to 4 kW/m^3 and the inversion radius was about 6 cm (in the radial direction).

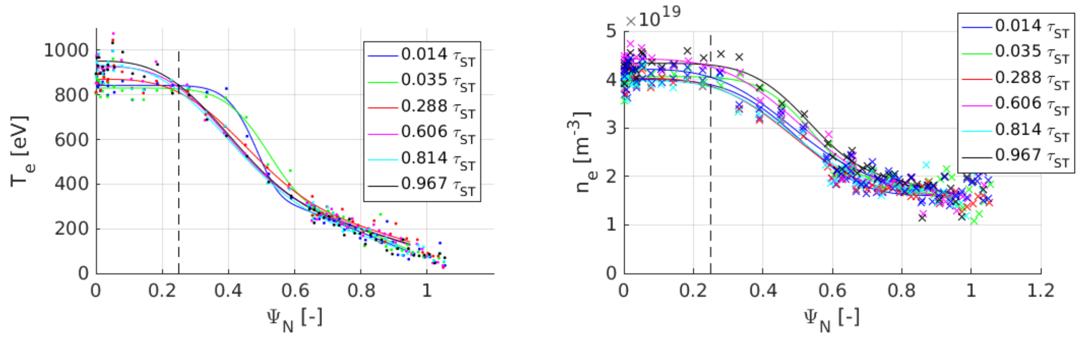

(a) (b)

Figure 6.8: Demonstration of the electron temperature (a) and density (b) profiles measured by the Thomson scattering diagnostics during different phases of the sawteeth at COMPASS (#7690). The dashed line shows a position of the inversion radius.

Internal kink mode growth rate

At COMPASS, an applicability of theoretical models has its limitations due to uncertainties in measurements of core profiles. The internal kink mode is often observed during the NBI heating by SXR detectors as oscillations in distribution of SXR profile indicating exponentially growing displacement of the plasma core:

$$\xi = \xi_0 e^{-\gamma t} \tag{6.17}$$

where ξ_0 in an initial displacement and γ observed growth rate. An example shown in Fig. 6.4 shows a displacement growing up to 3 cm before the sawooth crash and growth rate $\gamma = 4.6 \cdot 10^3$ s $^{-1}$ which is comparable to the growth rates at ASDEX-U ranging from 10^3 s $^{-1}$ to 10^4 s $^{-1}$ in [164]. On rare occasions and during the NBI heating, continuous internal kink (also called Long lived mode) without sawteeth can be also observed (e.g. in #6358, #6071).

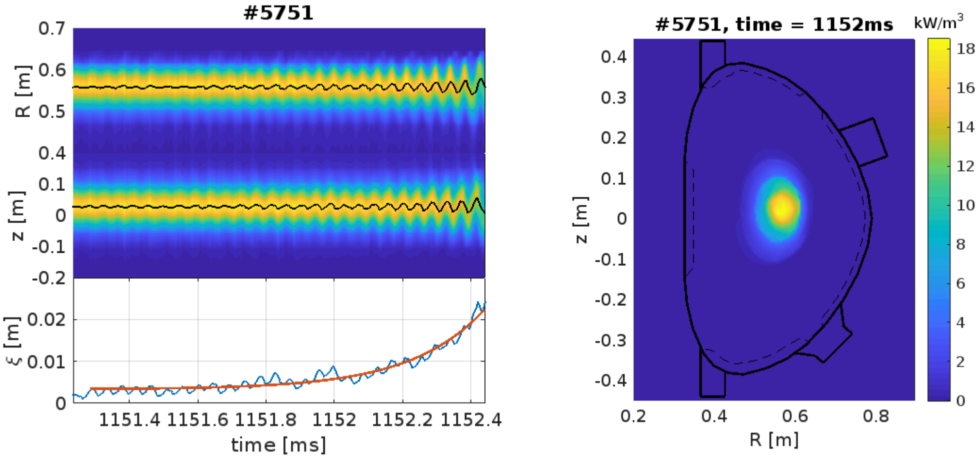

(a)

(b)

Figure 6.9: (a) Reconstructed SXR vertical and horizontal profiles indicating the growth rate of internal kink mode and (b) 2D SXR reconstruction.

Porcelli criteria

At COMPASS, verifying Porcelli criteria is problematic as it requires determining core plasma parameters including ion pressure profile which is not measured. Moreover, the terms for the potential energy of the kink mode represents theoretical approximation. Nevertheless, results from METIS simulations indicate a consistency with the resisitve regime, see Tab. 6.1 and Fig. 6.10. The contribution of fast particles $\hat{W}_{\text{fast}}$ is not included in Tab. 6.1 and requires simulations of their profile distribution. However, the $\hat{W}_{fast}$ term is supposed to be negligible without the NBI heating. During the NBI heating, the sawtooth period changes significantly but it keeps similar tendencies as it will be shown in section 6.4.1. Moreover, ion Larmor radius is comparable to the resistive layer width $\delta_\eta = s_1^{-1/3}(S)^{-1/3} r_1$ [145] which is a width of current layer where reconnection can take place. This implies a possible importance of subtle effects of finite Larmor radius and collisional resistivity associated with the resistive regime during the sawtooth crash [145]. The resistive regime is often observed e.g. at JET [165] or TEXTOR [166] which is a device of similar size and similar length of sawtooth period as in the case of COMPASS [167]. The term $\hat{W}_{\mathrm{MHD}}$ is given by the right side of formula 6.2 and the contribution of trapped particles $-\delta\hat{W}_{\mathrm{tr}}$ in Tab. 6.1 is approximated according to the formula derived in [151, 145]:

$$\delta\hat{W}_{\mathrm{tr}} = \frac{1.5}{6\pi}\left(\frac{r_1}{R_0}\right)^{-3/2}\beta_{i0}\tilde{cp} \quad \text{with} \quad \tilde{c_P} = \int_0^1 x^{3/2}\frac{p_i}{p_{i,0}}\,\mathrm{d}x \quad \text{and} \quad x = \frac{r}{r_1}. \tag{6.18}$$

discharge	5751	6071	6358	7677	7690	18200
time [ms]	1060	1100	1160	1120	1120	1120
I_p [kA]	241	178	236	342	212	223
$n_{e,0}$ [10^{19}m^{-3}]	11.2	11.1	12.5	3.5	4.6	9.4
P_{NBI} [kW]	0	684	307	0	0	742
$-\delta\hat{W}_{\mathrm{MHD}}$ [10^{-3}]	-7.8	-8.5	-14.4	-12.8	-7.2	-1.8
$-\delta\hat{W}_{\mathrm{tr}}$ [10^{-3}]	-12.2	-21.6	-11.0	-0.7	-1.9	-32.2
$1/2\omega_{*i}\tau_A$ [10^{-3}]	9.1	2.8	2.7	0.3	2.3	11.4
δ_η [mm]	1.9	1.7	2.6	1.7	1.6	1.5
$\rho_{i,1}$ [mm]	2.0	2.2	2.2	1.2	1.3	2.3
ν [-]	1.9	0.8	2.7	2.4	1.2	0.6
s_1 [-]	0.47	0.15	0.20	0.26	0.34	0.24
r_1 [m]	0.11	0.05	0.10	0.12	0.09	0.04
r_2 [m]	0.18	0.15	0.18	0.21	0.17	0.12

Table 6.1: Main plasma parameters, results from METIS simulations and variables relevant to the Porcelli model for various discharges.

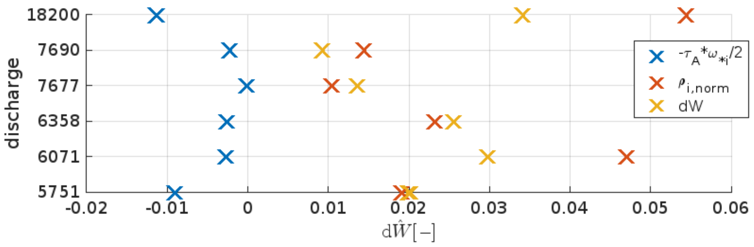

Figure 6.10: The Porcelli criteria and the change of potental energy approximated as $\mathrm{d}W = \delta\hat{W}_{\mathrm{tr}} + \delta\hat{W}_{\mathrm{MHD}}$ for various discharges.

6.4.1 Sawtooth period

Scan over the electron density

Scan over electron density is a good candidate for characterisation of the sawteeth as a controllable change in the plasma density also affects other (not directly controllable) plasma parameters important for the sawtooth behaviour like plasma pressure, temperature, poloidal beta and plasma resistivity (as it can be seen e.g. from formulas 6.2 and 6.5).

The effect of changing plasma density while other controllable plasma parameters like plasma position, shape, current and toroidal field remain fixed is summarised in Fig. 6.11 and table 6.2. The electron density ranged from $2 \cdot 10^{19} m^{-3}$ to $13 \cdot 10^{19} m^{-3}$ while the position of the magnetic axis, the plasma shape, the plasma current and the toroidal field were fixed to standard values: $R_0 = 0.565$

m, $z_0 = 0.025$ m, $a = 0.17$ m, $\kappa = 1.8$, $\delta_{upper} = 0.25$, $\delta_{lower} = 0.5$, $I_{plasma} = 180$ kA, $B_T = 1.15$ T.

These experiments show that the sawtooth period doesn't increase with the global resistive diffusion time and the core temperature (in contrast to [168] where the sawtooth period at JET increased with the temperature), i.e. it does not follow relation 6.7 when the sawtooth behaviour is dominated by current diffusion into the plasma core. The sawtooth period increases with the energy confinement time, plasma pressure (indicated by β_p and $n_e T_e$ values) and density. These trends are consistent with the Porcelli criteria $s_1 > s_{crit}$ during the resistive regime since s_{crit} increases mainly with plasma density decay length which increases with density as its profile is typically flat near the $q = 1$ region. However, the sawteeth can also affect the plasma kinetic energy as a less frequent redistribution of pressure profile could lead to lower energy losses and a better energy confinement time.

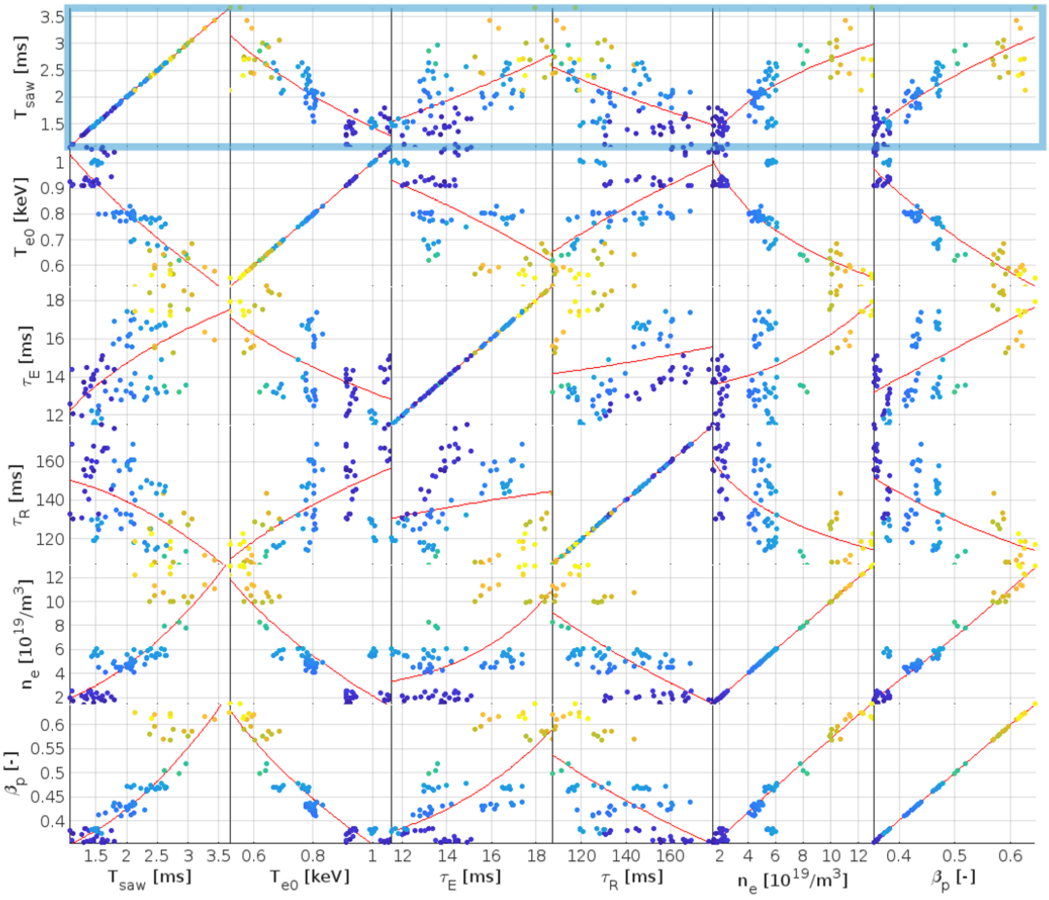

Figure 6.11: Relation of the sawtooth period to the density, central temperature and loop voltage during the density scan (with $I_p = 180kA$, $B_T = 1.15T$). Different colors represent different densities.

plasma parameter	p_1	p_2	p_3	$RMSE$
T_{e0} [keV]	-2.44e+02	1.08e-02	2.45e+02	3.19e-01
τ_E [ms]	1.87e-02	1.64e+00	5.05e-01	4.65e-01
τ_R [ms]	-8.87e+00	1.27e-01	1.86e+01	5.02e-01
n_e [10 $^{19}/m^3$]	1.55e+00	3.14e-01	-4.89e-01	3.51e-01
β_p [-]	2.34e+02	1.22e-02	-2.29e+02	2.79e-01
W [J]	**1.11e+00**	**2.78e-01**	**-8.22e+00**	**2.76e-01**

Table 6.2: Coefficients $p_{1,2,3}$ of the fit function for the sawtooth period during the density scan in the form $\tau_{saw} = p_1 \cdot x^{p_2} + p_3$ and RMSE as an indicator of goodness of fit. The fit corresponds to the first row in the Fig. 6.11 where it is shown as the red curve. RMSE is low especially for β_p and W

Effect of Neutral Beam Injection at COMPASS

Sawtooth instability is strongly influenced by NBI at COMPASS and its period can increase from 2 ms up to 10 ms. Dependence of sawtooth period on applied NBI power shown in Fig. 6.12 indicates minimum for $\mathrm{P_{NBI}} = -300\,\mathrm{kW}$ in counter-current regime. For higher counter-current NBI power, sawtooth instability usually vanished due to other MHD modes. The observed kink frequency increases with applied NBI power. It indicates a possible significant increase of toroidal rotation which is supposed to represent significant part of the measured-kink frequency according to the formula 2.45.

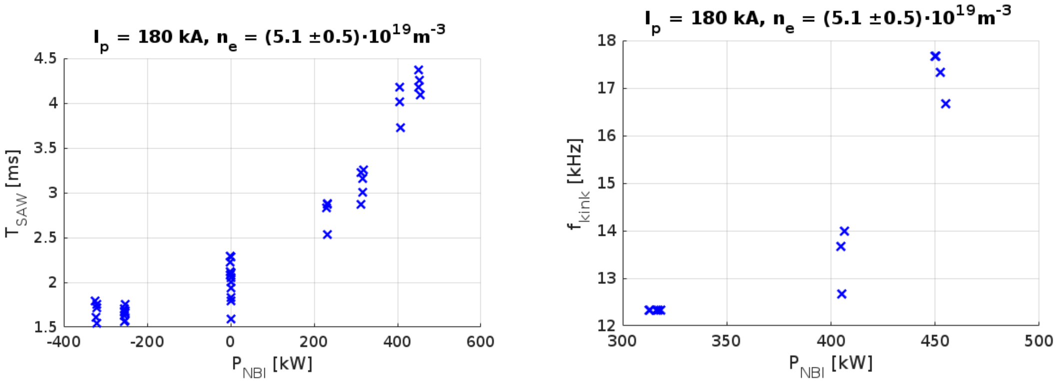

(a) (b)

Figure 6.12: Effect of the applied NBI power on sawtooth period (a) and on observed kink frequency (b) at COMPASS.

Scan over both the NBI power and electron density n_e while other controllable plasma parameters remained fixed to the same values as in section 6.4.1 during the density scan is summarised in Fig. 6.13 showing that the sawtooth period increases with n_e, $\mathrm{P_{NBI}}$, τ_E and β_p.

Dependence of the sawtooth period on $\mathrm{P_{NBI}}$ and n_e, β_p or τ_R is also shown in Fig. 6.14 where the fits for $\mathrm{P_{NBI}}$ and β_p show the lowest dependence on $\mathrm{P_{NBI}}$. In principle, this scan over n_e and $\mathrm{P_{NBI}}$ shows similar basic behaviour of sawtooth period as in the case of the density scan in chapter 6.4.1, i.e. scaling of the sawtooth period with β_p (or plasma thermal energy as the plasma current is fixed) indicating that stability of the internal kink mode is associated with the increased density and pressure gradient during the NBI heating as well.

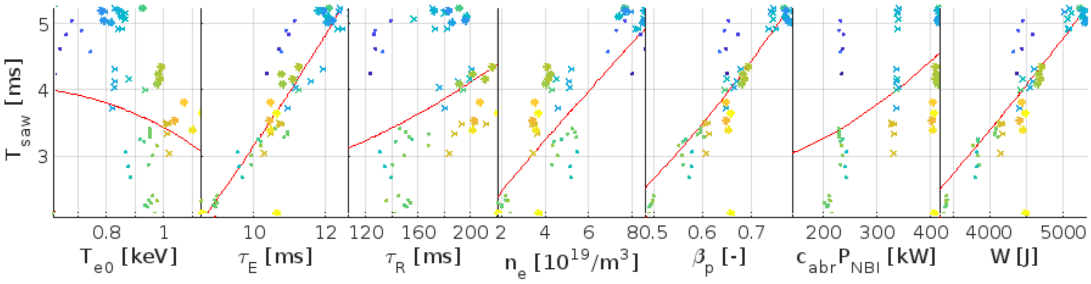

Figure 6.13: Sawtooth period and selected plasma parameters during scan over density and NBI power (with I_p = 180kA, B_T = 1.15T). The density is represented by different colors whereas NBI is represented by different marks.

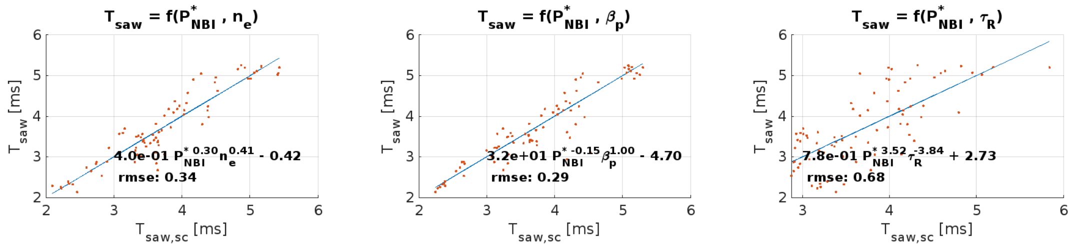

(a) (b) (c)

Figure 6.14: 2D fitting of the sawtooth period during the scan over NBI heating and selected plasma parameter: (a) electron density n_e, (b) β_p and (c) global resistive time τ_R.

Enlarging statistics over various experiments with H-mode performed at COMPASS between discharges #18248 and #20200 (almost 300 discharges) shows similar tendencies to those indicated for the density scan in section 6.4.1 and NBI scan in chapter 6.4.1, i.e. an increase of the sawtooth period with the density, NBI and β_p (or plasma kinetic energy W) is shown in Fig. 6.15. These trends are clear despite a higher diversity in plasma parameters and different plasma modes as both L-mode and H-mode plasmas during a steady state phase (i.e. stable plasma current and plasma shape) are included. Increasing trends with the density and the plasma kinetic energy are also shown in Fig. 6.16c where selecting plasma kinetic energy and NBI heating for fitting of the sawtooth period leads to a dominant dependence of the sawtooth period on the plasma kinetic energy and a negligible dependence on the NBI heating. It could indicate that stability of the internal kink mode at COMPASS is more related to the thermal plasma energy and pressure than to the toroidal rotation induced by NBI. However, NBI power and plasma kinetic energy are dependent variables in the fit of sawtooth period and there are missing data near the boundary regions. Nevertheless, plasma kinetic energy can be considered as a plasma parameter which is well connected with sawtooth period.

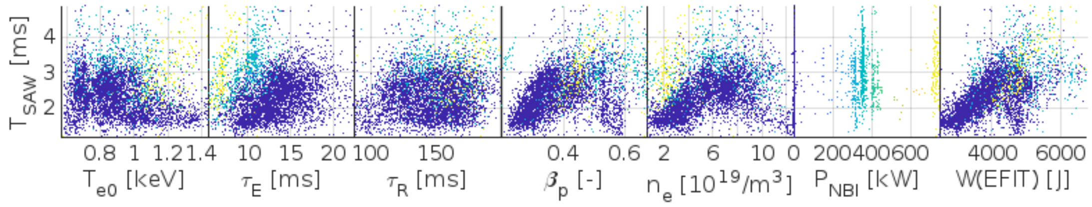

Figure 6.15: Relation of the sawtooth period to the selected plasma parameters (between the discharges #18248-20200). Different NBI power is distinguished by different colours.

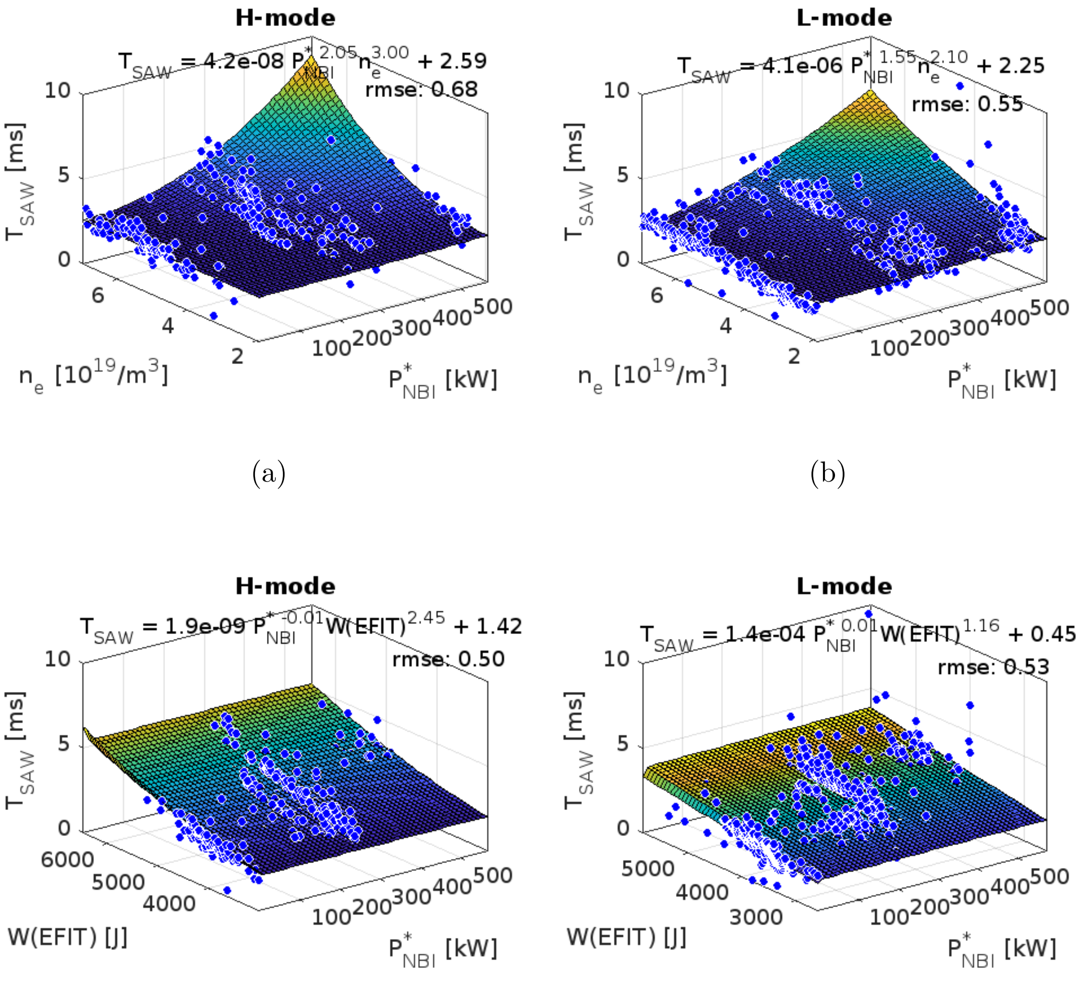

(a) (b)

(c) (d)

Figure 6.16: Visualisation of fitting the sawtooth period over the NBI heating $P^*_{NBI} = c_{nbi} P_{NBI}$ and n_e (top) and over the P^*_{NBI} and $W(EFIT)$ during H-mode (left column) and L-mode (right column).

The effect of NBI has a delay several tens of ms due to the time required to transfer energy from NBI to plasma. An example in Fig. 6.17 shows that after application of the co-current NBI the sawtooth period gradually increases for about 50 ms until it saturates and frequency of the internal kink mode follows. It indicates that the plasma requires roughly 50 ms to equilibriate after an application of the NBI). The delayed effect of the NBI is affected by slowing down time of injected deuterium ions. At COMPASS, with beam energy 40 keV and electron temperature about 1 keV, the slowing down time of NBI ions ranges from 10 ms to 50 ms for densities ranging from $2 \cdot 10^{19}$ m $^{-3}$ to $10 \cdot 10^{19}$ m^{-3} (with inverse proportion to the electron density) [169]. Response function of sawtooth period to the applied NBI power in Fig. 6.17 (from deconvolution of the NBI power and sawtooth period) shows maximum at about 20 ms which is comparable to the estimated slowing down time about 25 ms for electron density $n_e = 4 \cdot 10^{-3}$ m^{-3} in this discharge. The inversion radius remained roughly at 7 cm during the discharge #4415 (as shown in Fig. 6.17).

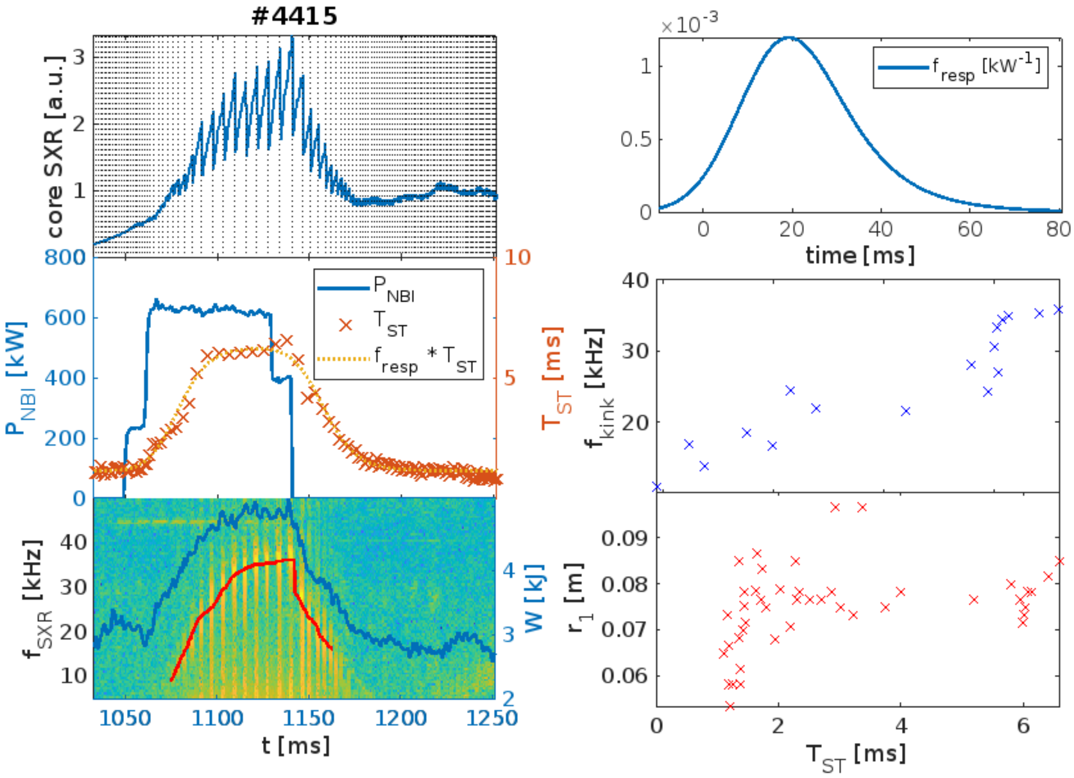

Figure 6.17: Effect of NBI on the sawtooth period at COMPASS during the discharge (# 4415). The left column shows evolution of the core SXR (top), the applied NBI power with the observed period (middle) and the spectrogram with traced frequency of the kink mode (red line) and plasma energy from EFIT (bottom). The right column contains the response function of the sawtooth period to the NBI power (top), kink frequency with respect to the sawtooth period (middle) and inversion radius with respect to the sawtooth period (bottom). Convolution of the response function and NBI power is also shown as a dotted orange line in the left middle plot.

Difference between L-mode and H-mode

The sawtooth period also depends on the plasma regime as it is shown in Fig. 6.18 where the sawtooth period with respect to the averaged plasma density n_e and plasma energy W seems to be prolonged by cca 0.3 ms. However, this diffeence can be also affected by a different systematic error of the plasma kinetic energy calculated by EFIT in the L-mode and H-mode due to the changes of the plasma profiles.

For higher densities ($n_e > 8 \cdot 10^{19}/m^3$), the sawtooth period seems to change its trend and starts decreasing. It typically takes place under a higher radiative cooling, i.e. lower plasma temperatures. If these cases are excluded from the statistics, dependence of the sawtooth period on the plasma energy becomes more evident as it is also shown in Fig. 6.18a.

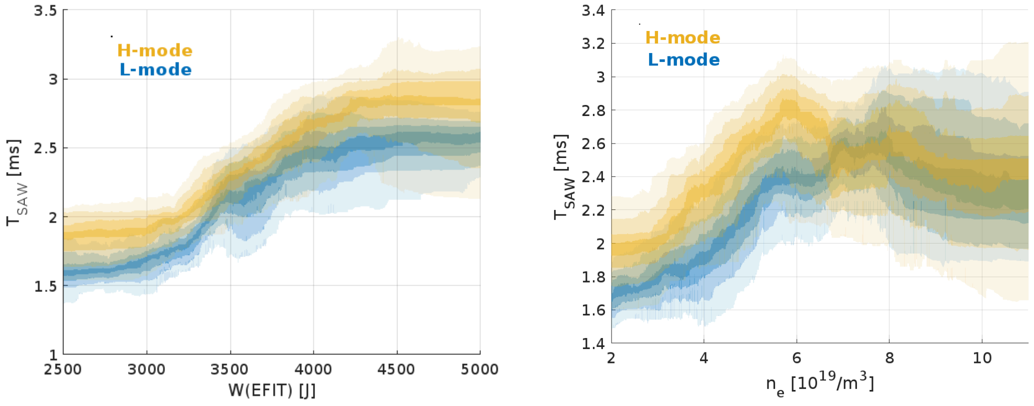

(a) (b)

Figure 6.18: Dependence of the awtooth period on the plasma energy W for plasma densities lower than $7 \cdot 10^{19}/m^3$ (a) and dependence of the sawtooth period on the plasma density without NBI in L-mode and H-mode (b).

Plasma shape

The plasma shape can affect the kink mode stability [145] and the sawtooth period [167]. At COMPASS, experiments with D-shaped plasmas have typically similar plasma shape parameters (minor radius ranging from 0.16 to 0.175 and elongation at 1.8). One of the campaigns investigating wider ranges of plasma parameters was the one with experiments using an additional coil to enable a wider range of triangularities as it is described in section 4.2). The sawtooth period did not change during the triangularity scan as it is shown in Fig. 6.19 suggesting no effect on stability of the internal kink mode. However, the change of upper triangularity was approximately five times smaller than in the case of TCV where the sawtooth period changed from 1.5 ms to 3 ms for triangulaties ranging from -0.2 to 0.4.

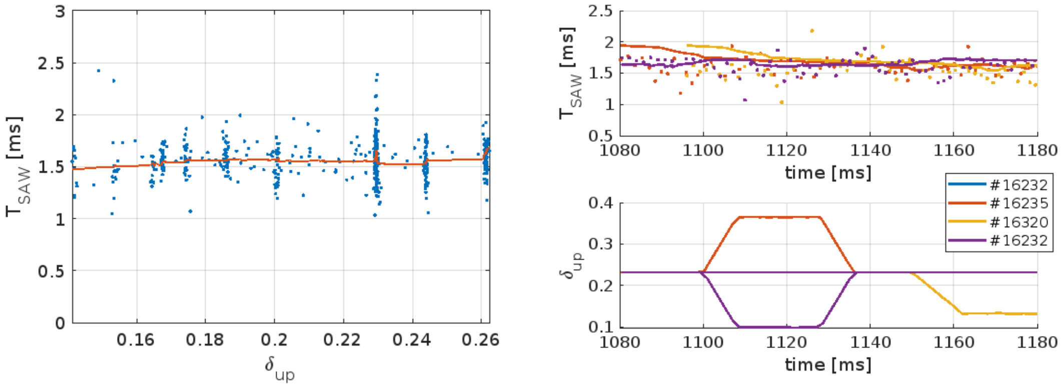

(a) (b)

Figure 6.19: Scan of the sawtooth period over the upper triangularity (a) and an example of evolution of triangularity (reconstructed by the Fiesta code) and sawtooth period in time (b).

Ion mass

The sawtooth period can change with the ion mass as it is indicated by the third criteria in 6.5 or by equation 6.6 (due to a change of the normalised Larmor radius $\hat{\rho}$) which is the most relevant criteria for the auxiliary heated plasmas [139]. At COMPASS, no clear evidence for any change of the sawtooth period during NBI heating between the helium and deuterium plasmas was observed as it is shown in Fig. 6.20. However, presence of other impurities could overcome effect of helium on the sawtooth period. No change of the sawtooth period was also observed in other helium pulses without NBI.

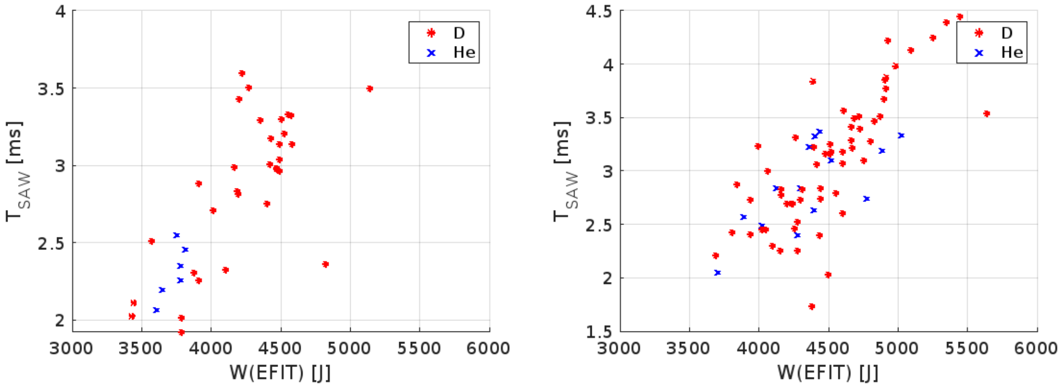

(a) (b)

Figure 6.20: Sawtooth period with respect to the plasma energy in the discharges in deuterium and helium for L-mode (a) and H-mode (b) with the applied NBI heating of 280 kW.

6.4.2 Inversion radius of sawtooth instability

The inversion radius (i.e. radius where $q = 1$) is supposed to be close to a location where the electron temperature and the electromagnetic emission, in particular the bremsstrahlung radiation, does not change during the sawtooth crash. This location can be found by means of the tomographic reconstruction of the SXR profile. A useful tool for visualisation of the process of the sawtooth crash seen by the SXR diagnostic is the singular value decomposition (SVD). The SVD can be applied to decompose matrix **M** into a weighted and ordered sum of separable matrices $\mathbf{A}_i$:

$$\mathbf{M} = \sum \mathbf{A}_i = \sum \sigma_i \mathbf{U}_i \otimes \mathbf{V}_i \tag{6.19}$$

where σ_i are the ordered singular values, $\mathbf{U}_i$ and $\mathbf{V}_i$ the i-th columns of the corresponding SVD matrices.

Applying the SVD to a matrix representing time series of the tomographic reconstructions, i.e. matrix where each column contains a tomographic reconstruction at a specific time allows the decomposition of the evolution of the reconstructed SXR profile into modes as it is shown in Fig. 6.21. The top plots represent the shapes of the first four dominant components of the SXR profile (the "topos") given by $\mathbf{V}_i$. These components contribute to the reconstructed SXR profile evolution by weights given by $\sigma_i \mathbf{U}_i$ shown in the bottom plots ("chronos u1"). The second mode illustrates a redistribution of the SXR emission during the sawtooth crash. The SVD can be applied to visualise processes during the sawteeth and to separate poloidally symmetrical components of the SXR emission for better localisation of the inversion radius which can be found as a location with the lowest variation of the SXR profile, see Fig. 6.22. The resulting inversion radii are shown in Fig. 6.23 with respect to the plasma density before and after the NBI heating. The inversion radius is typically about 45% (which is often observed in tokamaks [139]) of the minor radius, i.e. about 7 cm and at about $\psi_n = 0.3$ (which is consistent with inversion radius seen by the Thomson scattering in Fig. 6.8). The inversion radius is sometimes observed to change with the applied NBI and the plasma pressure [168]. However, at COMPASS there is no clear dependence of the inversion radius on the plasma density and on the applied NBI heating suggesting that a possible change of the location of the $q = 1$ surface at the moment of sawtooth crash is in this particular case below the resolution of this method.

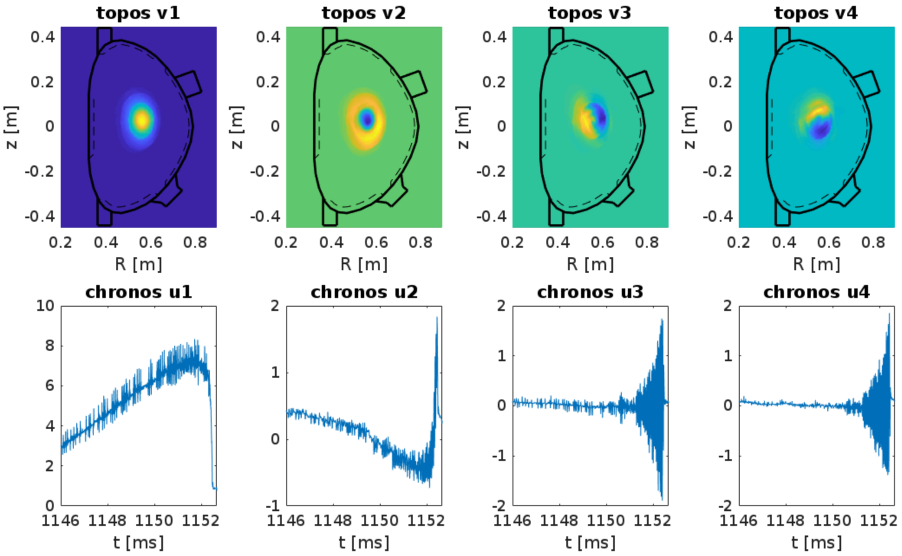

Figure 6.21: Example of SVD applied on the reconstructed SXR profiles duringthe sawtooth crash neighbourhood in the discharge #5751. The top row shows the shapes of the dominant components whereas the bottom row shows temporal evolution of their weights. The first column corresponds to the basic mode showing an increase in the core radiation followed by a fast drop during the sawtooth crash. The second column illustrates redistribution of the radiation near the inversion radius. The third and fourth columns correspond to oscillations caused by the internal mode.

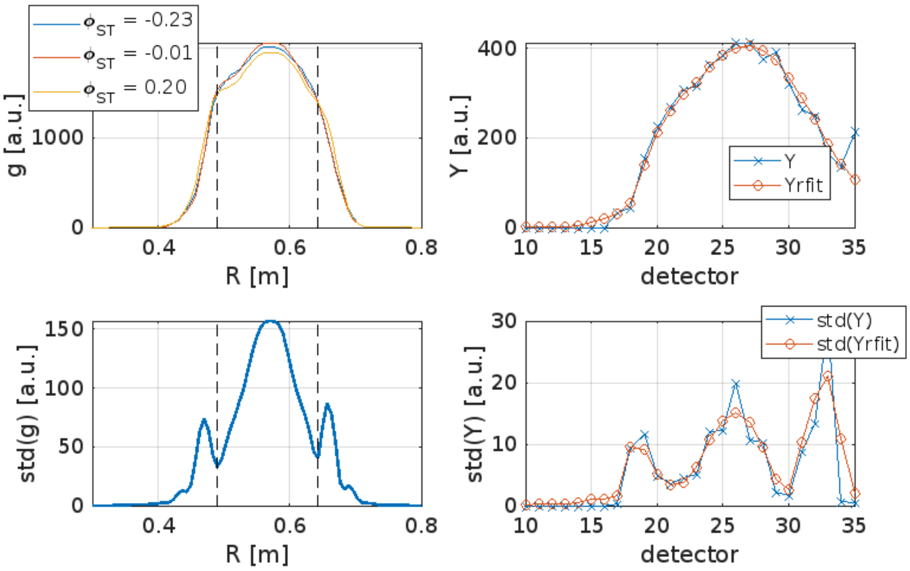

Figure 6.22: Reconstructed SXR profiles (top-left), Variance of the profiles (bottom-left), signals and retrofit (top-right) and its variation (bottom-right).

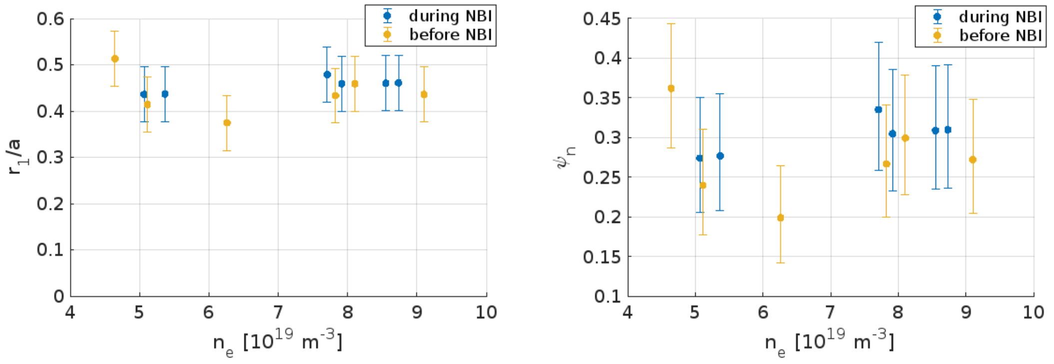

(a) (b)

Figure 6.23: Inversion radius normalised to the minor radius (a) and as a value of the normalised poloidal flux ψ_n (b) before and after the applied NBI heating power 400-480 kW with respect to the electron density. Values of ψ_n are consistent with the inversion radius seen by the Thomson scattering in Fig. 6.8. The errorbars represent a spatial resolution of the detectors ±1 cm.

6.5 Effect of sawtooth instability on edge plasma processes

The sawtooth instability changes the temperature profile and magnetic topology in a significant volume of the plasma, and therefore affects various plasma processes. Although major changes happen in the plasma core, the sawteeth can also affect processes occurring in the plasma edge due to a heat wave propagating from the plasma core to the edge during the sawtooth crash. This coupling between the plasma core and edge is remarkable mainly for smaller tokamaks. In the following sections, the effect of sawtooth on edge plasma processes like L-H transition, H-L transition, transition to ELM-free H-mode and ELMs is described.

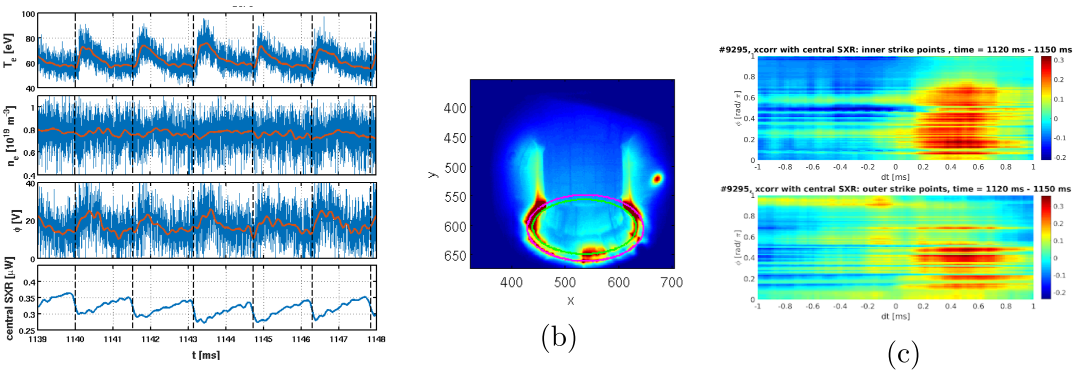

(a)

(b)

(c)

Figure 6.24: Illustration of the effect of the sawtooth crash at the plasma edge at COMPASS: (a) Electron temperature (T_e), density (n_e) and plasma potential (Φ) measured by the horizontal reciprocating probe near the separatrix during the discharge #6878 [66]. T_e starts to rise almost immediately with the sawtooth crash. Maximum of T_e is delayed by 0.2 ms, whereas Φ is delayed by 0.4 ms. b) Visible radiation measured by the Photron camera. (c) Cross correlations of the central SXR with the visible radiation coming from the inner strike point (indicated by the green circle in picture (b)) and the outer strike point (indicated by the purple circle in picture (b)) shows a delay about 0.5 ms.

6.5.1 L-H transition

At the COMPASS tokamak the transition to H-mode, i.e. L-H transition, is usually easily recognisable by a drop of the D_α signal and its fluctuations corresponding to a decreased intensity of the plasma-wall interaction as shown in Fig. 6.25.

The sawtooth crash can trigger a transition to H-mode as it is sometimes observed e.g. on ASDEX [140, 18], JFT-2M [141] TCV, [142], EAST [143]. It is supposed that the hot plasma expelled from the central region to the edge after the sawtooth crash can supply enough free energy for the formation of the edge shear flows and the transport barrier. At the COMPASS tokamak, synchronization of the L-H transition with the sawtooth crash is very clear as it can be seen in Fig. 6.26. The edge plasma is supplied by sufficiently frequent heat pulses from sawtooth crashes with such an intensity so that the L-H transition is triggered by sawteeth as soon as the plasma is near the conditions for the L-H transition. As it can be seen in the Fig. 6.26, a significant drop in the D_α signal representing the L-H transition mostly appears within 10% and 30% of the sawtooth period and about 0.4 ms after the sawtooth crash. No clear dependence of the L-H transition delay on B_T, X-point height, n_e, plasma thermal energy and P_{SEP} was found.

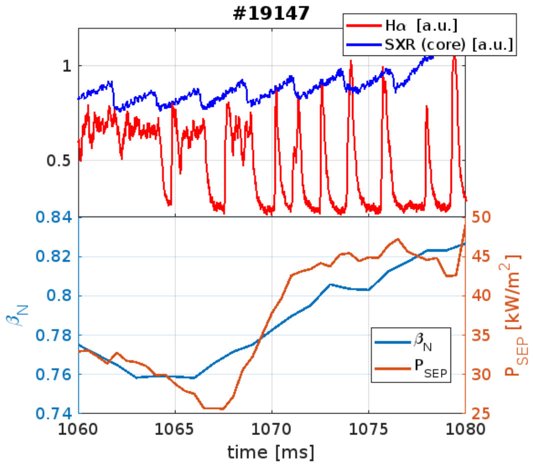

Figure 6.25: Example of L-H transitions represented by a drop of D_α synchronised with sawtooth crashes. The peaks after 1070 ms correspond to ELMs. The lower plot shows a corresponding rise of P_{SEP} and β_N.

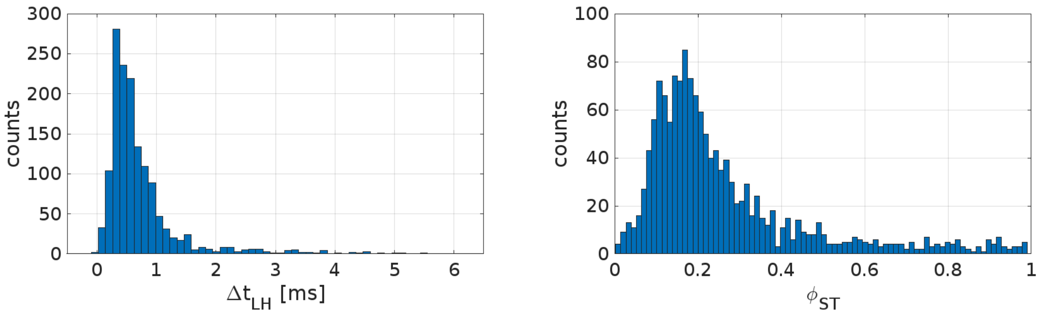

(a)

(b)

Figure 6.26: (a) Occurrence of the delay of the L-H transition in ms and (b) with respect to the sawtooth phase at COMPASS. Observations of the synchronisations of L-H transition with the sawtooth crash at COMPASS was published in the enclosed article A.3 and in [66]. This figure significantly improves statistics to 325 discharges and 1482 detected L-H transitions.

6.5.2 H-L transition

At the COMPASS tokamak, it is also observed that the sawteeth can also affect the H-L transition from H-mode back to the regime with a lower energy confinement as it can be seen in Fig 6.26 (in contrast to the enclosed article A.3 where the effect of the sawtooth crash was probably hidden in the insufficient available statistics). It is observed that the H-L transition is mostly avoided within the first 30% of the sawtooth phase and 0.4 ms after the sawtooth crash. These delays correspond to the previous section dealing with the sawtooth crash triggering the L-H transition. The heat pulse from the sawtooth crash apparently delays an occurrence of the conditions for the H-L transition so that it takes place mostly within the middle of the sawtooth phase. The occurrence of the H-L transition then decreases towards the end of the sawtooth phase and remains low also in the early phase (within the first 10% before the arrival of the heat pulse to the plasma edge) which could be a consequence of previously occurred H-L transitions in the middle of the sawtooth phase when the conditions for the H-L transition already appeared.

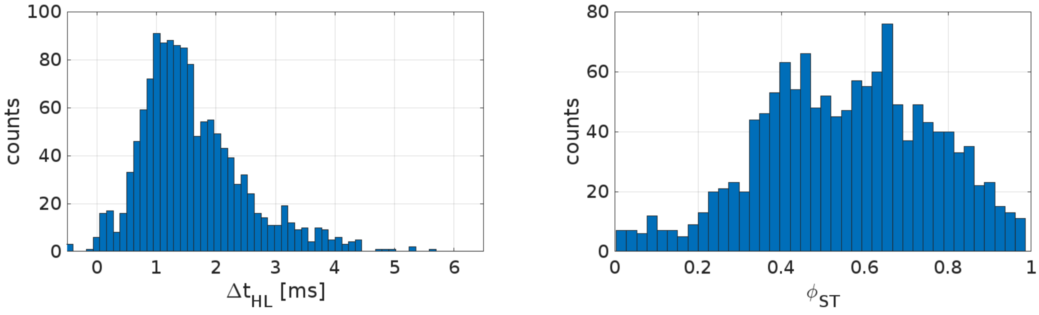

(a) (b)

Figure 6.27: The delay of the H-L transition after the sawtooth crash in time (a) and with respect to the phase of sawtooth cycle (b). The histograms show that the H-L transition is less likely to happen within the first 30% of the sawtooth phase and 0.4 ms after the sawtooth crash. The histograms contain 246 discharges and 1374 H-L transitions improving .

There are transitions between regimes with changed intensity of plasma-wall interactions (indicated by D_α signal) with rather short duration, i.e. shorter than sawtooth period and than the energy confinement time. These short transitions typically occurs when plasma is close to the thresholds for the H-mode. Fast fluctuations of D_α signals between intensities coresponding to L-mode or H-mode are often called dithering oscillations [170, 171]. In this section, regimes with short (< 3 ms) but clearly decreased plasma-wall interaction regime are called short "H-modes". These regimes do not represent fully developed H-mode, but they indicate clear decrease of plasma-wall interaction and development of the edge transport barrier. The H-L transitions from short and full H-modes are compared in Fig. 6.28b with respect to the sawtooth phase. Shorter "H-modes" with the duration comparable to the sawtooth period (less than 3 ms) have a more peaked probability of the occurrence than longer H-modes with maximum at about 1. ms after the sawtooth crash or at about 0.6 of the sawtooth phase. These short "H-modes" are strongly modulated by sawteeth, triggered shortly after the sawtooth crash and ending usually at cca 0.4 sawtooth phase or cca 1.3 ms after the sawtooth crash when the effect of the heat pulse from the sawtooth crash vanishes and the conditions at the plasma edge (mainly edge T_e decreasing during the sawtooth phase) are not sustainable for H-mode. The occurrence of the H-L transition from full H-modes (more than 3 ms) shows the maximum with shifted (or slightly higher) timer delays.

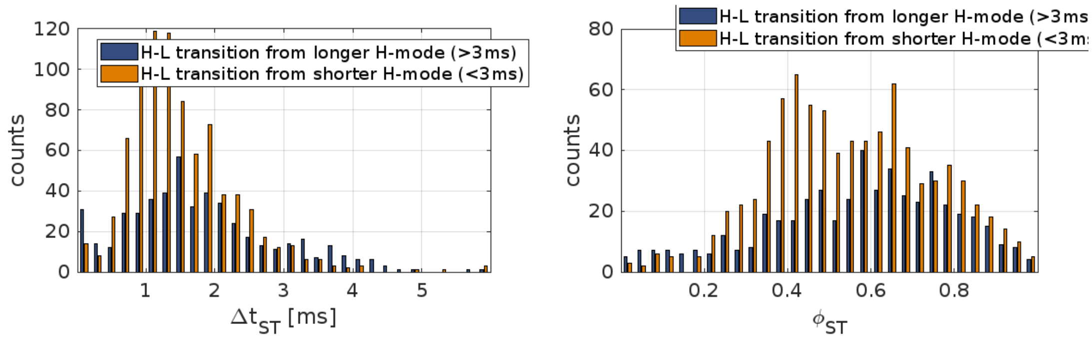

(a) (b)

Figure 6.28: Occurrences of the H-L transitions after the sawtooth crash (a) and with respect to the sawtooth phase (b) for shorter (less than 3 ms) "H-modes" and for longer (more than 3 ms) H-modes.

6.5.3 Transition from ELMy to ELM-free H-mode

The sawtooth crashes seem to be correlated with the transition from ELMy H-mode to ELM-free H-mode as it is indicated in Fig. 6.29 and 6.30 showing an example of ELM-free H-mode starting after the sawtooth crash and histogram of the occurrence of last ELM before the ELM-free phase. A similar behaviour was described for TCV in [142]. The effect is not so statistically dominant as in the case of the L-H transition, but still clearly visible. Moreover, there is a group of last ELMs before ELM-free H-mode occurring in the middle of the sawtooth phase. This similarity with the H-L transition (shown in the previous section) indicates a decrease of plasma edge stability towards the middle of the sawtooth phase. This behaviour could be a consequence of a decrease of the edge pressure gradient (as shown in Fig. 6.8) while the edge current density does not change fast enough (rather slow diffusion of plasma current into the plasma core compared to the sawtooth cycle is indicated in the section 6.4.1) so that the plasma crosses the peeling boundary stability condition for type-III ELMs as illustrated in Fig. 2.4b.

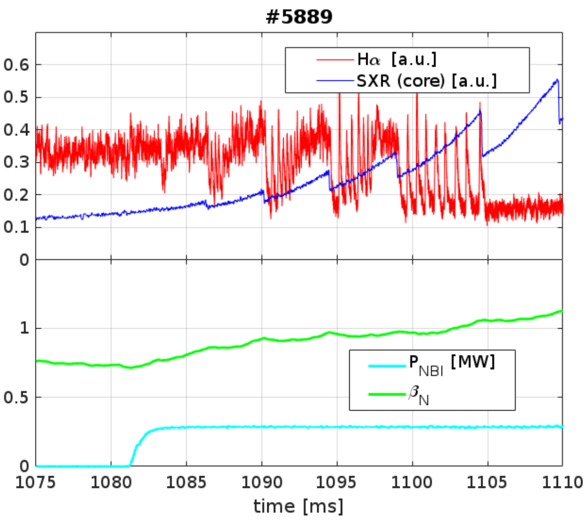

Figure 6.29: Transitions to H-mode and ELM-free H-mode coinciding with sawtooth crashes (top) and applied NBI power with β_N (bottom) from EFIT during discharge #5889.

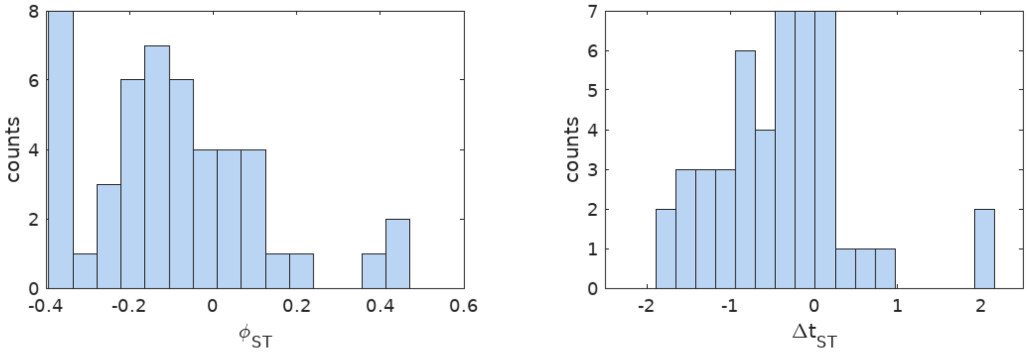

(a)

(b)

Figure 6.30: (a) Occurrence of last ELMs before ELM-free H-mode phases with respect to the sawtooth phase and (b) with respect to the time delay after the sawtooth crash.

6.5.4 Edge localised mode

The sawtooth instability can affect the edge plasma parameters so that it can influence ELMs as it was indicated in [16] for type III ELMs at JET or at TCV [144]. Occasionally, it can be directly observed that ELMs are modulated by the sawtooth instability at COMPASS, see Fig. 6.31b. However, these cases are rare as it is shown in Fig. 6.31a and the sawtooth period is typically longer than the ELM "period", in particular during the NBI heating.

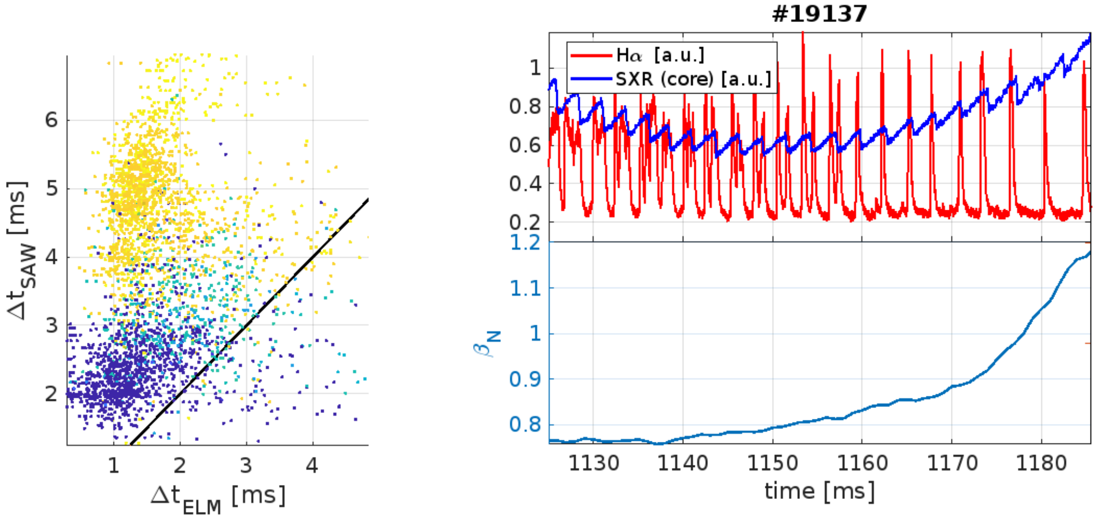

(a)

(b)

Figure 6.31: (a) sawtooth period with respect to the ELM ”period” where colors represent a different NBI applied power (from dark blue representing zero to 800 kW represented by yellow) and (b) transitions to ”H-mode” (represented by the drops in the red D_α signal) triggered by the sawteeth (represented by the core SXR in blue) smoothly changes to ELMs synchronised with the sawteeth. The lower plot shows an evolution of β_N.

The effect of the sawtooth instability on ELMs is clearly visible at COMPASS under larger statistics as it is shown in Fig. 6.32a where the ELMs distribution has the lowest values at about 0.4 ms after the sawtooth crash (corresponding to cca 0.2 of the sawtooth phase) and the values increase towards the middle of the sawtooth cycle and remain roughly constant in the second half of the sawtooh period. The delay after the sawtooth crash with the minimum in the ELM distribution corresponds to the delay of the L-H transition occurring due to arrival of the heat pulse to the plasma edge from the plasma core. This heat pulse can increase the edge pressure gradient so that it shifts the edge plasma into the stable region for type-III ELMs as shown in Fig. 2.4b.

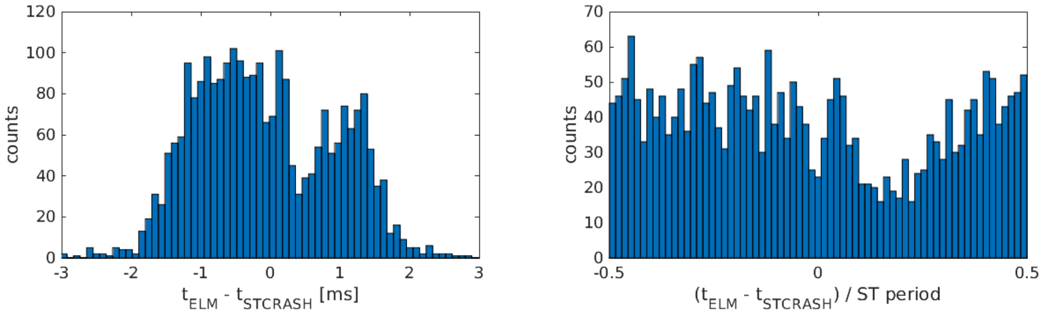

(a)

(b)

Figure 6.32: Histogram of the delays between edge localised mode and the sawtooth crash (statistics covers 286 discharges improving results shown in the attached article A.3).

The sawtooth period and ELM ”period” (related to histograms in Fig. 6.32) with respect to the selected parameters are shown in Fig. 6.33. The sawtooth period follows tendencies shown in the previous sections, in particular a well pronounced increase with the plasma kinetic energy. The dependence of the ELM "period" indicates increasing trends with β_p, τ_E, the sawtooth period and the plasma energy for different $\mathrm{P_{NBI}}$ distinguished by different colours.

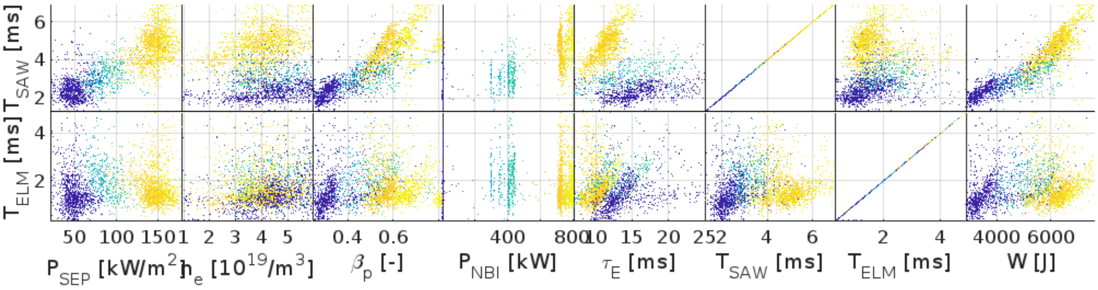

Figure 6.33: Sawtooth period and ELM period with respect to the selected plasma parameters.

6.6 Summary

At COMPASS, the sawtooth instability is observed to affect numerous plasma processes. The chapter started with characterisation of the sawtooth instability at COMPASS, in particular with the dependence of its period on various plasma parameters. It is shown that the sawtooth period increases with the plasma density, pressure (or β_p) and energy confinement time while it decreases with the electron temperature and plasma resistivity. These dependencies indicate that the diffusion of the plasma current into the plasma core is not a dominant process governing the sawtooth period at COMPASS (as it contradicts formula 6.7) and it is rather associated with more processes at once, e.g. with the competition of the pressure gradient with the steepness of the current profile (as indicated by the second bracket in 6.2) and others. A similar behaviour is sometimes observed in other tokamaks, in particular during "small" sawteeth [145, 139]. Increase of sawtooth period with plasma density is also consistent with the Porcelli criteria during resistive regime for the sawtooth crash trigger ($s_1 > s_{crit}$) since the cricial shear s_{crit} mainly increases with plasma density. However, the sawtooth instability itself can also affect the plasma kinetic energy since a less frequent redistribution of the pressure profile could lead to lower energy losses and a better energy confinement time.

At COMPASS, the NBI heating on the sawtooth instability has a stabilising effect in the co-current regime (i.e. leading to longer sawtooth period) and destabilising in counter-current regime where it is observed to decrease sawtooth period. Similar behaviour was observed e.g. at JET [158]. In the case of the counter-current NBI heating power above 400 kW, other MHD modes are often present and disturb the sawtooth instability and can lead to disruptions. Sawtooth period is observed to be closely related to the plasma kinetic energy during NBI which could indicate importance of the pressure gradient for the stability of the internal kink mode at COMPASS. The effect of the NBI heating and plasma density on the inversion radius is not observed implying that a possible change of $q = 1$ at the moment of the sawtooth crash is below the resolution of SXR tomgoraphy at COMPASS.

Section 6.5 describes the effect of the sawtooth instability on the selected plasma phenomena at COMPASS: occurrence of ELMs, L-H transition, H-L transition and transition from ELMy H-mode to ELM-free H-mode. The statistics covers about 300 experiments which were processed semi-automatically (with manual corrections in case of errors). It is shown that the L-H transition is strongly correlated with the sawtooth crash at COMPASS and occurs about 0.4 ms after the sawtooth crash which is comparable to the observed delay between the sawtooth crash and the heat pulse reaching the plasma edge. The sawtooth crash also affects the H-L transition which is less likely to happen within the first 30% of the sawtooth phase and 0.4 ms after the sawtooth crash. The heat pulse from the sawtooth crash apparently delays an occurrence of the conditions for the H-L transition so that it takes place mostly within the middle of the sawtooth phase. The occurrence of the H-L transition then decreases towards the end of the sawtooth phase and remains low also in the early phase (within the first 10% before the arrival of the heat pulse to the plasma edge) which could be a consequence of the previously occurred H-L transitions. The sawtooth crashes are also correlated with the transition from ELM-free H-mode to ELMy H-mode. Moreover, there is grouping of last ELMs before ELM-free H-mode occurring in the middle of the sawtooth phase. This similarity with the H-L transition indicates a lower plasma edge stability in the middle of the sawtooth phase. The sawtooth instability affects an occurrence of ELMs since the ELMs distribution has its minimum value at about 0.4 ms after the sawtooth crash (corresponding to cca 20% of the sawtooth phase).

Conclusion

The results section of the thesis begins with simulations of the MHD equilibria since the magnetic field configuration plays an important role in plasma stability and the used tomographic reconstructions. At COMPASS, the simulations successfully predicted the achieved plasma triangularities. In the case of COMPASS-U, the simulations were also applied to optimise the design of the PF coils, including positioning the PF coils outside TF coils (in a co-authored work also presented in [78]) and verified a possibility to reduce the number of the expensive power sources via an appropriate pairing of the CS coils. The simulated plasma scenarios cover various configurations, including a D-shaped plasma, double null configuration, plasma with negative triangularity, snowflake configuration and scenario with sweeping the strike points. The D-shaped plasmas with the planned plasma current 2 MA are typically achievable within the current limits of the PF coils and vertically stabilisable (according to the condition for the vertical stability parameter $f_s > 1.5$). However, they are susceptible to MHD instabilities due to $q_{95} > 3$. Thus, lower plasma currents (e.g. 1.5 MA or 1.2 MA) are more stable according to the simulations. Various unconventional plasma shapes are achievable, but for lower plasma currents, e.g. snowflake configuration for plasma currents up to 1.5 MA and negative triangularity up to 1 MA.

The thesis continues with a tomographic reconstruction based on Minimum Fisher Regularisation, its optimisation and shows examples of its application to the AXUV and SXR measurements during instabilities at COMPASS and JET. Distribution of the radiation losses measured by the AXUV was reconstructed during ELMs at COMPASS, indicating its proportionality to the kinetic plasma energy losses (calculated by EFIT). The reconstructions of the distribution of the radiation losses during the experiments aimed at the detachment regime via the impurity seeding helped to determine an optimal puff of nitrogen to reduce the heat flux reaching the divertor while avoiding a strong accumulation of plasma impurities in the plasma core, which can subsequently cause a disruption. The SXR tomography was also applied at JET. The tomography of the band-pass filtered data was indicated as a possible candidate to locate $m > 1$ MHD modes even though the reconstruction of the mode structure fails. A potential of the SXR tomography for real-time plasma control purposes and as a tool providing information about the plasma position in the case of pure tokamak plasmas was also studied. The centre of mass of the SXR radiation calculated by the fast linear methods was compared with the plasma position represented by its magnetic axis from EFIT showing the same trends with systematic differences (with a variance of about 1.5 cm) which were affected by the plasma shape and the systematic errors of the diagnostics. The 2D tomography according to one camera with a high preferential smoothing along the magnetic field was applied to avoid issues with the different spectral sensitivity of the cameras and to observe the propagation of impurities into the plasma core during a mitigated disruption, i.e. helping to identify the amount of the impurity seeding to optimally mitigate a disruption.

The main physical outcome of the thesis is a characterisation of the effect of the sawteeth on edge plasma processes and of the sawtooth instability itself at the COMPASS tokamak and its comparison with current physic models and with observations from other tokamaks.

The sawtooth period is shown to increase with the plasma density, kinetic energy, NBI heating, energy confinement time and to decrease with the core electron temperature (e.g. in contrast to [168] scaling sawtooth period at JET) and plasma resistivity. The decreasing trend with the central electron temperature could be a consequence of a negligible effect of the diffusion of the plasma current in the plasma core (as it contradicts formula 6.14) in comparison with other effects, e.g. competition of the pressure gradient with the steepness of the current profile. The METIS simulations indicate a resistive regime of the internal kink mode, i.e. possible fulfilment of the third condition in the Porcelli model for the sawtooth crash. The resistive regime is often observed in current tokamaks e.g. at JET [146] or TEXTOR [166] which is a device of similar to COMPASS in size and in the length of sawtooth period). Moreover, increasing the sawtooth period with the plasma density is consistent with the $s_1 > s_{crit}$ criterion for the sawtooth crash trigger in the resistive regime since s_{crit} strongly increases with the plasma density (resp. density decay length). The sawtooth period is also observed to strongly increase with the applied co-current NBI heating. This could be a consequence of stabilisation of the kink mode by the toroidal plasma rotation (gyroscopic stabilisation) since an increase of the apparent kink mode frequency (of which significant component is supposed to be given by the toroidal rotation) is also observed. Overall, the sawtooth period is observed to be closely related to the plasma kinetic energy (from EFIT) and energy confinement time (as expected from theory [145]). The increasing trend of the sawtooth period with the plasma kinetic energy and energy confinement time could also be a consequence of the lower losses of plasma energy under less frequent sawtooth crashes (flattening of the plasma pressure profile). The sawtooth inversion radius was not observed to depend on the plasma density and NBI heating, implying that a possible change of the location of the $q = 1$ surface at the moment of the sawtooth crash is below the resolution of the applied method, resp. the SXR tomography.

The sawtooth crash is shown to trigger a vast majority of the detected L-H transitions. It is indicated that whenever the plasma parameters are close to the threshold for the L-H transition (e.g. high heating power, X-point height, etc.), the heat pulse from the plasma core induced by the sawtooth crash triggers a formation of the edge transport barrier. The sawtooth crashes are also observed to coincide with a transition from ELMy to ELM-free H-mode. This effect is less statically dominant than in the case of the L-H transition but still clearly visible. It is also observed that ELMs are less likely to happen after the sawtooth crash. This could be a consequence of improved edge stability (with respect to the peeling mode shown in Fig. 2.4b) as a heat pulse from the sawtooth crash can significantly increase the edge pressure gradient compared to the edge current density. Similar effects are observed at other tokamak devices (e.g. at TCV [144] or JET [16]), but they are very clear at COMPASS due to its smaller dimensions and interconnectedness of the plasma core and edge. In addition, the effect of the sawtooth instability on the H-L transition is observed. It is shown that the H-L transition is most probable in the middle of the sawtooth cycle. Decreasing the plasma edge stability towards the middle of the sawtooth cycle is also indicated in the statistics of last ELM in H-mode showing a group of detected ELMs in the middle of the sawtooth cycle.

Bibliography

[1] John. Wesson and D. J. Campbell. *Tokamaks.* Oxford University Press, New York, 3rd ed edition, 2004.

[2] H. Zohm. *Mahnetohydrodynamic stability of tokamaks.* Wiley-VCH Verlag GmbH & Co. KGaA, 2015.

[3] Jeffrey P. Freidberg. *Ideal MHD.* Cambridge University Press, 2014.

[4] J. P. Goedbloed, Rony Keppens, and Stefaan Poedts. *Advanced magnetohydrodynamics: with applications to laboratory and astrophysical plasmas.* Cambridge University Press, 2010.

[5] Kulhánek Petr. *Úvod do teorie plazmatu.* AGA, 2011.

[6] V D Shafranov. On magnetohydronamical equilibrium configurations. *Soviet Phys. JETP*, Vol: 6, mar 1958.

[7] de M.F.M. Bock. *Understanding and controlling plasma rotation in tokamaks.* PhD thesis, Technische Universiteit Eindhoven, 2007.

[8] Wojciech Fundamenski. *Power exhaust in fusion plasmas.* Cambridge University Pres, 2014.

[9] V. D. Shafranov. Hydromagnetic Stability of a Current-Carrying Pinch in a Strong Longitudinal Magnetic Field. *Soviet Physics Technical Physics*, 15:175, Aug 1970.

[10] P Zanca, L Marrelli, R Paccagnella, A Soppelsa, M Baruzzo, T Bolzonella, G Marchiori, P Martin, and P Piovesan. Feedback control model of them= 2,n= 1 resistive wall mode in a circular plasma. *Plasma Physics and Controlled Fusion*, 54(9):094004, 2012.

[11] Marshall N. Rosenbluth. Nonlinear properties of the internal m=1 kink instability in the cylindrical tokamak. *Physics of Fluids*, 16(11):1894, 1973.

[12] M. N. Bussac, R. Pellat, D. Edery, and J. L. Soule. Internal kink modes in toroidal plasmas with circular cross sections. *Physical Review Letters*, 35(24):1638–1641, 1975.

[13] Claude Mercier. Un critere necessaire de stabilite hydromagnetique pour un plasma en symetrie de revolution. *Nucl. Fusion*, 1(1):47–53, 1960.

[14] Claude Mercier and H Luc. *The magnetohydrodynamic approach to the problem of plasma confinement in closed magnetic configurations.* Commission of the European Communities, Directorate General Scientific and . . . , 1974.

[15] F. Wagner, G. Becker, K. Behringer, D. Campbell, A. Eberhagen, W. Engelhardt, G. Fussmann, O. Gehre, J. Gernhardt, G. V. Gierke, and

et al. Regime of improved confinement and high beta in neutral-beam-heated divertor discharges of the asdex tokamak. *Physical Review Letters*, 49(19):1408–1412, Aug 1982.

[16] H Zohm. Edge localized modes (ELMs). *Plasma Physics and Controlled Fusion*, 38(2):105–128, feb 1996.

[17] Yunfeng Liang. Edge localized mode (elm). In *Active Control of Magneto-hydrodynamic Instabilities in Hot Plasmas*, pages 143–181. Springer, 2015.

[18] F. Wagner. A quarter-century of h-mode studies. *Plasma Physics and Controlled Fusion*, 49(12B), 2007.

[19] RJ Bickerton, JW Connor, and JB Taylor. Diffusion driven plasma currents and bootstrap tokamak. *Nature Physical Science*, 229(4):110–112, 1971.

[20] MC Zarnstorff, MG Bell, M Bitter, Robert James Goldston, B Grek, RJ Hawryluk, K Hill, D Johnson, D McCune, H Park, et al. Bootstrap current in tftr. *Physical review letters*, 60(13):1306, 1988.

[21] JG Cordey, CD Challis, and PM Stubberfield. Bootstrap current theory and experimental evidence. *Plasma Physics and Controlled Fusion*, 30(11):1625, 1988.

[22] EJ Doyle, RJ Groebner, KH Burrell, P Gohil, T Lehecka, NC Luhmann Jr, H Matsumoto, TH Osborne, WA Peebles, and R Philipona. Modifications in turbulence and edge electric fields at the l–h transition in the diii-d tokamak. *Physics of Fluids B: Plasma Physics*, 3(8):2300–2307, 1991.

[23] AW Degeling, YR Martin, JB Lister, L Villard, VN Dokouka, VE Lukash, and RR Khayrutdinov. Magnetic triggering of elms in tcv. *Plasma physics and controlled fusion*, 45(9):1637, 2003.

[24] PT Lang, AW Degeling, JB Lister, YR Martin, PJ Mc Carthy, ACC Sips, W Suttrop, GD Conway, L Fattorini, O Gruber, et al. Frequency control of type-i elms by magnetic triggering in asdex upgrade. *Plasma physics and controlled fusion*, 46(11):L31, 2004.

[25] SP Gerhardt, Joon-Wook Ahn, JM Canik, R Maingi, R Bell, D Gates, R Goldston, R Hawryluk, BP Le Blanc, J Menard, et al. First observation of elm pacing with vertical jogs in a spherical torus. *Nuclear fusion*, 50(6):064015, 2010.

[26] PT Lang, J Neuhauser, LD Horton, T Eich, L Fattorini, JC Fuchs, O Gehre, A Herrmann, P Ignácz, M Jakobi, et al. Elm frequency control by continuous small pellet injection in asdex upgrade. *Nuclear Fusion*, 43(10):1110, 2003.

[27] PT Lang, B Alper, R Buttery, K Gal, J Hobirk, J Neuhauser, M Stamp, JET-EFDA contributors, et al. Elm triggering by local pellet perturbations in type-i elmy h-mode plasma at jet. *Nuclear Fusion*, 47(8):754, 2007.

[28] Larry R Baylor, Stephen Kirk Combs, Charles R Foust, Thomas C Jernigan, SJ Meitner, PB Parks, John B Caughman, DT Fehling, S Maruyama, AL Qualls, et al. Pellet fuelling, elm pacing and disruption mitigation technology development for iter. *Nuclear fusion*, 49(8):085013, 2009.

[29] Todd E Evans, Richard A Moyer, Keith H Burrell, Max E Fenstermacher, Ilon Joseph, Anthony W Leonard, Thomas H Osborne, Gary D Porter, Michael J Schaffer, Philip B Snyder, et al. Edge stability and transport control with resonant magnetic perturbations in collisionless tokamak plasmas. *nature physics*, 2(6):419–423, 2006.

[30] Y Liang, HR Koslowski, PR Thomas, E Nardon, B Alper, P Andrew, Y Andrew, G Arnoux, Y Baranov, M Bécoulet, et al. Active control of type-i edge-localized modes with n= 1 perturbation fields in the jet tokamak. *Physical review letters*, 98(26):265004, 2007.

[31] A Kirk, E Nardon, R Akers, M Bécoulet, G De Temmerman, B Dudson, B Hnat, YQ Liu, R Martin, P Tamain, et al. Resonant magnetic perturbation experiments on mast using external and internal coils for elm control. *Nuclear Fusion*, 50(3):034008, 2010.

[32] Francis Troyon, R Gruber, H Saurenmann, S Semenzato, and S Succi. Mhd-limits to plasma confinement. *Plasma physics and controlled fusion*, 26(1A):209, 1984.

[33] Valentin Igochine. *Active Control of Magneto-hydrodynamic Instabilities in Hot Plasmas*. Springer, 2015.

[34] Martin Greenwald, JL Terry, SM Wolfe, S Ejima, MG Bell, SM Kaye, and GH Neilson. A new look at density limits in tokamaks. *Nuclear Fusion*, 28(12):2199, 1988.

[35] Martin Greenwald. Density limits in toroidal plasmas. *Plasma Physics and Controlled Fusion*, 44(8), 2002.

[36] W Suttrop, M Kaufmann, HJ De Blank, B Brüsehaber, K Lackner, V Mertens, H Murmann, J Neuhauser, F Ryter, H Salzmann, et al. Identification of plasma-edge-related operational regime boundaries and the effect of edge instability on confinement in asdex upgrade. *Plasma Physics and Controlled Fusion*, 39(12):2051, 1997.

[37] D. A. Gates and L. Delgado-Aparicio. Origin of tokamak density limit scalings. *Physical Review Letters*, 108(16), 2012.

[38] PT Lang, W Suttrop, E Belonohy, M Bernert, RM Mc Dermott, R Fischer, J Hobirk, OJWF Kardaun, G Kocsis, B Kurzan, et al. High-density h-mode operation by pellet injection and elm mitigation with the new active in-vessel saddle coils in asdex upgrade. *Nuclear Fusion*, 52(2):023017, 2012.

[39] L.c Ingesson, B Alper, H Chen, A.w Edwards, G.c Fehmers, J.c Fuchs, R Giannella, R.d Gill, L Lauro-Taroni, M Romanelli, and et al. Soft x ray tomography during elms and impurity injection in jet. *Nuclear Fusion*, 38(11):1675–1694, 1998.

[40] Weston M. Stacey. *Fusion plasma physics.* Wiley-VCH, 2012.

[41] I. H. Hutchinson. *Principles of plasma diagnostics.* Third Edition. Cambridge University Press, 2005.

[42] H. R. Griem. *Plasma spectroscopy.* McGraw-Hill, 1964.

[43] L.C. Ingesson, B Alper, B.J. Peterson, and Jean-Claude Vallet. Chapter 7: Tomography diagnostics: Bolometry and soft-x-ray detection. *Fusion Science and Technology*, 53:528–576, 02 2008.

[44] George B. Rybicki and Alan P. Lightman. *Radiative Processes in Astrophysics.* WILEY-VCH Verlag GmbH & Co. KGaA, 2004.

[45] Navikov I. D. and Thorne K. S. *Astrophysics of Black Holes.* Gordon and Breach, Science Publishers, Inc, New York, 1973.

[46] R.v. Jensen, D.e. Post, W.h. Grasberger, C.b. Tarter, and W.a. Lokke. Calculations of impurity radiation and its effects on tokamak experiments. *Nuclear Fusion*, Jan 1977.

[47] David Salzmann. *Atomic physics in hot plasmas.* Oxford University Press, 1998.

[48] A. A. Mavrin. Radiative cooling rates for low-z impurities in non-coronal equilibrium state. *Journal of Fusion Energy*, 36(4-5):161–172, 2017.

[49] Matěj Tomeš, Vladimír Weinzettl, Tiago Pereira, Martin Imríšek, and Jakub Seidl. Calculation of edge ion temperature and poloidal rotation velocity from carbon iii triplet measurements on the compass tokamak. *Nukleonika*, 61(4):443–451, Jan 2016.

[50] M Willensdorfer, G Birkenmeier, R Fischer, F M Laggner, E Wolfrum, G Veres, F Aumayr, D Carralero, L Guimarãis, B Kurzan, and et al. Characterization of the li-bes at asdex upgrade. *Plasma Physics and Controlled Fusion*, 56(2):025008, Oct 2014.

[51] M. Brix, D. Dodt, A. Korotkov, P. Morgan, D. Dunai, R. Fischer, A. Meigs, I. S. Nedzelskiy, J. Schweinzer, J. Vince, and et al. Upgrade of the lithium beam diagnostic at jet. *Review of Scientific Instruments*, 81(10), 2010.

[52] H. Stoschus, D. M. Thomas, B. Hudson, M. Watkins, D. F. Finkenthal, R. A. Moyer, and T. H. Osborne. Status and characterization of the lithium beam diagnostic on diii-d. *Review of Scientific Instruments*, 84(8):083503, 2013.

[53] H. A. Kramers. On the theory of x-ray absorption and of the continuous x-ray spectrum. *The London, Edinburgh, and Dublin Philosophical Magazine and Journal of Science*, 46(275):836–871, 1923.

[54] Jeffrey P. Freidberg. *Plasma physics and fusion energy.* Cambridge University Press, 2010.

[55] D Kh Morozov. Greenwald density limit and power balance in tokamaks. *Journal of Physics: Conference Series*, 941:012009, 2017.

[56] T Pütterich, E Fable, R Dux, M O'Mullane, R Neu, and M Siccinio. Determination of the tolerable impurity concentrations in a fusion reactor using a consistent set of cooling factors. *Nuclear Fusion*, 59(5):056013, 2019.

[57] Mlynar J. *Focus on: JET*. Culham Science Centre, 2007.

[58] G. Cunningham. High performance plasma vertical position control system for upgraded mast. *Fusion Engineering and Design*, 88(12):3238–3247, 2013.

[59] GTA Huysmans, JP Goedbloed, and W Kerner. Proceedings of the cp90 conference on computational physics, 1991.

[60] H. Lütjens, A. Bondeson, and A. Roy. Axisymmetric mhd equilibrium solver with bicubic hermite elements. *Computer Physics Communications*, 69(2-3):287–298, 1992.

[61] Wilson H R et al. Scene bootstrap current model upgrade to the full hirshman-sigmar formulation for thermal species, with modifications to allow for anisotropic pressure: Scene4.0, 1996.

[62] L.l. Lao, H. St. John, R.d. Stambaugh, A.g. Kellman, and W. Pfeiffer. Reconstruction of current profile parameters and plasma shapes in tokamaks. *Nuclear Fusion*, 25(11):1611–1622, 1985.

[63] *A new free-boundary equilibrium evolution code, FREEBIE*, volume 39. European Physical Society, 2012.

[64] G O Ludwig. Direct variational solutions of the tokamak equilibrium problem. *Plasma Physics and Controlled Fusion*, 39(12):2021–2037, 1997.

[65] Martin Hron, Jiri Adamek, Jordan Cavalier, Renaud Dejarnac, Ondřej Ficker, Ondrej Grover, Jan Horacek, Michael Komm, Eva Macusova, Ekaterina Matveeva, et al. Overview of the compass results. *Nuclear Fusion*, 2021.

[66] R Panek, J Adámek, M Aftanas, P Bílková, P Böhm, F Brochard, P Cahyna, J Cavalier, R Dejarnac, M Dimitrova, et al. Status of the compass tokamak and characterization of the first h-mode. *Plasma Physics and Controlled Fusion*, 58(1):014015, 2015.

[67] J. Havlicek. *Study of Equilibrium Magnetic Configuration in Tokamak Type Devices*. PhD thesis, Charles University, 2015.

[68] Radomir Panek, T Markovic, P Cahyna, R Dejarnac, J Havlicek, J Horacek, M Hron, M Imrisek, P Junek, M Komm, et al. Conceptual design of the compass upgrade tokamak. *Fusion Engineering and Design*, 123:11–16, 2017.

[69] P Vondracek, Radomír Pánek, Martin Hron, J Havlicek, Vladimír Weinzettl, T Todd, D Tskhakaya, Geoffrey Cunningham, P Hacek, Jakub Hromádka, et al. Preliminary design of the compass upgrade tokamak. *Fusion Engineering and Design*, 169:112490, 2021.

[70] J.f. Artaud, F. Imbeaux, J. Garcia, G. Giruzzi, T. Aniel, V. Basiuk, A. Bécoulet, C. Bourdelle, Y. Buravand, J. Decker, and et al. Metis: a fast integrated tokamak modelling tool for scenario design. *Nuclear Fusion*, 58(10):105001, 2018.

[71] Tikhonov A. N. On the stability of inverse problems. *Doklady Akademii Nauk SSSR*, 39:195–198, 1943.

[72] Tikhonov A. N. Solution of incorrectly formulated problems and the regularization method. *Doklady Akademii Nauk SSSR*, 151:501–504, 1963.

[73] Tikhonov A. N. and Arsenin V. Y. Solutions of ill posed problems. *VH Winston*, 1977.

[74] David L. Phillips. A technique for the numerical solution of certain integral equations of the first kind. *Journal of the ACM (JACM)*, 9(1):84–97, 1962.

[75] J. A. Leuer. Passive vertical stability in the next generation tokamaks. *Fusion Technology*, 15(2P2A):489–494, 1989.

[76] Alfredo Portone. The stability margin of elongated plasmas. *Nuclear fusion*, 45(8):926, 2005.

[77] F Hofmann, S Coda, P Lavanchy, X Llobet, Ph Marmillod, Y Martin, A Martynov, J Mlynar, J-M Moret, A Pochelon, et al. Extension of the tcv operating space towards higher elongation and higher normalized current. *Nuclear fusion*, 42(6):743, 2002.

[78] L Kripner, M Peterka, M Imrıšek, T Markovic, J Urban, J Havlıcek, M Hron, F Jaulmes, R Pánek, and D Šesták. Equilibrium design for the compass-u tokamak. *WDS'18 Proceedings of Contributed Papers—Physics*, pages 99–104, 2018.

[79] S Saarelma, Lorenzo Frassinetti, P Bilkova, CD Challis, A Chankin, Richard Fridström, L Garzotti, L Horvath, CF Maggi, and JET Contributors. Self-consistent pedestal prediction for jet-ilw in preparation of the dt campaign. *Physics of Plasmas*, 26(7):072501, 2019.

[80] Benoît Labit, Hugo De Olivera, Roberto Maurizio, Antoine Merle, Umar Sheikh, Pedro Andres Molina Cabrera, Thomas Eich, Elisabeth Wolfrum, Matthias Bernert, Jeorg Stober, et al. Plasma shape and fueling dependence on the small elms regime in tcv and aug. In *27th IAEA Fusion Energy Conference*, 2018.

[81] B Labit, T Eich, GF Harrer, E Wolfrum, M Bernert, MG Dunne, L Frassinetti, Pascale Hennequin, R Maurizio, A Merle, et al. Dependence on plasma shape and plasma fueling for small edge-localized mode regimes in tcv and asdex upgrade. *Nuclear Fusion*, 59(8):086020, 2019.

[82] TW Petrie, ME Fenstermacher, SL Allen, TN Carlstrom, P Gohil, RJ Groebner, CM Greenfield, AW Hyatt, CJ Lasnier, RJ La Haye, et al. A comparison of plasma performance between single-null and double-null configurations during elming h-mode. Technical report, General Atomics, San Diego, CA (US), 1999.

[83] D Brunner, AQ Kuang, B LaBombard, and JL Terry. The dependence of divertor power sharing on magnetic flux balance in near double-null configurations on alcator c-mod. *Nuclear Fusion*, 58(7):076010, 2018.

[84] DD Ryutov. Geometrical properties of a “snowflake” divertor. *Physics of Plasmas*, 14(6):064502, 2007.

[85] DD Ryutov, RH Cohen, TD Rognlien, and MV Umansky. The magnetic field structure of a snowflake divertor. *Physics of Plasmas*, 15(9):092501, 2008.

[86] F Piras, S Coda, I Furno, JM Moret, RA Pitts, O Sauter, B Tal, G Turri, A Bencze, BP Duval, et al. Snowflake divertor plasmas on tcv. *Plasma Physics and Controlled Fusion*, 51(5):055009, 2009.

[87] VA Soukhanovskii, Ronald E Bell, Ahmed Diallo, Stefan Gerhardt, S Kaye, E Kolemen, Benoit P LeBlanc, AG McLean, JE Menard, Stephen F Paul, et al. Snowflake divertor configuration studies in national spherical torus experiment. *Physics of Plasmas*, 19(8):082504, 2012.

[88] VA Soukhanovskii. Snowflake divertor studies in diii-d and nstx aimed at the power exhaust solution for the tokamak. Technical report, Lawrence Livermore National Lab.(LLNL), Livermore, CA (United States), 2013.

[89] Zhouji Huang and Stefano Coda and. Dependence of density fluctuations on shape and collisionality in positive- and negative-triangularity tokamak plasmas. *Plasma Physics and Controlled Fusion*, 61(1):014021, nov 2018.

[90] M. E. Austin, A. Marinoni, M. L. Walker, M. W. Brookman, J. S. deGrassie, A. W. Hyatt, G. R. McKee, C. C. Petty, T. L. Rhodes, S. P. Smith, C. Sung, K. E. Thome, and A. D. Turnbull. Achievement of reactor-relevant performance in negative triangularity shape in the diii-d tokamak. *Phys. Rev. Lett.*, 122:115001, Mar 2019.

[91] A Marinoni, ME Austin, AW Hyatt, ML Walker, J Candy, C Chrystal, CJ Lasnier, GR McKee, T Odstrčil, CC Petty, et al. H-mode grade confinement in l-mode edge plasmas at negative triangularity on diii-d. *Physics of Plasmas*, 26(4):042515, 2019.

[92] A Marinoni, O Sauter, and S Coda. A brief history of negative triangularity tokamak plasmas. *Reviews of Modern Plasma Physics*, 5(1):1–44, 2021.

[93] Renaud Dejarnac and et al. Plasma-Facing Components in COMPASS Upgrade. Technical report, Institute of plasma physics of the CAS, 2021.

[94] Thomas Eich, AW Leonard, RA Pitts, W Fundamenski, Robert James Goldston, TK Gray, A Herrmann, A Kirk, A Kallenbach, O Kardaun, et al. Scaling of the tokamak near the scrape-off layer h-mode power width and implications for iter. *Nuclear fusion*, 53(9):093031, 2013.

[95] D Brunner, B LaBombard, AQ Kuang, and JL Terry. High-resolution heat flux width measurements at reactor-level magnetic fields and observation of a unified width scaling across confinement regimes in the alcator c-mod tokamak. *Nuclear Fusion*, 58(9):094002, 2018.

[96] F Maviglia, G Federici, G Strohmayer, R Wenninger, Ch Bachmann, R Albanese, R Ambrosino, M Li, VP Loschiavo, JH You, et al. Limitations of transient power loads on demo and analysis of mitigation techniques. *Fusion Engineering and Design*, 109:1067–1071, 2016.

[97] Jan Horacek, Geoffrey Cunningham, Slavomir Entler, Petr Dobias, Richard Duban, Martin Imrisek, Tomas Markovic, Josef Havlicek, and Rustam Enikeev. Feasibility study of fast swept divertor strike point suppressing transient heat fluxes in big tokamaks. *Fusion Engineering and Design*, 123:646–649, 2017.

[98] Johann Radon. On the determination of functions from their integral values along certain manifolds. *IEEE Transactions on Medical Imaging*, 5(4):170–176, 1986.

[99] F. Natterer. *The Mathematics of computerized tomography.* Society for Industrial and Applied Mathematics, 2001.

[100] L C Ingesson and V V Pickalov. An iterative projection-space reconstruction algorithm for tomography systems with irregular coverage. *Journal of Physics D: Applied Physics*, 29(12):3009–3016, 1996.

[101] M Anton, H Weisen, M J Dutch, W Von Der Linden, F Buhlmann, R Chavan, B Marletaz, P Marmillod, and P Paris. X-ray tomography on the tcv tokamak. *Plasma Physics and Controlled Fusion*, 38(11):1849–1878, Jan 1996.

[102] M. Odstrcil, J. Mlynar, T. Odstrcil, B. Alper, and A. Murari. Modern numerical methods for plasma tomography optimisation. *Nuclear Instruments and Methods in Physics Research Section A: Accelerators, Spectrometers, Detectors and Associated Equipment*, 686:156–161, 2012.

[103] D. Mazon, D. Vezinet, D. Pacella, D. Moreau, L. Gabelieri, A. Romano, P. Malard, J. Mlynar, R. Masset, P. Lotte, and et al. Soft x-ray tomography for real-time applications: present status at tore supra and possible future developments. *Review of Scientific Instruments*, 83(6):063505, 2012.

[104] J Mlynar, M Imrisek, V Weinzettl, M Odstrcil, J Havlicek, F Janky, B Alper, A Murari, and JET-EFDA Contributors. Introducing minimum fisher regularisation tomography to axuv and soft x-ray diagnostic systems of the compass tokamak. *Review of Scientific Instruments*, 83(10):10E531, 2012.

[105] J Mlynar, S Coda, A Degeling, B P Duval, F Hofmann, T Goodman, J B Lister, X Llobet, and H Weisen. Investigation of the consistency of magnetic and soft x-ray plasma position measurements on tcv by means of a rapid tomographic inversion algorithm. *Plasma Physics and Controlled Fusion*, 45(2):169–180, 2003.

[106] V. Loffelmann, J. Mlynar, M. Imrisek, D. Mazon, A. Jardin, V. Weinzettl, and M. Hron. Minimum fisher tikhonov regularization adapted to real-time tomography. *Fusion Science and Technology*, 69(2):505–513, 2016.

[107] N Terasaki, Y Hosoda, M Teranishi, and N Iwama. Linear algebraic algorithms for high speed and stable reconstruction of plasma image. *Fusion Engineering and Design*, 34-35:801–804, 1997.

[108] G C Fehmers, L P J Kamp, and F W Sluijter. An algorithm for quadratic optimization with one quadratic constraint and bounds on the variables. *Inverse Problems*, 14(4):893–901, Jan 1998.

[109] Hosoda Y. and Torii T. A direct method for ill – posed linear operator equations — truncated least-square least-norm solutions. *Jpn. J. Appl. Math.*, 4:287–298, 1994.

[110] M. Bernert, T. Eich, A. Burckhart, J. C. Fuchs, L. Giannone, A. Kallenbach, R. M. Mcdermott, and B. Sieglin. Application of axuv diode detectors at asdex upgrade. *Review of Scientific Instruments*, 85(3):033503, 2014.

[111] R. L. Boivin, J. A. Goetz, E. S. Marmar, J. E. Rice, and J. L. Terry. High resolution bolometry on the alcator c-mod tokamak (invited). *Review of Scientific Instruments*, 70(1):260–264, 1999.

[112] D. S. Gray, S. C. Luckhardt, L. Chousal, G. Gunner, A. G. Kellman, and D. G. Whyte. Time resolved radiated power during tokamak disruptions and spectral averaging of axuv photodiode response in diii-d. *Review of Scientific Instruments*, 75(2):376–381, 2004.

[113] I. Furno, H. Weisen, J. Mlynar, R. A. Pitts, X. Llobet, Ph. Marmillod, and G. P. Pochon. Fast bolometric measurements on the tcv tokamak. *Review of Scientific Instruments*, 70(12):4552–4556, 1999.

[114] A. G. U. Perera. *Bolometers*. InTech, 2012.

[115] B. Tal, B. Labit, D. Nagy, R. Chavan, B. Duval, and G. Veres. Plasma radiation dynamics with the upgraded absolute extreme ultraviolet tomographical system in the tokamak à configuration variable. *Review of Scientific Instruments*, 84(12):123508, 2013.

[116] M. Anton, M. J. Dutch, and H. Weisen. Relative calibration of photodiodes in the soft-x-ray spectral range. *Review of Scientific Instruments*, 66(7):3762–3769, 1995.

[117] The center for x-ray optics. `https://www.cxro.lbl.gov/`, accessed: 29th december 2021.

[118] M. Vácha. *Detection system for measurements of high-temperature plasma radiation on the COMPASS tokamak by fast bolometers and soft X-rays.* Diploma thesis, Charles University in Prague, 2009.

[119] V Weinzettl, M Imrisek, J Havlicek, J Mlynar, D Naydenkova, P Hacek, M Hron, F Janky, D Sarychev, M Berta, et al. On use of semiconductor detector arrays on compass tokamak. *International Journal of Physical and Mathematical Sciences*, 6(11):1503 – 1509, 2012.

[120] J. W. Connor, A. Kirk, H. R. Wilson, and Sadruddin Benkadda. Edge localised modes (elms): Experiments and theory. *AIP Conference Proceedings*, 2008.

[121] Jordan Cavalier, Nicolas Lemoine, Frédéric Brochard, Vladimir Weinzettl, Jakub Seidl, Scott Silburn, Patrick Tamain, Renaud Dejarnac, Jiri Adamek, and Radomir Panek. Tomographic reconstruction of tokamak edge turbulence from single visible camera data and automatic turbulence structure tracking. *Nuclear Fusion*, 59(5):056025, 2019.

[122] M Komm, I Khodunov, J Cavalier, P Vondracek, S Henderson, J Seidl, J Horacek, D Naydenkova, J Adamek, P Bilkova, et al. Divertor impurity seeding experiments at the compass tokamak. *Nuclear Fusion*, 59(10):106035, 2019.

[123] M Komm, D Mancini, M Morbey, J Cavalier, J Adamek, M Bernert, P Bilkova, P Bohm, D Brida, O Février, et al. Power exhaust by core radiation at compass tokamak. *Nuclear Fusion*, 61(3):036016, 2021.

[124] John Wesson. The science of jet. *Abingdon, Oxon, OX14 3EA, UK*, 2000.

[125] GF Matthews, M Beurskens, S Brezinsek, M Groth, E Joffrin, A Loving, M Kear, ML Mayoral, R Neu, P Prior, et al. Jet iter-like wall—overview and experimental programme. *Physica Scripta*, 2011(T145):014001, 2011.

[126] D Ćirić, DPD Brown, CD Challis, B Chuilon, SJ Cox, B Crowley, IE Day, DC Edwards, G Evison, LJ Hackett, et al. Overview of the jet neutral beam enhancement project. *Fusion Engineering and Design*, 82(5-14):610–618, 2007.

[127] Edwards A. W. Gill R. D., Alper B. First results in d-t from the radiation hardened soft x-ray cameras, 1997.

[128] *2D Tomography of SXR Data from Toroidally Separated Cameras for Studies of Impurity Injection and Fast Instabilities on JET*, volume 38. European Physical Society, 2011.

[129] R. Fitzpatrick. Helical temperature perturbations associated with tearing modes in tokamak plasmas. *Physics of Plasmas*, Jan 1994.

[130] Jan Mlynar, Matej Tomes, Martin Imrisek, Barry Alper, Martin O'Mullane, Tomas Odstrcil, Thomas Puetterich, et al. Soft x-ray tomographic reconstruction of jet ilw plasmas with tungsten impurity and different spectral response of detectors. *Fusion Engineering and Design*, 96:869–872, 2015.

[131] J Mlynar, D Mazon, M Imrisek, V Loffelmann, P Malard, T Odstrcil, M Tomes, D Vezinet, and V Weinzettl. Soft x-ray tomography in support of impurity control in tokamaks. *Journal of Physics: Conference Series*, 768(1):012001, 2016.

[132] S. Von Goeler, W. Stodiek, and N. Sauthoff. Studies of internal disruptions and m=1 oscillations in tokamak discharges with soft-x-ray techniques. *Physical Review Letters*, 33(20):1201–1203, Nov 1974.

[133] A. Klassen, H. Aurass, and G. Mann. Sawtooth oscillations in solar flare radio emission. *Astronomy & Astrophysics*, 370(3):L41–L44, 2001.

[134] D. J. Campbell, D. F. H. Start, J. A. Wesson, D. V. Bartlett, V. P. Bhatnagar, M. Bures, J. G. Cordey, G. A. Cottrell, P. A. Dupperex, A. W. Edwards, and et al. Stabilization of sawteeth with additional heating in the jet tokamak. *Physical Review Letters*, 60(21):2148–2151, 1988.

[135] O. Sauter, E. Westerhof, M. L. Mayoral, B. Alper, P. A. Belo, R. J. Buttery, A. Gondhalekar, T. Hellsten, T. C. Hender, and et al. Howell, D. F. Control of neoclassical tearing modes by sawtooth control. *Physical Review Letters*, 88(10), 2002.

[136] A. Gude, S. Günter, M. Maraschek, H. Zohm, and The Asdex Upgrade Team. Temporal evolution of neoclassical tearing modes and its effect on confinement reduction in asdex upgrade. *Nuclear Fusion*, 42(7):833–840, 2002.

[137] R.J. Buttery, T.C. Hender, D.F. Howell, R.J. La Haye, S. Parris, O. Sauter, C.G. Windsor, and Jet-Efda Contributors. On the form of ntm onset scalings. *Nuclear Fusion*, 44(5):678–685, 2004.

[138] M.F.F Nave, J Rapp, T Bolzonella, R Dux, M.J Mantsinen, R Budny, P Dumortier, M. Von Hellermann, S Jachmich, H.r Koslowski, and et al. Role of sawtooth in avoiding impurity accumulation and maintaining good confinement in jet radiative mantle discharges. *Nuclear Fusion*, 43(10):1204–1213, 2003.

[139] I. T. Chapman. Controlling sawtooth oscillations in tokamak plasmas. *Plasma Physics and Controlled Fusion*, 53(1):013001, 2010.

[140] F. Wagner, G. Fussmann, T. Grave, M. Keilhacker, M. Kornherr, K. Lackner, K. Mccormick, E. R. Müller, A. Stäbler, G. Becker, and et al. Development of an edge transport barrier at the h-mode transition of asdex. *Physical Review Letters*, 53(15):1453–1456, Aug 1984.

[141] T. Ido, K. Kamiya, Y. Miura, Y. Hamada, A. Nishizawa, and Y. Kawasumi. Observation of the fast potential change at l-h transition by a heavy-ion-beam probe on jft-2m. *Physical Review Letters*, 88(5), 2002.

[142] Y R Martin and TCV Team. Synchronization of l-mode to h-mode transitions on the sawtooth cycle in ohmic tcv plasmas. *Plasma Physics and Controlled Fusion*, 46(5A), Jun 2004.

[143] L.m. Shao, G.s. Xu, N. Yan, R. Chen, L. Chen, Y.m. Duan, W. Gao, J.p. Qian, W. Shen, A. Ti, and et al. L-mode to h-mode transition triggered by sawtooth-induced heat flux in east. *Physics Letters A*, page 126184, 2019.

[144] Y R Martin, A W Degeling, and J B Lister. Search for determinism in elm time series in tcv. *Plasma Physics and Controlled Fusion*, 44(5A), 2002.

[145] F Porcelli, D Boucher, and M N Rosenbluth. Model for the sawtooth period and amplitude. *Plasma Physics and Controlled Fusion*, 38(12):2163–2186, Jan 1996.

[146] Glenn Bateman, Canh N. Nguyen, Arnold H. Kritz, and Franco Porcelli. Testing a model for triggering sawtooth oscillations in tokamaks. *Physics of Plasmas*, 13(7):072505, 2006.

[147] C Angioni, A Pochelon, N N Gorelenkov, K G Mcclements, O Sauter, R V Budny, P C De Vries, D F Howell, M Mantsinen, M F F Nave, and et al. Neutral beam stabilization of sawtooth oscillations in jet. *Plasma Physics and Controlled Fusion*, 44(2):205–222, 2002.

[148] C Angioni, T.P Goodman, M.A Henderson, and O Sauter. Effects of localized electron heating and current drive on the sawtooth period. *Nuclear Fusion*, 43(6):455–468, may 2003.

[149] M. Choi, A. D. Turnbull, V. S. Chan, M. S. Chu, L. L. Lao, Y. M. Jeon, G. Li, Q. Ren, and R. I. Pinsker. Sawtooth control using beam ions accelerated by fast waves in the diii-d tokamak. *Physics of Plasmas*, 14(11):112517, 2007.

[150] Martin David Kruskal and Carl R Oberman. On the stability of plasma in static equilibrium. *The Physics of Fluids*, 1(4):275–280, 1958.

[151] Fabien Francis Éric Jaulmes. *Kinetic behaviour of ions in tokamak inductive scenarios.* PhD thesis, Technische Universiteit Eindhoven, 2016.

[152] Kadomtsev B. B. *Disruptive Instability in Tokamaks.* Princeton University Plasma Physics Laboratory, 1976.

[153] C G Gimblett and R J Hastie. Calculation of the post-crash state and 1 1/2 d simulation of sawtooth cycles. *Plasma Physics and Controlled Fusion*, 36(9):1439–1455, Jan 1994.

[154] H. K. Park, N. C. Luhmann, A. J. H. Donné, I. G. J. Classen, C. W. Domier, E. Mazzucato, T. Munsat, M. J. Van De Pol, and Z. Xia. Observation of high-field-side crash and heat transfer during sawtooth oscillation in magnetically confined plasmas. *Physical Review Letters*, 96(19), 2006.

[155] H. K. Park, A. J. H. Donné, N. C. Luhmann, I. G. J. Classen, C. W. Domier, E. Mazzucato, T. Munsat, M. J. Van De Pol, and Z. Xia. Comparison study of 2d images of temperature fluctuations during sawtooth oscillation with theoretical models. *Physical Review Letters*, 96(19), 2006.

[156] M. Swisdak, B. N. Rogers, J. F. Drake, and M. A. Shay. Diamagnetic suppression of component magnetic reconnection at the magnetopause. *Journal of Geophysical Research: Space Physics*, 108(A5), 2003.

[157] M. T. Beidler and P. A. Cassak. Model for incomplete reconnection in sawtooth crashes. *Physical Review Letters*, 107(25), 2011.

[158] M. F. F. Nave, H. R. Koslowski, S. Coda, J. Graves, M. Brix, R. Buttery, C. Challis, C. Giroud, M. Stamp, P. De Vries, and et al. Exploring a small sawtooth regime in joint european torus plasmas with counterinjected neutral beams. *Physics of Plasmas*, 13(1):014503, 2006.

[159] I. T. Chapman, T.c Hender, S Saarelma, S.e Sharapov, R.j Akers, N.j Conway, and The Mast Team. The effect of toroidal plasma rotation on sawteeth in mast. *Nuclear Fusion*, 46(12):1009–1016, 2006.

[160] I. T. Chapman, S.d. Pinches, H.r. Koslowski, Y. Liang, A. Krämer-Flecken, and M. De Bock. Sawtooth stability in neutral beam heated plasmas in textor. *Nuclear Fusion*, 48(3):035004, 2008.

[161] *Global energy confinement time of NBI-heated plasma on the COMPASS tokamak*, volume 41F. European Physical Society, 2017.

[162] Andrew R. Conn, Nicholas I. M. Gould, and Philippe L. Toint. *Trust-region methods*. SIAM, 2000.

[163] O. Grover. *L-H transition and H-mode in tokamak plasma*. Bachelor's thesis, Czech Technical University in Prague, 2015.

[164] F. Jaulmes, B. Geiger, T. Odstrčil, M. Weiland, M. Salewski, A.s. Jacobsen, J. Rasmussen, M. Stejner, S.k. Nielsen, E. Westerhof, and et al. Numerical and experimental study of the redistribution of energetic and impurity ions by sawteeth in asdex upgrade. *Nuclear Fusion*, 56(11):112012, 2016.

[165] Glenn Bateman, Canh N Nguyen, Arnold H Kritz, and Franco Porcelli. Testing a model for triggering sawtooth oscillations in tokamaks. *Physics of plasmas*, 13(7):072505, 2006.

[166] C Angioni, TP Goodman, MA Henderson, and O Sauter. Effects of localized electron heating and current drive on the sawtooth period. *Nuclear Fusion*, 43(6):455, 2003.

[167] H Reimerdes, A Pochelon, O Sauter, TP Goodman, MA Henderson, and An Martynov. Effect of triangular and elongated plasma shape on the sawtooth stability. *Plasma physics and controlled fusion*, 42(6):629, 2000.

[168] *Analysis of shaping effects on sawteeth in JET*. European Physical Society, 2001.

[169] Klára Bogár. *Additional plasma heating of tokamak plasma by powerful beam of deuterium atoms on the COMPASS tokamak*. PhD thesis, Univerzita Karlova, Matematicko-fyzikální fakulta, 2021. PhD thesis.

[170] Hartmut Zohm. Dynamic behavior of the l-h transition. *Physical review letters*, 72(2):222, 1994.

[171] Hartmut Zohm, W Suttrop, K Buchl, HJ De Blank, O Gruber, A Kallenbach, V Mertens, F Ryter, and M Schittenhelm. Investigation of the bifurcation character of the h-mode in asdex upgrade. *Plasma physics and controlled fusion*, 37(4):437, 1995.

List of Figures

List of Tables

List of Abbreviations

ASDEX Axially Symmetric Divertor Experiment

AXUV absolute extreme ultraviolet

CE coronal equilibrium model

CRSS collisional radiative steady state model

CS central solenoid

CXRS charge exchange recombination spectroscopy

DMV disruption mitigation valve

EFIT equilibrium fitting code

ECCD electron cyclotron current drive

ECRH electron cyclotron resonant heating

ECE electron cyclotron emission

ELM edge localized mode

FFT fast Fourier transformation

GEV generalised eigen values

GS Grad-Shafranov

HFS high field side

ICRH ion cyclotron resonant heating

ITER International Thermonuclear Experimental Reactor

JET Joint European Torus

LCFS last closed flux surface

LFS low field side

Li-BES lithium-beam emission spectroscopy

LTE local thermal equilibrium model

LOS line of sight

MARFE multifaceted asymmetric radiation from the edge

MAST Mega Ampere Spherical Tokamak

METIS the minute embedded tokamak integrated simulator

MFR Minimum Fisher Regularisation

MHD magnetohydrodynamic

MSE Motional Stark Effect

NBI Neutral Beam Injection

NTM Neoclassical Tearing Mode

PDE partial differential equation

PDF probability distribution function

PF poloidal field

PFC plasma facing components

RMSE root mean square error

SOL scrape-of layer

SXR soft X-ray

SVD singular value decomposition

TEXTOR Tokamak Experiment for Technology Oriented Research

TF toroidal field

TCV Tokamak à configuration variable

VDE vertical displacement event